CHAPTER 5

SYNTHESIS, MESOMORPHISM AND PHOTOPHYSICAL PROPERTIES OF TETRADENTATE [N_2O_2]-DONOR 'SALPHEN' TYPE SCHIFF BASE LIGANDS AND THEIR VO(IV), Ni(II), Cu(II) AND Zn(II) COMPLEXES

CHAPTER 5

SYNTHESIS, MESOMORPHISM AND PHOTOPHYSICAL PROPERTIES OF TETRADENTATE [N_2O_2]-DONOR 'SALPHEN' TYPE SCHIFF BASE LIGANDS AND THEIR VO(IV), Ni(II), Cu(II) AND Zn(II) COMPLEXES

5.1. Introduction

Ligands with π-conjugated 'salphen' framework have gained enormous attention in recent times attributable primarily to their interesting photophysical, supramolecular properties and reactivity.[1] The extended conjugation offered by the phenyl spacer in the salphen-ligated metal systems hold immense possibilities for the fabrication of catalysts, photo-responsive materials, supramolecular assemblies, non-linear optical materials and novel liquid crystalline entities.[2-9] The electronic properties and steric bulk of the ligand framework can be easily varied in these systems by careful use of substituents to tune the overall potential of the resulting salphen-metal complexes.[1,10-12]

Metallomesogens based on salphen ligands are quite intriguing as systems providing access to interesting liquid crystalline materials.[8,9,13-21] The rigidity of the extensively conjugated ligand offers the anisotropy which is essential for the construction of supramolecular structures favouring mesomorphism. Structural modification by suitable substitution either at the salicylideneimine units or the aryl bridging group often tune the mesomorphic properties of these complexes including loss of mesomorphism, at times.[8,13] Incorporating metal ion in a square planar geometry is another challenging aspect as tetrahedral distortions away from planar geometry, in some cases, disrupt the required anisotropy of the core, frustrating mesomorphism in turn.[14] Luminescent liquid crystals (LCs) are currently in the limelight particularly owing to the intrinsic light-emitting property coupled with unique self-assembly and self-healing features in the mesophase. This has generated great interest in technological applications such as polarized organic lasers,[22] anisotropic light-emitting diodes,[23-25] sensors, information storage, and one-dimensional semiconductors.[26] Extensive π-conjugation in the salphen ligands in combination with

electron-accepting/donating substituents, donor-acceptor (DA) systems, and/or π-extended systems and the ease of preparation makes them potential photo-responsive materials - exhibiting photo- and electroluminescent (PL and EL) properties.[1,27,28] Emission properties of the ligands can be suitably modulated by careful choice of metal ion and (or) substituents across the ligand framework. A series of luminescent 4-substituted-Zn(II) and Ni(II) complexes based on salphen ligands exhibiting different type of columnar phases were reported by our group lately.[16,17,19-21]

In this chapter, we report the synthesis of three new series of mono-substituted and one di-substituted 'salphen type' Schiff base ligands bearing different halogen substituents at the spacer and their corresponding oxovanadium(IV), nickel(II), copper(II) and zinc(II) complexes. Effect of the spacer group substitution on the mesomorphic and photophysical properties of the ligands and the corresponding metal complexes has been studied. Additionally, the role of the metal ion on the mesomorphism and photophysical behaviour of the complexes has been explored.

5.2. Experimental

5.2.1. Synthesis of salphen ligands

The general preparative route for the salphen ligands is presented in **Scheme 5.1**. The ligands were obtained in a two-step synthesis. The first step involves alkylation of 2,4-Dihydroxybenzaldehyde, which is then followed by condensation with the respective mono- and di-substituted halogenated aromatic 1,2-diamines in the second step.

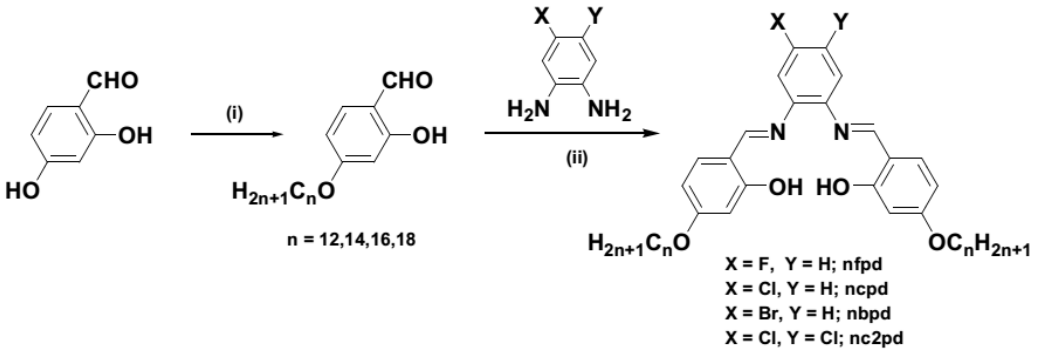

Scheme 5.1: i) $C_nH_{2n+1}Br$, $KHCO_3$, KI, dry acetone, Δ, 24h, and ii) glacial AcOH, absolute EtOH, Δ, 3h.

Synthesis of 4-n-alkoxysalicylaldehyde (n = 12, 14, 16, 18)

2,4-Dihydroxybenzaldehyde (10mmol, 1.38g), $KHCO_3$ (10mmol, 1g), KI (catalytic amount) and 1-bromododecane (10mmol, 2.4g) or 1-bromotetradecane (10mmol, 2.5g) or 1-bromohexadecane (10mmol, 2.8g) 1-bromooctadecane (10mmol, 3g) were mixed in 250 mL of dry acetone; the mixture was heated under reflux for 24 h, and then filtered, while hot, to remove any insoluble solids. Dilute HCl was added to neutralize the warm solution and then extracted with chloroform (100mL). The combined chloroform extract was concentrated to give a purple solid. The solid was purified by column chromatography using a mixture of chloroform and hexane (v/v, 1/1) as an eluent. Evaporation of the solvents afforded a white solid product.

Synthesis of N,N-Bis(4-n-alkoxysalicylidene)-4-fluoro-1,2-diaminobenzene (nfpd); n = 12, 14 or 16

General procedure:

To an ethanolic solution of 1mmol of the corresponding 4-n-alkoxysalicyldehyde, an ethanolic solution of 0.5mmol (0.06g) of 4-Fluoro-1,2-phenylenediamine was added. The solution mixture was heated under reflux with a few drops of acetic acid as a catalyst for 3h to yield the yellow Schiff base. The product was collected by filtration and re-crystallized from absolute ethanol to obtain a pure compound.

N,N-Bis(4-dodecyloxysalicylidene)-4-fluoro-1,2-diaminobenzene (12fpd)

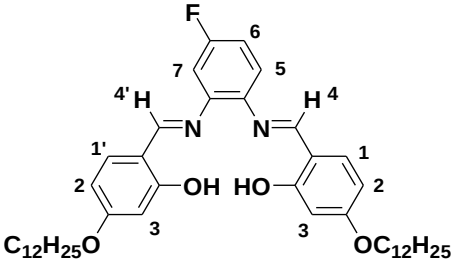

Yield = 0.29g (80%); Anal. Calc. for $C_{44}H_{63}FN_2O_4$ (702.98): C, 75.18; H, 9.03; N, 3.98. Found: C, 75.23; H, 9.01; N, 3.93 %. ^{1}H NMR (400 MHz, $CDCl_3$; Me_4Si at 25°C, ppm): δ = 13.48, 13.36 (s, 2H, OH), 8.52 (s, 1H, $H^{4'}$), 8.49 (s, 1H, H^4), 7.24-7.27 (m, 2H, H^6, H^7), 7.17-7.21(m, 2H, H^1, $H^{1'}$), 6.99 (m, 1H, H^5), 6.55 (d, $^4J_{H,H}$ = 2.44 Hz, 2H, H^3), 6.48-6.52

(m, 2H, H^2), 3.99 (t, $^3J_{H,H}$ = 6.31 Hz, 4H, O-CH_2), 1.70-1.87 (m, 4H, CH_2), 1.29-1.70 (m, 36H, -CH_2), 0.90 (t, $^3J_{H,H}$ = 6.63 Hz, 6H, -CH_3). IR (ν_{max}, cm^{-1}, KBr): 3436 (ν_{OH}), 2918 ($\nu_{as(C\text{-}H),}$ CH_3), 2850 ($\nu_{s(C\text{-}H)}$, CH_3), 1628 ($\nu_{C=N}$), 1293 ($\nu_{C\text{-}O}$).

N,N-Bis(4-tetradecyloxysalicylidene)-4-fluoro-1,2-diaminobenzene (14fpd)

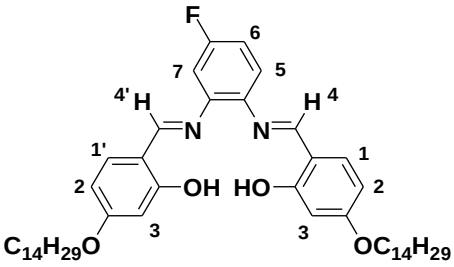

Yield = 0.31g (79%); Anal. Calc. for $C_{48}H_{71}FN_2O_4$ (759.09): C, 75.95; H, 9.43; N, 3.69. Found: C, 75.98; H, 9.41; N, 3.65 %. ^{1}H NMR (400 MHz, $CDCl_3$; Me_4Si at 25°C, ppm): δ = 13.49, 13.37 (s, 2H, OH), 8.51 (s, 1H, $H^{4'}$), 8.48 (s, 1H, H^4), 7.25-7.28 (m, 2H, H^6, H^7), 7.15-7.21 (m, 2H, H^1, $H^{1'}$), 6.99 (m, 1H, H^5), 6.55 (d, $^4J_{H,H}$ = 2.42 Hz, 2H, H^3), 6.46-6.50 (m, 2H, H^2), 3.99 (t, $^3J_{H,H}$ = 6.30 Hz, 4H, O-CH_2), 1.71-1.88 (m, 4H, CH_2), 1.28-1.70 (m, 44H, -CH_2), 0.91 (t, $^3J_{H,H}$ = 6.67 Hz, 6H, -CH_3). IR (ν_{max}, cm^{-1}, KBr): 3437 (ν_{OH}), 2918 ($\nu_{as(C\text{-}H),}$ CH_3), 2849 ($\nu_{s(C\text{-}H)}$, CH_3), 1628 ($\nu_{C=N}$), 1294 ($\nu_{C\text{-}O}$).

N,N-Bis(4-hexadecyloxysalicylidene)-4-fluoro-1,2-diaminobenzene (16fpd)

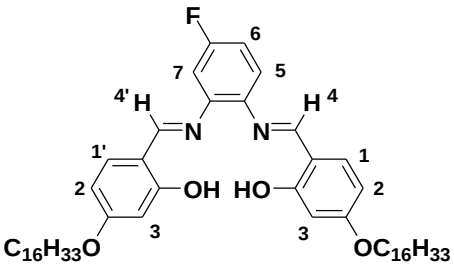

Yield = 0.36g (80%); Anal. Calc. for $C_{52}H_{79}FN_2O_4$ (815.19): C, 76.61; H, 9.77; N, 3.44. Found: C, 76.57; H, 9.73; N, 3.49 %. ^{1}H NMR (400 MHz, $CDCl_3$; Me_4Si at 25°C, ppm): δ = 13.48, 13.35 (s, 2H, OH), 8.52 (s, 1H, $H^{4'}$), 8.49 (s, 1H, H^4), 7.24-7.27 (m, 2H, H^6, H^7), 7.17-7.21 (m, 2H, H^1, $H^{1'}$), 6.98 (m, 1H, H^5), 6.54 (d, $^4J_{H,H}$ = 2.42 Hz, 2H, H^3), 6.47-6.51 (m, 2H, H^2), 3.99 (t, $^3J_{H,H}$ = 6.28 Hz, 4H, O-CH_2), 1.70-1.89 (m, 4H, CH_2), 1.28-1.70 (m,

52H, -CH_2), 0.90 (t, $^3J_{H,H}$ = 6.65 Hz, 6H, -CH_3). IR (ν_{max}, cm^{-1}, KBr): 3436 (ν_{OH}), 2918 ($\nu_{as(C-H),}$ CH_3), 2850 ($\nu_{s(C-H)}$, CH_3), 1629 ($\nu_{C=N}$), 1293 (ν_{C-O}).

Synthesis of N,N-Bis(4-n-alkoxysalicylidene)-4-chloro-1,2-diaminobenzene (ncpd); n = 12, 14, 16 or 18

These ligands were prepared analogously to **nfpd** using 4-Chloro-1,2-diaminobenzene and corresponding 4-n-alkoxysalicyldehyde.

N,N-Bis(4-dodecyloxysalicylidene)-4-chloro-1,2-diaminobenzene (12cpd)

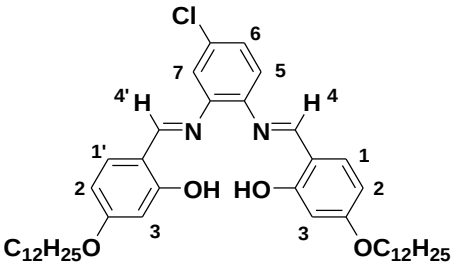

Yield = 0.27g (75%); Anal. Calc. for $C_{44}H_{63}ClN_2O_4$ (719.4): C, 73.46; H, 8.83; N, 3.89. Found: C, 73.45; H, 8.82; N, 3.87. %. ^{1}H NMR (400 MHz, $CDCl_3$; Me_4Si at 25°C, ppm): δ = 13.06 (s, 2H; OH), 8.57 (s, 1H, H^4, $H^{4'}$), 7.72 (d, $^3J_{H,H}$ = 8.54 Hz, H^5), 7.21 (d, 2H, H^7), 7.12 (t, $^3J_{H,H}$ = 8.44 Hz, 2H, H^1, $H^{1'}$), 7.11 (dd, $^4J_{H,H}$ = 2.43Hz, $^3J_{H,H}$ = 9.00 Hz, 2H, H^6), 6.62 (d, $^4J_{H,H}$ = 2.42 Hz, 2H, H^3), 6.48 (dd, $^4J_{H,H}$ = 2.43 Hz, $^3J_{H,H}$ = 8.27 Hz, 2H, H^2), 3.96 (t, $^3J_{H,H}$ = 6.81 Hz, 2H, -OCH_2), 0.86 (m, 40H, CH_2), 0.96 (t, $^3J_{H,H}$ = 6.82 Hz, 6H, -CH_3). IR (ν_{max}, cm^{-1}, KBr): 3400 (ν_{OH}), 2924 ($\nu_{as(C-H),}$ CH_3), 2871 ($\nu_{s(C-H)}$, CH_3), 1628 ($\nu_{C=N}$), 1297 (ν_{C-O}).

N,N-Bis(4-tetradecyloxysalicylidene)-4-chloro-1,2-diaminobenzene (14cpd)

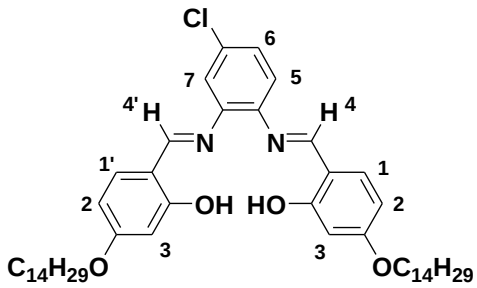

Yield = 0.28g (70%); Anal. Calc. for $C_{48}H_{71}ClN_2O_4$ (774.5): C, 74.34; H, 9.23; N, 3.61. Found: C, 74.35; H, 9.22; N, 3.65. %. ^{1}H NMR (400 MHz, $CDCl_3$; Me_4Si at 25°C, ppm): δ = 13.01 (s, 2H; OH), 8.67 (s, 1H, H^4, $H^{4'}$), 7.76 (d, $^3J_{H,H}$ = 8.53 Hz, H^5), 7.23 (d, 2H, H^7), 7.13 (dd, $^4J_{H,H}$ = 2.41 Hz, $^3J_{H,H}$ = 9.21 Hz, 2H, H^6), 7.13 (t, $^3J_{H,H}$ = 8.44 Hz, 2H, H^1, $H^{1'}$), 6.48 (d, $^4J_{H,H}$ = 2.13 Hz, 2H, H^3), 6.45 (dd, $^4J_{H,H}$ = 2.13 Hz, $^3J_{H,H}$ = 8.29 Hz, 2H, H^2), 3.91(t, $^3J_{H,H}$ = 6.84 Hz, 2H, -OCH_2), 0.86 (m, 48H, -CH_2) 0.95(t, $^3J_{H,H}$ = 6.72 Hz, 6H, -CH_3). IR (ν_{max}, cm^{-1}, KBr): 3435 (ν_{OH}), 2915 ($\nu_{as(C-H)}$, CH_3), 2845 ($\nu_{s(C-H)}$, CH_3), 1626 ($\nu_{C=N}$), 1288 (ν_{C-O}).

N,N-Bis(4-hexadecyloxysalicylidene)-4-chloro-1,2-diaminobenzene (16cpd)

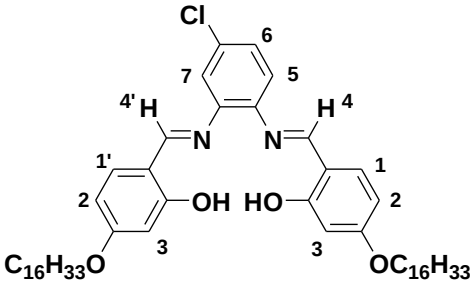

Yield = 0.32g (75%); Anal. Calc. for $C_{52}H_{79}ClN_2O_4$ (831.6): C, 75.10; H, 9.57; N, 3.37. Found: C, 75.12; H, 9.54; N, 3.34 %. ^{1}H NMR (400 MHz, $CDCl_3$; Me_4Si at 25°C, ppm): δ = 13.12 (s, 2H; OH), 8.77 (s, 1H, H^4, $H^{4'}$), 7.74 (d, $^3J_{H,H}$ = 8.54 Hz, H^5), 7.24 (d, 2H, H^7), 7.23 (dd, $^4J_{H,H}$ = 2.81 Hz, $^3J_{H,H}$ = 9.00 Hz, 2H, H^6), 7.15 (t, $^3J_{H,H}$ = 8.43 Hz, 2H, H^1, $H^{1'}$), 6.66 (d, $^4J_{H,H}$ = 2.44 Hz, 2H, H^3), 6.43 (dd, $^4J_{H,H}$ = 2.44 Hz, $^3J_{H,H}$ = 8.29 Hz, 2H, H^2), 3.97(t, $^3J_{H,H}$ = 6.81 Hz, 2H, -OCH_2), 0.99 (m, 56H, -CH_2) 0.88 (t, $^3J_{H,H}$ = 6.32 Hz, 6H, -CH_3). ^{13}C NMR (75.45 MHz; $CDCl_3$; Me_4Si at 25 ^{0}C, ppm) δ= 131.5 (-C_1), 106.8(-C_2), 102.3(-C_3), 161.6(-C_{14}), 160.2(-C_4), 110.5(-C_{13}), 128.8(-C_6), 161.3 (-C_{15}). IR (ν_{max}, cm^{-1}, KBr): 3433 (ν_{OH}), 2918 ($\nu_{as(C-H)}$, CH_3), 2849 ($\nu_{s(C-H)}$, CH_3), 1626 ($\nu_{C=N}$), 1287 (ν_{C-O}).

N,N-Bis(4-octadecyloxysalicylidene)-4-chloro-1,2-diaminobenzene (18cpd)

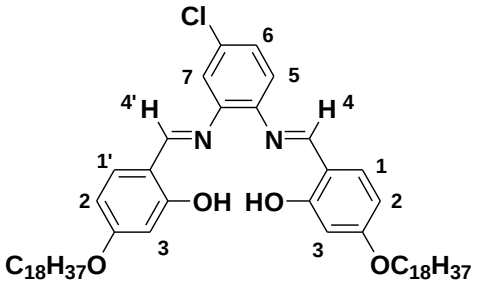

Yield = 0.34g (74%); Anal. Calc. for $C_{56}H_{87}ClN_2O_4$ (887.6): C, 75.76; H, 9.88; N, 3.16. Found: C, 75.74; H, 9.84; N, 3.14 %. ^{1}H NMR (400 MHz, $CDCl_3$; Me_4Si at 25°C, ppm): δ = 13.12 (s, 2H; OH), 8.72 (s, 1H, H^4, $H^{4'}$), 7.77 (d, $^3J_{H,H}$ = 8.54 Hz, H^5), 7.24 (d, 2H, H^7), 7.15 (dd, $^4J_{H,H}$ = 2.41 Hz, $^3J_{H,H}$ = 9.00Hz, 2H, H^6), 7.14 (t, $^3J_{H,H}$ = 8.43 Hz, 2H, H^1, $H^{1'}$), 6.49 (d, $^4J_{H,H}$ = 2.13 Hz, 2H, H^3), 6.45 (dd, $^4J_{H,H}$ = 2.14 Hz, $^3J_{H,H}$ = 8.29 Hz, 2H, H^2), 3.91(t, $^3J_{H,H}$ = 6.81 Hz, 2H, -OCH_2), 0.82 (m, 64H, -CH_2) 0.98 (t, $^3J_{H,H}$ = 6.85 Hz, 6H, -CH_3). IR (ν_{max}, cm^{-1}, KBr): 3434 (ν_{OH}), 2916 ($\nu_{as(C-H)}$, CH_3), 2844 ($\nu_{s(C-H)}$, CH_3), 1622 ($\nu_{C=N}$), 1289 (ν_{C-O}).

Synthesis of N,N-Bis(4-n-alkoxysalicylidene)-4-bromo-1,2-diaminobenzene (nbpd); n = 12, 14 or 16

These ligands were prepared analogously to **nfpd** using 4-Bromo-1,2-diaminobenzene and corresponding 4-n-alkoxysalicyldehyde.

N,N-Bis(4-dodecyloxysalicylidene)-4-bromo-1,2-diaminobenzene (12bpd)

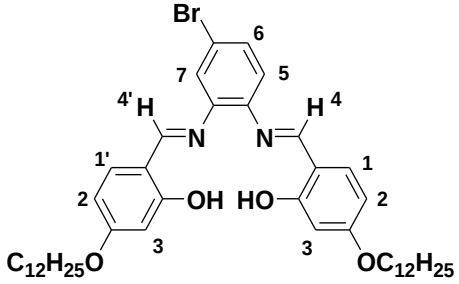

Yield = 0.30g (75%); Anal. Calc. for $C_{44}H_{63}BrN_2O_4$ (763.89): C, 69.18; H, 8.31; N, 3.67. Found: C, 69.22; H, 8.33; N, 3.65 %. ^{1}H NMR (400 MHz, $CDCl_3$; Me_4Si at 25°C, ppm): δ = 13.43, 13.36 (s, 2H; OH), 8.51 (s, 1H, $H^{4'}$), 8.49 (s, 1H, H^4), 7.36-7.42 (m, 2H, H^6, H^7), 7.24-7.27 (m, 2H, H^1, $H^{1'}$), 7.09-7.11 (m, 1H, H^5), 6.56 (d, $^4J_{H,H}$ = 2.23 Hz, 2H, H^3), 6.46-6.53 (m, 2H, H^2), 3.99 (t, $^3J_{H,H}$ = 6.30 Hz, 4H, O-CH_2), 1.75-1.87 (m, 4H, CH_2), 1.28-1.60

(m, 36H, -CH_2), 0.89 (t, $^3J_{H,H}$ = 6.68 Hz, 6H, -CH_3). IR (ν_{max}, cm^{-1}, KBr): 3436 (ν_{OH}), 2919 ($\nu_{as(C-H),}$ CH_3), 2848 ($\nu_{s(C-H)}$, CH_3), 1620 ($\nu_{C=N}$), 1298 (ν_{C-O}).

N,N-Bis(4-tetradecyloxysalicylidene)-4-bromo-1,2-diaminobenzene (14bpd)

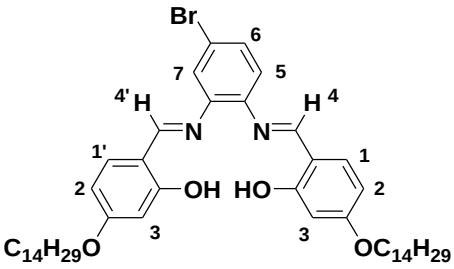

Yield = 0.33g (78%); Anal. Calc. for $C_{48}H_{71}BrN_2O_4$ (819.99): C, 70.31; H, 8.73; N, 3.42. Found: C, 70.27; H, 8.77; N, 3.48 %. ^{1}H NMR (400 MHz, $CDCl_3$; Me_4Si at 25°C, ppm): δ = 13.44, 13.38 (s, 2H; OH), 8.52 (s, 1H, $H^{4'}$), 8.50 (s, 1H, H^4), 7.33-7.45 (m, 2H, H^6, H^7), 7.24-7.27 (m, 2H, H^1, $H^{1'}$), 7.11-7.13 (m, 1H, H^5), 6.55 (d, $^4J_{H,H}$ = 2.28 Hz, 2H, H^3), 6.48-6.52 (m, 2H, H^2), 4.00 (t, $^3J_{H,H}$ = 6.28 Hz, 4H, O-CH_2), 1.75-1.88 (m, 4H, CH_2), 1.29-1.60 (m, 44H, -CH_2), 0.90 (t, $^3J_{H,H}$ = 6.67 Hz, 6H, -CH_3). IR (ν_{max}, cm^{-1}, KBr): 3437 (ν_{OH}), 2918 ($\nu_{as(C-H),}$ CH_3), 2849 ($\nu_{s(C-H)}$, CH_3), 1620 ($\nu_{C=N}$), 1297 (ν_{C-O}).

N,N-Bis(4-hexadecyloxysalicylidene)-4-bromo-1,2-diaminobenzene (16bpd)

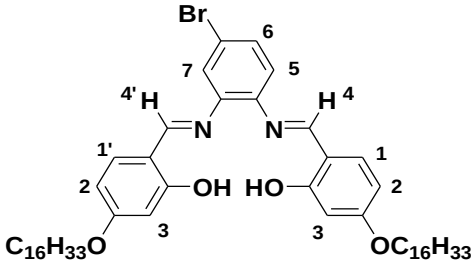

Yield = 0.34g (75%); Anal. Calc. for $C_{52}H_{79}BrN_2O_4$ (876.10): C, 71.29; H, 9.09; N, 3.20. Found: C, 71.33; H, 9.10; N, 3.25 %. ^{1}H NMR (400 MHz, $CDCl_3$; Me_4Si at 25°C, ppm): δ = 13.43, 13.38 (s, 2H; OH), 8.52 (s, 1H, $H^{4'}$), 8.50 (s, 1H, H^4), 7.36-7.42 (m, 2H, H^6, H^7), 7.22-7.27 (m, 2H, H^1, $H^{1'}$), 7.11 (m, 1H, H^5), 6.54 (d, $^4J_{H,H}$ = 2.40 Hz, 2H, H^3), 6.47-6.50 (m, 2H, H^2), 4.00 (t, $^3J_{H,H}$ = 6.29 Hz, 4H, O-CH_2), 1.75-1.86 (m, 4H, CH_2), 1.28-1.59 (m, 52H, -CH_2), 0.90 (t, $^3J_{H,H}$ = 6.67 Hz, 6H, -CH_3). IR (ν_{max}, cm^{-1}, KBr): 3436 (ν_{OH}), 2917 ($\nu_{as(C-H),}$ CH_3), 2848 ($\nu_{s(C-H)}$, CH_3), 1619 ($\nu_{C=N}$), 1298 (ν_{C-O}).

Synthesis of N,N-Bis(4-n-alkoxysalicylidene)-4,5-dichloro-1,2-phenylenediamine (nc2pd); n = 12, 14 or 16

These ligands were prepared analogously to **nfpd** using corresponding 4-n-alkoxysalicyldehyde and 4,5-Dichloro-1,2- phenylenediamine.

N,N-Bis(4-dodecyloxysalicylidene)-4,5-dichloro-1,2-phenylenediamine (12c2pd)

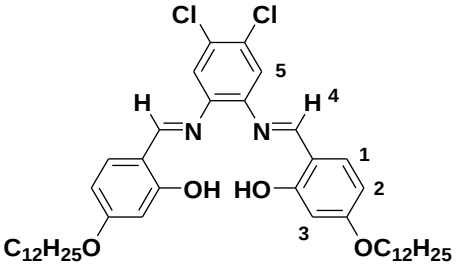

Yield = 0.34g (85%); Anal. Calc. for $C_{44}H_{62}Cl_2N_2O_4$ (753.88): C, 70.10; H, 8.29; N, 3.72. Found: C, 70.14; H, 8.31; N, 3.74 %. ^{1}H NMR (400 MHz, $CDCl_3$; Me_4Si at 25°C, ppm): δ = 13.17 (s, 2H; OH), 8.52 (s, 2H, H^4), 7.32 (s, 2H, H^5), 7.27 (d, $^3J_{H,H}$ = 8.23 Hz, 2H, H^1), 6.54 (d, $^4J_{H,H}$ = 2.01Hz, 2H, H^3), 6.51 (dd, $^3J_{H,H}$ = 8.00Hz, $^4J_{H,H}$ = 2.00Hz, 2H, H^2), 4.00 (t, $^3J_{H,H}$ = 6.52Hz, 4H, O-CH_2), 1.82 (m, 4H, CH_2), 1.25-1.61 (m, 36H, CH_2), 0.90 (t, $^3J_{H,H}$ = 6.74Hz, 6H, CH_3). IR (ν_{max}, cm^{-1}, KBr): 3437 (ν_{OH}), 2916 ($\nu_{as(C\text{-}H),}$ CH_3), 2850 ($\nu_{s(C\text{-}H)}$, CH_3), 1614 ($\nu_{C=N}$), 1298 ($\nu_{C\text{-}O}$).

N,N-Bis(4-tetradecyloxysalicylidene)-4,5-dichloro-1,2-phenylenediamine (14c2pd)

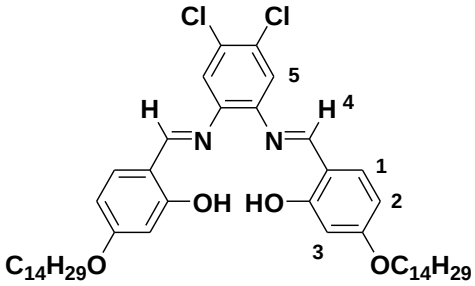

Yield = 0.32g (81%); Anal. Calc. for $C_{48}H_{70}Cl_2N_2O_4$ (809.99): C, 71.18; H, 8.71; N, 3.46. Found: C, 71.21; H, 8.74; N, 3.50 %. ^{1}H NMR (400 MHz, $CDCl_3$; Me_4Si at 25°C, ppm): δ = 13.18 (s, 2H; OH), 8.52 (s, 2H, H^4), 7.31(s, 2H, H^5), 7.25 (d, $^3J_{H,H}$ = 8.0 Hz, 2H, H^1), 6.53 (d, $^4J_{H,H}$ = 2.04Hz, 2H, H^3), 6.50 (dd, $^3J_{H,H}$ = 8.03Hz, $^4J_{H,H}$ = 2.03Hz, 2H, H^2), 4.00 (t, $^3J_{H,H}$ = 6.64Hz, 4H, O-CH_2), 1.80 (m, 4H, CH_2), 1.27-1.57 (m, 44H, CH_2), 0.89 (t, $^3J_{H,H}$ =

6.82Hz, 6H, CH_3). IR (ν_{max}, cm^{-1}, KBr): 3435 (ν_{OH}), 2919 ($\nu_{as(C-H),}$ CH_3), 2849 ($\nu_{s(C-H)}$, CH_3), 1614 ($\nu_{C=N}$), 1297 (ν_{C-O}).

N,N-Bis(4-hexadecyloxysalicylidene)-4,5-dichloro-1,2-phenylenediamine (16c2pd)

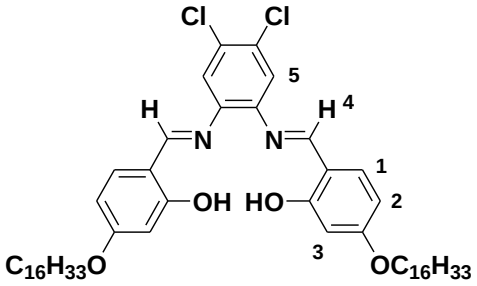

Yield = 0.38g (83%); Anal. Calc. for $C_{52}H_{78}Cl_2N_2O_4$ (866.09): C, 72.11; H, 9.08; N, 3.23. Found: C, 71.12; H, 9.11; N, 3.25 %. ^{1}H NMR (400 MHz, $CDCl_3$; Me_4Si at 25°C, ppm): δ = 13.17 (s, 2H; OH), 8.52 (s, 2H, H^4), 7.32(s, 2H, H^5), 7.27 (d, $^3J_{H,H}$ = 8.0 Hz, 2H, H^1), 6.54 (d, $^4J_{H,H}$ = 2.07Hz, 2H, H^3), 6.50 (dd, $^3J_{H,H}$ = 8.03Hz, $^4J_{H,H}$ = 2.02Hz, 2H, H^2), 4.00 (t, $^3J_{H,H}$ = 6.57Hz, 4H, O-CH_2), 1.81 (m, 4H, CH_2), 1.28-1.58 (m, 52H, CH_2), 0.90 (t, $^3J_{H,H}$ = 6.70Hz, 6H, CH_3). IR (ν_{max}, cm^{-1}, KBr): 3436 (ν_{OH}), 2916 ($\nu_{as(C-H),}$ CH_3), 2850 ($\nu_{s(C-H)}$, CH_3), 1613 ($\nu_{C=N}$), 1299 (ν_{C-O}).

5.2.2. Synthesis of metal complexes (M = VO^{2+}, Ni^{2+}, Cu^{2+}, Zn^{2+})

The general route for the preparation of the metal complexes is presented in **Scheme 5.2**.

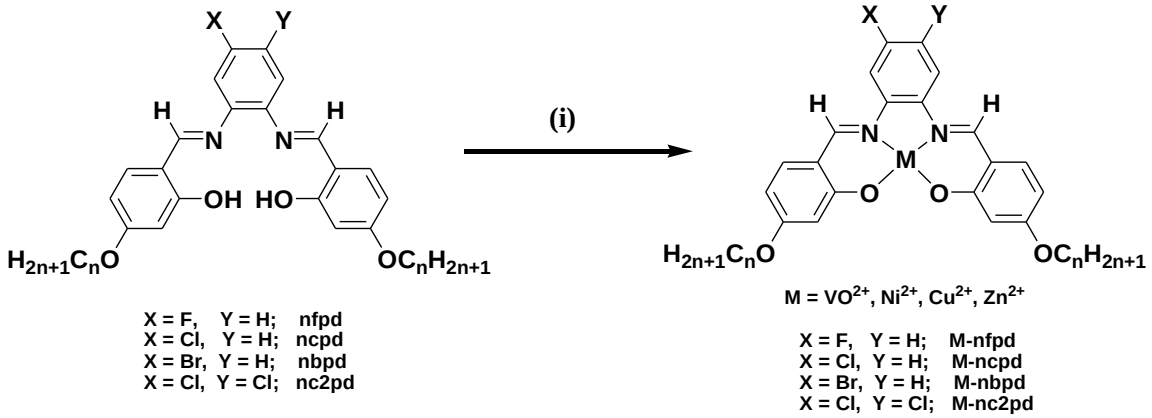

Scheme 5.2: (i) $M(OAc)_2.nH_2O$ (M = Ni^{2+}, Cu^{2+}, Zn^{2+} n = 2,4) / $VOSO_4.H_2O$, MeOH, stir, 3h, r.t.

Synthesis of zinc(II) complexes ; Zn-nfpd, Zn-ncpd, Zn-nbpd and Zn-nc2pd (n = 12, 14, 16, 18).

General procedure:

To a solution of 0.1mmol of imine ligand (**nfpd**, **ncpd**, **nbpd** or **nc2pd**) in ethanol, methanolic solution of zinc(II) acetate dihydrate; $Zn(OAc)_2.2H_2O$ (0.02g, 0.1mmol) was added slowly and stirred for 3h at room temperature. A bright yellow solid formed in each case was filtered, washed with diethyl ether and re-crystallized from chloroform-ethanol (1:1).

Zn-12fpd: Yield = 0.06g (67%); Anal. Calc. for $C_{44}H_{61}FN_2O_4Zn$ (766.35): C, 68.96; H, 8.02; N, 3.66. Found: C, 68.99; H, 7.97; N, 3.70 %. ^{1}H NMR (400 MHz, $CDCl_3$; Me_4Si at 25°C, ppm): δ = 8.36 (s, 1H, $H^{4'}$), 8.31 (s, 1H, H^4), 7.37 (m, 2H, H^6, H^7), 6.90-6.93(m, 2H, H^1, $H^{1'}$), 6.63 (m, 1H, H^5), 6.14 (d, $^4J_{H,H}$ = 2.42 Hz, 2H, H^3), 6.03 (m, 2H, H^2), 3.69 (t, $^3J_{H,H}$ = 6.31 Hz, 4H, O-CH_2), 2.02 (m, 4H, CH_2), 1.26-1.62 (m, 36H, -CH_2), 0.88 (t, $^3J_{H,H}$ = 6.63 Hz, 6H, -CH_3). IR (ν_{max}, cm^{-1}, KBr): 2920 ($\nu_{as(C-H),}$ CH_3), 2849 ($\nu_{s(C-H)}$, CH_3), 1614 ($\nu_{C=N}$), 1315 (ν_{C-O}).

Zn-14fpd: Yield = 0.07g (70%); Anal. Calc. for $C_{48}H_{69}FN_2O_4Zn$ (822.46): C, 70.10; H, 8.46; N, 3.41. Found: C, 70.06; H, 8.49; N, 3.40 %. ^{1}H NMR (400 MHz, $CDCl_3$; Me_4Si at 25°C, ppm): δ = 8.36 (s, 1H, $H^{4'}$), 8.32 (s, 1H, H^4), 7.38 (m, 2H, H^6, H^7), 6.90-6.94(m, 2H, H^1, $H^{1'}$), 6.61 (m, 1H, H^5), 6.14 (d, $^4J_{H,H}$ = 2.45 Hz, 2H, H^3), 6.03 (m, 2H, H^2), 3.70 (t, $^3J_{H,H}$ = 6.31 Hz, 4H, O-CH_2), 2.04 (m, 4H, CH_2), 1.25-1.62 (m, 44H, -CH_2), 0.87 (t, $^3J_{H,H}$ = 6.63 Hz, 6H, -CH_3). IR (ν_{max}, cm^{-1}, KBr): 2919 ($\nu_{as(C-H),}$ CH_3), 2850 ($\nu_{s(C-H)}$, CH_3), 1613 ($\nu_{C=N}$), 1314 (ν_{C-O}).

Zn-16fpd: Yield = 0.08g (72%); Anal. Calc. for $C_{52}H_{77}FN_2O_4Zn$ (878.57): C, 71.09; H, 8.83; N, 3.19. Found: C, 71.07; H, 8.85; N, 3.23 %. ^{1}H NMR (400 MHz, $CDCl_3$; Me_4Si at 25°C, ppm): δ = 8.36 (s, 1H, $H^{4'}$), 8.31 (s, 1H, H^4), 7.38 (m, 2H, H^1, $H^{1'}$), 6.90-6.93 (m, 2H, H^6, H^7), 6.62 (m, 1H, H^5), 6.14 (d, $^4J_{H,H}$ = 2.42 Hz, 2H, H^3), 6.02 (m, 2H, H^2), 3.69 (t, $^3J_{H,H}$ = 6.31 Hz, 4H, O-CH_2), 2.04 (m, 4H, CH_2), 1.26-1.62 (m, 52H, -CH_2), 0.87 (t, $^3J_{H,H}$ = 6.63 Hz, 6H, -CH_3). IR (ν_{max}, cm^{-1}, KBr): 2920 ($\nu_{as(C-H),}$ CH_3), 2850 ($\nu_{s(C-H)}$, CH_3), 1614 ($\nu_{C=N}$), 1315 (ν_{C-O}).

Zn-12cpd: Yield = 0.07g (75%); Anal. Calc. for $C_{44}H_{61}ClN_2O_4Zn$ (782.4): C, 67.51; H, 7.85; N, 3.58. Found: C, 67.52; H, 7.84; N, 3.54. %. ^{1}H NMR (400 MHz, $CDCl_3$; Me_4Si at 25°C, ppm): δ, 8.24 (s, 1H, $H^{4'}$, H^4), 7.73 (d, $^3J_{H,H}$ = 8.53 Hz, H^5), 7.22 (d, 2H, H^7), 7.15 (t, $^3J_{H,H}$ = 8.36, 2H, $H^{1'}$, H^1), 7.01 (dd, $^4J_{H,H}$ = 2.36 Hz, $^3J_{H,H}$ = 8.58 Hz, 2H, H^6), 6.55 (d, $^4J_{H,H}$ = 2.45 Hz, 2H, H^3), 6.38 (dd, $^4J_{H,H}$ = 2.36 Hz, $^3J_{H,H}$ = 8.18 Hz, 2H, H^2), 3.98 (t, $^3J_{H,H}$ = 6.72 Hz, 2H, -OCH_2), 0.90 (m, 40H, -CH_2), 0.89 (t, $^3J_{H,H}$ = 6.83 Hz, 6H, CH_3). IR (ν_{max}, cm^{-1}, KBr): 2924 ($\nu_{as(C-H)}$, CH_3), 2850 ($\nu_{s(C-H)}$, CH_3), 1612 ($\nu_{C=N}$), 1256 (ν_{C-O}).

Zn-14cpd: Yield = 0.07g (76%); Anal. Calc. for $C_{48}H_{69}ClN_2O_4Zn$ (839.4): C, 68.72; H, 8.29; N, 3.34. Found: C, 68.71; H, 8.28; N, 3.35. %. ^{1}H NMR (400 MHz, $CDCl_3$; Me_4Si at 25°C, ppm): δ, 8.21 (s, 1H, $H^{4'}$, H^4), 7.76 (d, $^3J_{H,H}$ = 8.56 Hz, H^5), 7.21 (d, 2H, H^7), 7.14 (t, $^3J_{H,H}$ = 8.35, 2H, $H^{1'}$, H^1), 7.01 (dd, $^4J_{H,H}$ = 2.35 Hz, $^3J_{H,H}$ = 8.38 Hz, 2H, H^6), 6.57 (d, $^4J_{H,H}$ = 2.43 Hz, 2H, H^3), 6.39 (dd, $^4J_{H,H}$ = 2.37 Hz, $^3J_{H,H}$ = 8.18 Hz, 2H, H^2), 3.99 (t, $^3J_{H,H}$ = 6.54 Hz, 2H, -OCH_2), 0.92 (m, 48H, -CH_2), 0.88 (t, $^3J_{H,H}$ = 6.82 Hz, 6H, CH_3). IR (ν_{max}, cm^{-1}, KBr): 2923($\nu_{as(C-H)}$, CH_3), 2847($\nu_{s(C-H)}$, CH_3), 1613($\nu_{C=N}$), 1256 (ν_{C-O}).

Zn-16cpd: Yield = 0.07g (70%); Anal. Calc. for $C_{52}H_{77}ClN_2O_4Zn$ (895.5): C, 69.78; H, 8.67; N, 3.13. Found: C, 69.76; H, 8.68; N, 3.15. %. ^{1}H NMR (400 MHz, $CDCl_3$; Me_4Si at 25°C, ppm): δ, 8.23 (s, 1H, $H^{4'}$, H^4), 7.77 (d, $^3J_{H,H}$ = 8.54 Hz, H^5), 7.26 (d, 2H, H^7), 7.18 (t, $^3J_{H,H}$ = 8.39, 2H, $H^{1'}$, H^1), 7.08 (dd, $^4J_{H,H}$ = 2.34 Hz, $^3J_{H,H}$ = 8.37 Hz, 2H, H^6), 6.56 (d, $^4J_{H,H}$ = 2.45 Hz, 2H, H^3), 6.38 (dd, $^4J_{H,H}$ = 2.37 Hz, $^3J_{H,H}$ = 8.17 Hz, 2H, H^2), 3.95 (t, $^3J_{H,H}$ = 6.56 Hz, 2H, -OCH_2), 0.96 (m, 56H, -CH_2), 0.89 (t, $^3J_{H,H}$ = 6.73 Hz, 6H, CH_3). ^{13}C NMR (75.45 MHz; $CDCl_3$; Me_4Si at 25°C, ppm) δ= 135.6 (-C_1), 109.7(-C_2), 106.9(-C_3), 168.7(-C_{14}), 166.4(-C_4), 114.8(-C_{13}), 133.7(-C_6), 166.2 (-C_{15}). IR (ν_{max}, cm^{-1}, KBr): 2927($\nu_{as(C-H)}$, CH_3), 2865($\nu_{s(C-H)}$, CH_3), 1613($\nu_{C=N}$), 1258 (ν_{C-O}).

Zn-18cpd: Yield = 0.08g (75%); Anal. Calc. for $C_{56}H_{85}ClN_2O_4Zn$ (949.5): C, 70.72; H, 9.01; N, 2.95. Found: C, 70.72; H, 9.02; N, 2.96. %. ^{1}H NMR (400 MHz, $CDCl_3$; Me_4Si at 25°C, ppm): δ, 8.24 (s, 1H, $H^{4'}$, H^4), 7.78 (d, $^3J_{H,H}$ = 8.55 Hz, H^5), 7.29 (d, 2H, H^7), 7.17 (t, $^3J_{H,H}$ = 8.39 Hz, 2H, $H^{1'}$, H^1), 7.08 (dd, $^4J_{H,H}$ = 2.35 Hz, $^3J_{H,H}$ = 8.38 Hz, 2H, H^6), 6.59 (d, $^4J_{H,H}$ = 2.48 Hz, 2H, H^3), 6.38 (dd, $^4J_{H,H}$ = 2.37 Hz, $^3J_{H,H}$ = 8.17 Hz, 2H, H^2), 3.95 (t,

$^{3}J_{H,H}$ = 6.56 Hz, 2H, -OCH_2), 0.97 (m, 64H, -CH_2), 0.91 (t, $^{3}J_{H,H}$ = 6.73 Hz, 6H, CH_3). IR (ν_{max}, cm-1, KBr): 2928($\nu_{as(C-H)}$, CH_3), 2866($\nu_{s(C-H)}$, CH_3), 1611($\nu_{C=N}$), 1255 (ν_{C-O}).

Zn-12bpd: Yield = 0.07g (70%); Anal. Calc. for $C_{44}H_{61}BrN_2O_4Zn$ (827.26): C, 63.88; H, 7.43; N, 3.39. Found: C, 63.90; H, 7.47; N, 3.44 %. ^{1}H NMR (400 MHz, $CDCl_3$; Me_4Si at 25°C, ppm): δ = 8.39 (s, 1H, $H^{4'}$), 8.33 (s, 1H, H^4), 7.54 (m, 2H, H^6, H^7), 6.90-6.93(m, 2H, H^1, $H^{1'}$), 6.64 (m, 1H, H^5), 6.14 (d, $^{4}J_{H,H}$ = 2.43 Hz, 2H, H^3), 6.02 (m, 2H, H^2), 3.69 (t, $^{3}J_{H,H}$ = 6.31 Hz, 4H, O-CH_2), 2.00 (m, 4H, CH_2), 1.25-1.61 (m, 36H, -CH_2), 0.87 (t, $^{3}J_{H,H}$ = 6.64 Hz, 6H, -CH_3). IR (ν_{max}, cm^{-1}, KBr): 2920 ($\nu_{as(C-H),}$ CH_3), 2849 ($\nu_{s(C-H)}$, CH_3), 1610 ($\nu_{C=N}$), 1313 (ν_{C-O}).

Zn-14bpd: Yield = 0.08g (72%); Anal. Calc. for $C_{48}H_{69}BrN_2O_4Zn$ (883.37): C, 65.26; H, 7.87; N, 3.17. Found: C, 65.30; H, 7.91; N, 3.22 %. ^{1}H NMR (400 MHz, $CDCl_3$; Me_4Si at 25°C, ppm): δ = 8.38 (s, 1H, $H^{4'}$), 8.33 (s, 1H, H^4), 7.52 (m, 2H, H^6, H^7), 6.90-6.93 (m, 2H, H^1, $H^{1'}$), 6.63 (m, 1H, H^5), 6.15 (d, $^{4}J_{H,H}$ = 2.40 Hz, 2H, H^3), 6.03 (m, 2H, H^2), 3.70 (t, $^{3}J_{H,H}$ = 6.30 Hz, 4H, O-CH_2), 1.99 (m, 4H, CH_2), 1.26-1.60 (m, 36H, -CH_2), 0.89 (t, $^{3}J_{H,H}$ = 6.63 Hz, 6H, -CH_3). IR (ν_{max}, cm^{-1}, KBr): 2918 ($\nu_{as(C-H),}$ CH_3), 2848 ($\nu_{s(C-H)}$, CH_3), 1610 ($\nu_{C=N}$), 1313 (ν_{C-O}).

Zn-16bpd: Yield = 0.09g (75%); Anal. Calc. for $C_{52}H_{77}BrN_2O_4Zn$ (939.47): C, 66.48; H, 8.26; N, 2.98. Found: C, 66.44; H, 8.29; N, 3.02 %. ^{1}H NMR (400 MHz, $CDCl_3$; Me_4Si at 25°C, ppm): δ = 8.38 (s, 1H, $H^{4'}$), 8.32 (s, 1H, H^4), 7.53 (m, 2H, H^6, H^7), 6.90-6.93 (m, 2H, H^1, $H^{1'}$), 6.64 (m, 1H, H^5), 6.14 (d, $^{4}J_{H,H}$ = 2.41 Hz, 2H, H^3), 6.02 (m, 2H, H^2), 3.69 (t, $^{3}J_{H,H}$ = 6.28 Hz, 4H, O-CH_2), 2.01 (m, 4H, CH_2), 1.25-1.61 (m, 36H, -CH_2), 0.88 (t, $^{3}J_{H,H}$ = 6.65 Hz, 6H, -CH_3). IR (ν_{max}, cm^{-1}, KBr): 2919 ($\nu_{as(C-H),}$ CH_3), 2850 ($\nu_{s(C-H)}$, CH_3), 1609 ($\nu_{C=N}$), 1314 (ν_{C-O}).

Zn-12c2pd: Yield = 0.06g (82%); Anal. Calc. for $C_{44}H_{60}Cl_2N_2O_4Zn$ (817.25): C, 64.66; H, 7.40; N, 3.43. Found: C, 64.69; H, 7.43; N, 3.47 %. ^{1}H NMR (400 MHz, $CDCl_3$; Me_4Si at 25°C, ppm): δ = 8.49 (s, 2H, H^4), 7.29 (s, 2H, H^5), 7.23 (d, $^{3}J_{H,H}$ = 8.0 Hz, 2H, H^1), 6.52 (d, $^{4}J_{H,H}$ = 2.0 Hz, 2H, H^3), 6.47 (dd, $^{3}J_{H,H}$ = 8.0 Hz, $^{4}J_{H,H}$ = 2.0 Hz, 2H, H^2), 3.97 (t, $^{3}J_{H,H}$ = 6.5 Hz, 4H, O-CH_2), 1.79 (m, 4H, CH_2), 1.25-1.60 (m, 36H, CH_2), 0.88 (t, $^{3}J_{H,H}$ = 6.7 Hz,

6H, CH_3). IR (ν_{max}, cm^{-1}, KBr): 2919 ($\nu_{as(C-H),}$ CH_3), 2848 ($\nu_{s(C-H)}$, CH_3), 1609 ($\nu_{C=N}$), 1313 (ν_{C-O}).

Zn-14c2pd: Yield = 0.07g (87%); Anal. Calc. for $C_{48}H_{68}Cl_2N_2O_4Zn$ (873.36): C, 66.01; H, 7.85; N, 3.21. Found: C, 66.03; H, 7.91; N, 3.26 %. ^{1}H NMR (400 MHz, $CDCl_3$; Me_4Si at 25°C, ppm): δ = 8.49 (s, 2H, H^4), 7.29 (s, 2H, H^5), 7.23 (d, $^3J_{H,H}$ = 8.0 Hz, 2H, H^1), 6.52 (d, $^4J_{H,H}$ = 2.0 Hz, 2H, H^3), 6.47 (dd, $^3J_{H,H}$ = 8.0 Hz, $^4J_{H,H}$ = 2.0 Hz, 2H, H^2), 3.97 (t, $^3J_{H,H}$ = 6.5 Hz, 4H, O-CH_2), 1.79 (m, 4H, CH_2), 1.25-1.60 (m, 44H, CH_2), 0.88 (t, $^3J_{H,H}$ = 6.7 Hz, 6H, CH_3). IR (ν_{max}, cm^{-1}, KBr): 2918 ($\nu_{as(C-H),}$ CH_3), 2849 ($\nu_{s(C-H)}$, CH_3), 1608 ($\nu_{C=N}$), 1315 (ν_{C-O}).

Zn-16c2pd: Yield = 0.08g (85%); Anal. Calc. for $C_{52}H_{76}Cl_2N_2O_4Zn$ (929.47): C, 67.20; H, 8.24; N, 3.01. Found: C, 67.17; H, 8.29; N, 3.05 %. ^{1}H NMR (400 MHz, $CDCl_3$; Me_4Si at 25°C, ppm): δ = 8.49 (s, 2H, H^4), 7.30 (s, 2H, H^5), 7.25 (d, $^3J_{H,H}$ = 8.0 Hz, 2H, H^1), 6.52 (d, $^4J_{H,H}$ = 2.0 Hz, 2H, H^3), 6.48 (dd, $^3J_{H,H}$ = 8.0 Hz, $^4J_{H,H}$ = 2.0 Hz, 2H, H^2), 3.98 (t, $^3J_{H,H}$ = 6.5 Hz, 4H, O-CH_2), 1.78 (m, 4H, CH_2), 1.25-1.58 (m, 52H, CH_2), 0.88 (t, $^3J_{H,H}$ = 6.7 Hz, 6H, CH_3). IR (ν_{max}, cm^{-1}, KBr): 2917 ($\nu_{as(C-H),}$ CH_3), 2850 ($\nu_{s(C-H)}$, CH_3), 1608 ($\nu_{C=N}$), 1314 (ν_{C-O}).

Synthesis of nickel(II) complexes; Ni-nfpd, Ni-ncpd, Ni-nbpd and Ni-nc2pd (n = 12, 14, 16).

General procedure:

A solution of $Ni(OAc)_2.4H_2O$ (0.02g, 0.1mmol) in methanol was added to a solution of the corresponding salphen ligand (0.1mmol) in ethanol under the stirring condition when an orange-red solid begin to appear in suspension that turned into microcrystalline solid on further stirring. The fine orange crystalline precipitate was isolated by filtration, washed with diethyl ether and re-crystallized from chloroform-ethanol (1:1).

Ni-12fpd: Yield = 0.07g (77%); Anal. Calc. for $C_{44}H_{61}FN_2O_4Ni$ (759.66): C, 69.57; H, 8.09; N, 3.69. Found: C, 69.61; H, 8.04; N, 3.71 %. ^{1}H NMR (400 MHz, $CDCl_3$; Me_4Si at 25°C, ppm): δ = 7.96 (s, 1H, $H^{4'}$), 7.93 (s, 1H, H^4), 7.59 (m, 2H, H^6, H^7), 7.17-7.21(m, 2H, H^1, $H^{1'}$), 6.92-6.96 (m, 1H, H^5), 6.61 (d, $^4J_{H,H}$ = 2.53 Hz, 2H, H^3), 6.35 (m, 2H, H^2), 3.96 (t, $^3J_{H,H}$ = 6.43 Hz, 4H, O-CH_2), 1.79 (m, 4H, CH_2), 1.27-1.60 (m, 36H, -CH_2), 0.90 (t,

$^{3}J_{H,H}$ = 6.67 Hz, 6H, -CH_3). IR (ν_{max}, cm^{-1}, KBr): 2919 ($\nu_{as(C-H),}$ CH_3), 2850 ($\nu_{s(C-H)}$, CH_3), 1611 ($\nu_{C=N}$), 1322 (ν_{C-O}).

Ni-14fpd: Yield = 0.08g (80%); Anal. Calc. for $C_{48}H_{69}FN_2O_4Ni$ (815.76): C, 70.67; H, 8.53; N, 3.43. Found: C, 70.71; H, 8.50; N, 3.47 %. ^{1}H NMR (400 MHz, $CDCl_3$; Me_4Si at 25°C, ppm): δ = 7.97 (s, 1H, $H^{4'}$), 7.94 (s, 1H, H^4), 7.57 (m, 2H, H^6, H^7), 7.17-7.21(m, 2H, H^1, $H^{1'}$), 6.92-6.96 (m, 1H, H^5), 6.63 (d, $^{4}J_{H,H}$ = 2.51 Hz, 2H, H^3), 6.35 (m, 2H, H^2), 3.97 (t, $^{3}J_{H,H}$ = 6.44 Hz, 4H, O-CH_2), 1.79 (m, 4H, CH_2), 1.28-1.59 (m, 44H, -CH_2), 0.90 (t, $^{3}J_{H,H}$ = 6.68 Hz, 6H, -CH_3). IR (ν_{max}, cm^{-1}, KBr): 2918 ($\nu_{as(C-H),}$ CH_3), 2851 ($\nu_{s(C-H)}$, CH_3), 1610 ($\nu_{C=N}$), 1321 (ν_{C-O}).

Ni-16fpd: Yield = 0.08g (71%); Anal. Calc. for $C_{52}H_{77}FN_2O_4Ni$ (871.87): C, 71.63; H, 8.90; N, 3.21. Found: C, 71.67; H, 8.93; N, 3.24 %. ^{1}H NMR (400 MHz, $CDCl_3$; Me_4Si at 25°C, ppm): δ = 7.96 (s, 1H, $H^{4'}$), 7.93 (s, 1H, H^4), 7.59 (m, 2H, H^6, H^7), 7.17-7.21(m, 2H, H^1, $H^{1'}$), 6.92-6.96 (m, 1H, H^5), 6.61 (d, $^{4}J_{H,H}$ = 2.55 Hz, 2H, H^3), 6.33 (m, 2H, H^2), 3.97 (t, $^{3}J_{H,H}$ = 6.42 Hz, 4H, O-CH_2), 1.79 (m, 4H, CH_2), 1.28-1.59 (m, 56H, -CH_2), 0.90 (t, $^{3}J_{H,H}$ = 6.67 Hz, 6H, -CH_3). IR (ν_{max}, cm^{-1}, KBr): 2918 ($\nu_{as(C-H),}$ CH_3), 2850 ($\nu_{s(C-H)}$, CH_3), 1610 ($\nu_{C=N}$), 1322 (ν_{C-O}).

Ni-12cpd: Yield = 0.07g (74%); Anal. Calc. for $C_{44}H_{61}ClN_2O_4Ni$ (776.11): C, 68.09; H, 7.92; N, 3.61. Found: C, 68.05; H, 7.96; N, 3.64%. ^{1}H NMR (400 MHz, $CDCl_3$; Me_4Si at 25°C, ppm): δ = 7.97 (s, 1H, $H^{4'}$), 7.94 (s, 1H, H^4), 7.56-7.58 (m, 2H, H^6, H^7), 7.18-7.20 (m, 2H, H^1, $H^{1'}$), 7.14 (m, 1H, H^5), 6.58 (d, $^{4}J_{H,H}$ = 2.39 Hz, 2H, H^3), 6.30-6.34 (m, 2H, H^2), 3.96 (t, $^{3}J_{H,H}$ = 6.33 Hz, 4H, O-CH_2), 1.79 (m, 4H, CH_2), 1.28-1.59 (m, 44H, -CH_2), 0.90 (t, $^{3}J_{H,H}$ = 6.47 Hz, 6H, -CH_3). IR (ν_{max}, cm^{-1}, KBr): 2917 ($\nu_{as(C-H),}$ CH_3), 2850 ($\nu_{s(C-H)}$, CH_3), 1610 ($\nu_{C=N}$), 1320 (ν_{C-O}).

Ni-14cpd: Yield = 0.08g (73%); Anal. Calc. for $C_{48}H_{69}ClN_2O_4Ni$ (832.22): C, 69.27; H, 8.36; N, 3.37. Found: C, 69.33; H, 7.32; N, 3.41 %. ^{1}H NMR (400 MHz, $CDCl_3$; Me_4Si at 25°C, ppm): δ = 7.98 (s, 1H, $H^{4'}$), 7.95 (s, 1H, H^4), 7.56-7.59 (m, 2H, H^6, H^7), 7.18-7.20 (m, 2H, H^1, $H^{1'}$), 7.15 (m, 1H, H^5), 6.58 (d, $^{4}J_{H,H}$ = 2.40 Hz, 2H, H^3), 6.31-6.36 (m, 2H, H^2), 3.96 (t, $^{3}J_{H,H}$ = 6.31 Hz, 4H, O-CH_2), 1.79 (m, 4H, CH_2), 1.28-1.59 (m, 44H, -CH_2), 0.90

(t, $^{3}J_{H,H}$ = 6.45 Hz, 6H, -CH_3). IR (ν_{max}, cm^{-1}, KBr): 2918 ($\nu_{as(C-H),}$ CH_3), 2851 ($\nu_{s(C-H)}$, CH_3), 1611 ($\nu_{C=N}$), 1321 (ν_{C-O}).

Ni-16cpd: Yield = 0.08g (71%); Anal. Calc. for $C_{52}H_{77}ClN_2O_4Ni$ (888.33): C, 70.31; H, 8.74; N, 3.15. Found: C, 70.33; H, 8.70; N, 3.20 %. ^{1}H NMR (400 MHz, $CDCl_3$; Me_4Si at 25°C, ppm): δ = 7.98 (s, 1H, $H^{4'}$), 7.95 (s, 1H, H^4), 7.56-7.58 (m, 2H, H^6, H^7), 7.18-7.20 (m, 2H, H^1, $H^{1'}$), 7.14 (m, 1H, H^5), 6.58 (d, $^{4}J_{H,H}$ = 2.38 Hz, 2H, H^3), 6.30-6.34 (m, 2H, H^2), 3.96 (t, $^{3}J_{H,H}$ = 6.29 Hz, 4H, O-CH_2), 1.79 (m, 4H, CH_2), 1.28-1.59 (m, 56H, -CH_2), 0.90 (t, $^{3}J_{H,H}$ = 6.42 Hz, 6H, -CH_3). IR (ν_{max}, cm^{-1}, KBr): 2918 ($\nu_{as(C-H),}$ CH_3), 2851 ($\nu_{s(C-H)}$, CH_3), 1610 ($\nu_{C=N}$), 1321 (ν_{C-O}).

Ni-12bpd: Yield = 0.08g (74%); Anal. Calc. for $C_{44}H_{61}BrN_2O_4Ni$ (820.56): C, 64.40; H, 7.49; N, 3.41. Found: C, 64.44; H, 7.39; N, 3.37 %. ^{1}H NMR (400 MHz, $CDCl_3$; Me_4Si at 25°C, ppm): δ = 8.01 (s, 1H, $H^{4'}$), 7.98 (s, 1H, H^4), 7.76 (m, 2H, H^6, H^7), 7.52-7.55 (m, 2H, H^1, $H^{1'}$), 7.17-7.22 (m, 1H, H^5), 6.61 (d, $^{4}J_{H,H}$ = 2.40 Hz, 2H, H^3), 6.32-6.36 (m, 2H, H^2), 3.97 (t, $^{3}J_{H,H}$ = 6.53 Hz, 4H, O-CH_2), 1.79 (m, 4H, CH_2), 1.28-1.58 (m, 36H, -CH_2), 0.90 (t, $^{3}J_{H,H}$ = 6.78 Hz, 6H, -CH_3). IR (ν_{max}, cm^{-1}, KBr): 2918 ($\nu_{as(C-H),}$ CH_3), 2850 ($\nu_{s(C-H)}$, CH_3), 1610 ($\nu_{C=N}$), 1321 (ν_{C-O}).

Ni-14bpd: Yield = 0.09g (74%); Anal. Calc. for $C_{48}H_{69}BrN_2O_4Ni$ (876.67): C, 65.76; H, 7.93; N, 3.20. Found: C, 65.74; H, 7.97; N, 3.23 %. ^{1}H NMR (400 MHz, $CDCl_3$; Me_4Si at 25°C, ppm): δ = 8.02 (s, 1H, $H^{4'}$), 7.99 (s, 1H, H^4), 7.74 (m, 2H, H^6, H^7), 7.51-7.53 (m, 2H, H^1, $H^{1'}$), 7.17-7.22 (m, 1H, H^5), 6.61 (d, $^{4}J_{H,H}$ = 2.45 Hz, 2H, H^3), 6.32-6.36 (m, 2H, H^2), 3.97 (t, $^{3}J_{H,H}$ = 6.56 Hz, 4H, O-CH_2), 1.79 (m, 4H, CH_2), 1.28-1.58 (m, 44H, -CH_2), 0.90 (t, $^{3}J_{H,H}$ = 6.82 Hz, 6H, -CH_3). IR (ν_{max}, cm^{-1}, KBr): 2916 ($\nu_{as(C-H),}$ CH_3), 2850 ($\nu_{s(C-H)}$, CH_3), 1610 ($\nu_{C=N}$), 1320 (ν_{C-O}).

Ni-16bpd: Yield = 0.09g (72%); Anal. Calc. for $C_{52}H_{77}BrN_2O_4Ni$ (932.78): C, 66.96; H, 8.32; N, 3.00. Found: C, 67.00; H, 8.29; N, 2.98 %. ^{1}H NMR (400 MHz, $CDCl_3$; Me_4Si at 25°C, ppm): δ = 8.01 (s, 1H, $H^{4'}$), 7.98 (s, 1H, H^4), 7.76 (m, 2H, H^6, H^7), 7.51-7.53 (m, 2H, H^1, $H^{1'}$), 7.17-7.22 (m, 1H, H^5), 6.61 (d, $^{4}J_{H,H}$ = 2.42 Hz, 2H, H^3), 6.32-6.36 (m, 2H, H^2), 3.97 (t, $^{3}J_{H,H}$ = 6.55 Hz, 4H, O-CH_2), 1.79 (m, 4H, CH_2), 1.28-1.58 (m, 56H, -CH_2), 0.90

(t, $^{3}J_{H,H}$ = 6.80 Hz, 6H, -CH_3). IR (ν_{max}, cm^{-1}, KBr): 2916 ($\nu_{as(C-H),}$ CH_3), 2849 ($\nu_{s(C-H)}$, CH_3), 1610 ($\nu_{C=N}$), 1321 (ν_{C-O}).

Ni-12c2pd: Yield = 0.06g (80%); Anal. Calc. for $C_{44}H_{60}Cl_2N_2O_4Ni$ (810.56): C, 65.20; H, 7.46; N, 3.46. Found: C, 65.23; H, 7.43; N, 3.47 %. ^{1}H NMR (400 MHz, $CDCl_3$; Me_4Si at 25°C, ppm): δ = 7.92 (s, 2H, H^4), 7.71 (s, 2H, H^5), 7.19 (d, $^{3}J_{H,H}$ = 8.0 Hz, 2H, H^1), 6.58 (d, $^{4}J_{H,H}$ = 2.0 Hz, 2H, H^3), 6.37 (dd, $^{3}J_{H,H}$ = 8.0 Hz, $^{4}J_{H,H}$ = 2.0 Hz, 2H, H^2), 3.99 (t, $^{3}J_{H,H}$ = 6.6 Hz, 4H, O-CH_2), 1.80 (m, 4H, CH_2), 1.25-1.60 (m, 36H, CH_2), 0.89 (t, $^{3}J_{H,H}$ = 6.7 Hz, 6H, CH_3). IR (ν_{max}, cm^{-1}, KBr): 2919 ($\nu_{as(C-H),}$ CH_3), 2851 ($\nu_{s(C-H)}$, CH_3), 1610 ($\nu_{C=N}$), 1314 (ν_{C-O}).

Ni-14c2pd: Yield = 0.06g (78%); Anal. Calc. for $C_{48}H_{68}Cl_2N_2O_4Ni$ (866.66): C, 66.52; H, 7.91; N, 3.23. Found: C, 66.55; H, 7.93; N, 3.27 %. ^{1}H NMR (400 MHz, $CDCl_3$; Me_4Si at 25°C, ppm): δ = 7.90 (s, 2H, H^4), 7.72 (s, 2H, H^5), 7.18 (d, $^{3}J_{H,H}$ = 8.0 Hz, 2H, H^1), 6.60 (d, $^{4}J_{H,H}$ = 2.0 Hz, 2H, H^3), 6.36 (dd, $^{3}J_{H,H}$ = 8.0 Hz, $^{4}J_{H,H}$ = 2.0 Hz, 2H, H^2), 3.98 (t, $^{3}J_{H,H}$ = 6.7 Hz, 4H, O-CH_2), 1.79 (m, 4H, CH_2), 1.25-1.59 (m, 44H, CH_2), 0.90 (t, $^{3}J_{H,H}$ = 6.8 Hz, 6H, CH_3). IR (ν_{max}, cm^{-1}, KBr): 2918 ($\nu_{as(C-H),}$ CH_3), 2850 ($\nu_{s(C-H)}$, CH_3), 1612 ($\nu_{C=N}$), 1314 (ν_{C-O}).

Ni-16c2pd: Yield = 0.07g (75%); Anal. Calc. for $C_{52}H_{76}Cl_2N_2O_4Ni$ (922.77): C, 67.68; H, 8.30; N, 3.04. Found: C, 67.71; H, 8.27; N, 3.07 %. ^{1}H NMR (400 MHz, $CDCl_3$; Me_4Si at 25°C, ppm): δ = 7.91 (s, 2H, H^4), 7.71 (s, 2H, H^5), 7.19 (d, $^{3}J_{H,H}$ = 8.0 Hz, 2H, H^1), 6.60 (d, $^{4}J_{H,H}$ = 2.0 Hz, 2H, H^3), 6.35 (dd, $^{3}J_{H,H}$ = 8.0 Hz, $^{4}J_{H,H}$ = 2.0 Hz, 2H, H^2), 3.99 (t, $^{3}J_{H,H}$ = 6.7 Hz, 4H, O-CH_2), 1.80 (m, 4H, CH_2), 1.28-1.58 (m, 52H, CH_2), 0.90 (t, $^{3}J_{H,H}$ = 6.5 Hz, 6H, CH_3). IR (ν_{max}, cm^{-1}, KBr): 2918 ($\nu_{as(C-H),}$ CH_3), 2850 ($\nu_{s(C-H)}$, CH_3), 1611 ($\nu_{C=N}$), 1319 (ν_{C-O}).

Synthesis of copper(II) complexes; Cu-nfpd, Cu-ncpd, Cu-nbpd and Cu-nc2pd (n = 12, 14, 16)

General procedure:

To a solution of the salphen ligand **nfpd** or **ncpd** or **nbpd** (0.1mmol) in ethanol, methanolic solution of $Cu(OAc)_2.2H_2O$ (0.02g, 0.1mmol) was added which was immediately

accompanied by brown coloration. The mixture was stirred for 3h at room temperature and the brown solid so formed was isolated by filtration, washed with diethyl ether and recrystallized from chloroform-ethanol(1:1).

Cu-12fpd: Yield = 0.06g (67%); Anal. Calc. for $C_{44}H_{61}FN_2O_4Cu$ (764.51): C, 69.13; H, 8.04; N, 3.66. Found: C, 69.16; H, 8.01; N, 3.69 %. IR (ν_{max}, cm^{-1}, KBr): 2919 ($\nu_{as(C-H),}$ CH_3), 2849 ($\nu_{s(C-H)}$, CH_3), 1614 ($\nu_{C=N}$), 1317 (ν_{C-O}).

Cu-14fpd: Yield = 0.07g (70%); Anal. Calc. for $C_{48}H_{69}FN_2O_4Cu$ (820.62): C, 70.25; H, 8.48; N, 3.41. Found: C, 70.21; H, 8.45; N, 3.46 %. IR (ν_{max}, cm^{-1}, KBr): 2920 ($\nu_{as(C-H),}$ CH_3), 2850 ($\nu_{s(C-H)}$, CH_3), 1615 ($\nu_{C=N}$), 1316 (ν_{C-O}).

Cu-16fpd: Yield = 0.08g (71%); Anal. Calc. for $C_{52}H_{77}FN_2O_4Cu$ (876.72): C, 71.24; H, 8.85; N, 3.20. Found: C, 71.21; H, 8.89; N, 3.19 %. IR (ν_{max}, cm^{-1}, KBr): 2919 ($\nu_{as(C-H),}$ CH_3), 2850 ($\nu_{s(C-H)}$, CH_3), 1615 ($\nu_{C=N}$), 1317 (ν_{C-O}).

Cu-12cpd: Yield = 0.06g (65%); Anal. Calc. for $C_{44}H_{61}ClN_2O_4Cu$ (780.97): C, 67.67; H, 7.87; N, 3.59. Found: C, 67.70; H, 7.84; N, 3.62 %. IR (ν_{max}, cm^{-1}, KBr): 2920 ($\nu_{as(C-H),}$ CH_3), 2850 ($\nu_{s(C-H)}$, CH_3), 1617 ($\nu_{C=N}$), 1316 (ν_{C-O}).

Cu-14cpd: Yield = 0.07g (68%); Anal. Calc. for $C_{48}H_{69}ClN_2O_4Cu$ (837.07): C, 68.87; H, 8.31; N, 3.35. Found: C, 68.91; H, 8.29; N, 3.31 %. IR (ν_{max}, cm^{-1}, KBr): 2920 ($\nu_{as(C-H),}$ CH_3), 2849 ($\nu_{s(C-H)}$, CH_3), 1618 ($\nu_{C=N}$), 1316 (ν_{C-O}).

Cu-16cpd: Yield = 0.08g (69%); Anal. Calc. for $C_{52}H_{77}ClN_2O_4Cu$ (893.18): C, 69.93; H, 8.69; N, 3.14. Found: C, 69.91; H, 8.73; N, 3.16 %. IR (ν_{max}, cm^{-1}, KBr): 2921 ($\nu_{as(C-H),}$ CH_3), 2851 ($\nu_{s(C-H)}$, CH_3), 1618 ($\nu_{C=N}$), 1315 (ν_{C-O}).

Cu-12bpd: Yield = 0.07g (70%); Anal. Calc. for $C_{44}H_{61}BrN_2O_4Cu$ (825.42): C, 64.02; H, 7.45; N, 3.39. Found: C, 64.04; H, 7.46; N, 3.35 %. IR (ν_{max}, cm^{-1}, KBr): 2920 ($\nu_{as(C-H),}$ CH_3), 2850 ($\nu_{s(C-H)}$, CH_3), 1610 ($\nu_{C=N}$), 1317 (ν_{C-O}).

Cu-14bpd: Yield = 0.07g (73%); Anal. Calc. for $C_{48}H_{69}BrN_2O_4Cu$ (881.52): C, 65.40; H, 7.89; N, 3.18. Found: C, 65.43; H, 7.92; N, 3.22 %. IR (ν_{max}, cm^{-1}, KBr): 2919 ($\nu_{as(C-H),}$ CH_3), 2850 ($\nu_{s(C-H)}$, CH_3), 1610 ($\nu_{C=N}$), 1316 (ν_{C-O}).

Cu-16bpd: Yield = 0.08g (73%); Anal. Calc. for $C_{52}H_{77}BrN_2O_4Cu$ (937.63): C, 66.61; H, 8.28; N, 2.99. Found: C, 66.65; H, 8.31; N, 3.03 %. IR (ν_{max}, cm^{-1}, KBr): 2918 ($\nu_{as(C-H),}$ CH_3), 2851 ($\nu_{s(C-H)}$, CH_3), 1610 ($\nu_{C=N}$), 1318 (ν_{C-O}).

Cu-12c2pd: Yield = 0.07g (86%); Anal. Calc. for $C_{44}H_{60}Cl_2N_2O_4Cu$ (815.41): C, 64.81; H, 7.42; N, 3.44. Found: C, 64.84; H, 7.46; N, 3.47 %. IR (ν_{max}, cm^{-1}, KBr): 2920 ($\nu_{as(C-H),}$ CH_3), 2849 ($\nu_{s(C-H)}$, CH_3), 1600 ($\nu_{C=N}$), 1314 (ν_{C-O}).

Cu-14c2pd: Yield = 0.07g (82%); Anal. Calc. for $C_{48}H_{68}Cl_2N_2O_4Cu$ (871.52): C, 66.15; H, 7.86; N, 3.21. Found: C, 66.21; H, 7.89; N, 3.25 %. IR (ν_{max}, cm^{-1}, KBr): 2920 ($\nu_{as(C-H),}$ CH_3), 2849 ($\nu_{s(C-H)}$, CH_3), 1600 ($\nu_{C=N}$), 1316 (ν_{C-O}).

Cu-16c2pd: Yield = 0.07g (80%); Anal. Calc. for $C_{52}H_{76}Cl_2N_2O_4Cu$ (927.62): C, 67.33; H, 8.26; N, 3.02. Found: C, 67.38; H, 8.31; N, 3.05 %. IR (ν_{max}, cm^{-1}, KBr): 2917 ($\nu_{as(C-H),}$ CH_3), 2850 ($\nu_{s(C-H)}$, CH_3), 1599 ($\nu_{C=N}$), 1318 (ν_{C-O}).

Synthesis of oxovanadium(IV) complexes; VO-nfpd, VO-ncpd, VO-nbpd and VO-nc2pd (n = 12, 14, 16).

General procedure:

To a solution of the salphen ligand **nfpd** or **ncpd** or **nbpd** or **nc2pd** (0.1mmol) in ethanol, $VOSO_4$. H_2O (0.02g, 0.1mmol) in methanol was added under stirring when the solution acquired a green colour. The addition of a few drops of triethylamine resulted in a green suspension affording microcrystalline solid on further stirring. The light green product was filtered off, washed with diethyl ether and recrystallized from chloroform-ethanol(1:1).

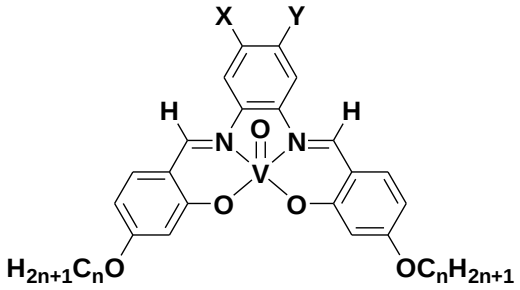

X = F, Y = H; VO-nfpd
X = Cl, Y = H; VO-ncpd
X= Br, Y = H; VO-nbpd
X = Cl, Y = Cl; VO-nc2pd

VO-12fpd: Yield = 0.06g (70%); Anal. Calc. for $C_{44}H_{61}FN_2O_4VO$ (767.91): C, 68.82; H, 8.01; N, 3.65. Found: C, 68.78; H, 8.03; N, 3.69 %. IR (ν_{max}, cm^{-1}, KBr): 2918 ($\nu_{as(C-H),}$ CH_3), 2849 ($\nu_{s(C-H)}$, CH_3), 1615 ($\nu_{C=N}$), 1313 (ν_{C-O}), 967 ($\nu_{V=O}$).

VO-14fpd: Yield = 0.07g (73%); Anal. Calc. for $C_{48}H_{69}FN_2O_4VO$ (824.01): C, 69.96; H, 8.44; N, 3.40. Found: C, 69.99; H, 8.41; N, 3.44 %. IR (ν_{max}, cm^{-1}, KBr): 2919 ($\nu_{as(C-H),}$ CH_3), 2849 ($\nu_{s(C-H)}$, CH_3), 1616 ($\nu_{C=N}$), 1314 (ν_{C-O}), 966 ($\nu_{V=O}$).

VO-16fpd: Yield = 0.07g (71%); Anal. Calc. for $C_{52}H_{77}FN_2O_4VO$ (880.12): C, 70.96; H, 8.82; N, 3.18. Found: C, 71.01; H, 8.78; N, 3.21 %. IR (ν_{max}, cm^{-1}, KBr): 2919 ($\nu_{as(C-H),}$ CH_3), 2850 ($\nu_{s(C-H)}$, CH_3), 1616 ($\nu_{C=N}$), 1313 (ν_{C-O}), 966 ($\nu_{V=O}$).

VO-12cpd: Yield = 0.07g (72%); Anal. Calc. for $C_{44}H_{61}ClN_2O_4VO$ (784.36): C, 67.38; H, 7.84; N, 3.57. Found: C, 67.41; H, 7.81; N, 3.61 %. IR (ν_{max}, cm^{-1}, KBr): 2918 ($\nu_{as(C-H),}$ CH_3), 2849 ($\nu_{s(C-H)}$, CH_3), 1614 ($\nu_{C=N}$), 1311 (ν_{C-O}), 969 ($\nu_{V=O}$).

VO-14cpd: Yield = 0.07g (71%); Anal. Calc. for $C_{48}H_{69}ClN_2O_4VO$ (840.47): C, 68.59; H, 8.27; N, 3.33. Found: C, 68.55; H, 8.31; N, 3.35 %. IR (ν_{max}, cm^{-1}, KBr): 2919 ($\nu_{as(C-H),}$ CH_3), 2850 ($\nu_{s(C-H)}$, CH_3), 1615 ($\nu_{C=N}$), 1312 (ν_{C-O}), 969 ($\nu_{V=O}$).

VO-16cpd: Yield = 0.08g (72%); Anal. Calc. for $C_{52}H_{77}ClN_2O_4VO$ (896.57): C, 69.66; H, 8.66; N, 3.12. Found: C, 69.70; H, 8.63; N, 3.16 %. IR (ν_{max}, cm^{-1}, KBr): 2919 ($\nu_{as(C-H),}$ CH_3), 2850 ($\nu_{s(C-H)}$, CH_3), 1615 ($\nu_{C=N}$), 1311 (ν_{C-O}), 968 ($\nu_{V=O}$).

VO-12bpd: Yield = 0.07g (73%); Anal. Calc. for $C_{44}H_{61}BrN_2O_4VO$ (828.81): C, 63.76; H, 7.42; N, 3.38. Found: C, 63.80; H, 7.39; N, 3.42 %. IR (ν_{max}, cm^{-1}, KBr): 2918 ($\nu_{as(C-H),}$ CH_3), 2849 ($\nu_{s(C-H)}$, CH_3), 1615 ($\nu_{C=N}$), 1311 (ν_{C-O}), 968 ($\nu_{V=O}$).

VO-14bpd: Yield = 0.08g (73%); Anal. Calc. for $C_{48}H_{69}BrN_2O_4VO$ (884.92): C, 65.15; H, 7.86; N, 3.17. Found: C, 65.19; H, 7.87; N, 3.20 %. IR (ν_{max}, cm^{-1}, KBr): 2920 ($\nu_{as(C-H),}$ CH_3), 2848 ($\nu_{s(C-H)}$, CH_3), 1614 ($\nu_{C=N}$), 1312 (ν_{C-O}), 967 ($\nu_{V=O}$).

VO-16bpd: Yield = 0.09g (75%); Anal. Calc. for $C_{52}H_{77}BrN_2O_4VO$ (941.02): C, 66.37; H, 8.25; N, 2.98. Found: C, 66.33; H, 8.27; N, 3.02 %. IR (ν_{max}, cm^{-1}, KBr): 2918 ($\nu_{as(C-H),}$ CH_3), 2849 ($\nu_{s(C-H)}$, CH_3), 1615 ($\nu_{C=N}$), 1311 (ν_{C-O}), 968 ($\nu_{V=O}$).

VO-12c2pd: Yield = 0.06g (75%); Anal. Calc. for $C_{44}H_{60}Cl_2N_2O_4VO$ (818.81): C, 64.54; H, 7.39; N, 3.42. Found: C, 64.57; H, 7.43; N, 3.45 %. IR (ν_{max}, cm^{-1}, KBr): 2918 ($\nu_{as(C-H),}$ CH_3), 2849 ($\nu_{s(C-H)}$, CH_3), 1608 ($\nu_{C=N}$), 1313 (ν_{C-O}), 971 ($\nu_{V=O}$).

VO-14c2pd: Yield = 0.06g (77%); Anal. Calc. for $C_{48}H_{68}Cl_2N_2O_4VO$ (874.91): C, 65.89; H, 7.83; N, 3.20. Found: C, 65.91; H, 7.87; N, 3.24 %. IR (ν_{max}, cm^{-1}, KBr): 2919 ($\nu_{as(C-H),}$ CH_3), 2848 ($\nu_{s(C-H)}$, CH_3), 1610 ($\nu_{C=N}$), 1314 (ν_{C-O}), 971 ($\nu_{V=O}$).

VO-16c2pd: Yield = 0.06g (73%); Anal. Calc. for $C_{52}H_{76}Cl_2N_2O_4VO$ (931.02): C, 67.08; H, 8.23; N, 3.01. Found: C, 67.13; H, 8.27; N, 3.06 %. IR (ν_{max}, cm^{-1}, KBr): 2919 ($\nu_{as(C-H),}$ CH_3), 2850 ($\nu_{s(C-H)}$, CH_3), 1609 ($\nu_{C=N}$), 1311 (ν_{C-O}), 971 ($\nu_{V=O}$).

5.3. Results and discussion

5.3.1. Mono-substituted salphen ligands

5.3.1.1. Synthesis and structural assessment

The strategy implemented for the synthesis of the mono-substituted salphen ligands [N,N-bis-(4-n-alkoxysalicylidene)-4-fluoro/chloro/bromo-1,2-diaminobenzene], abbreviated as **nfpd**, **ncpd** or **nbpd** (n = 12, 14, 16 and 18 is the number of carbon atoms in alkyl chains) has been summarized in **Scheme 5.1**. The structure of the compounds has been ascertained by elemental analyses, UV-visible, FT-IR, ^{1}H NMR and ^{13}C NMR (for **16cpd** only) spectroscopy. FT-IR spectra of the ligands showed bands corresponding to the $\nu_{C=N}$ and ν_{O-H} vibrations in the region 1619–1629cm^{-1} and at ~3436cm^{-1}, respectively. The ^{1}H NMR spectra of the ligands showed two distinct resonances for phenolic-OH protons at around 13.45ppm and 13.38ppm and two for imine protons at ~8.52ppm and 8.50ppm, respectively (**Fig. 5.1**).

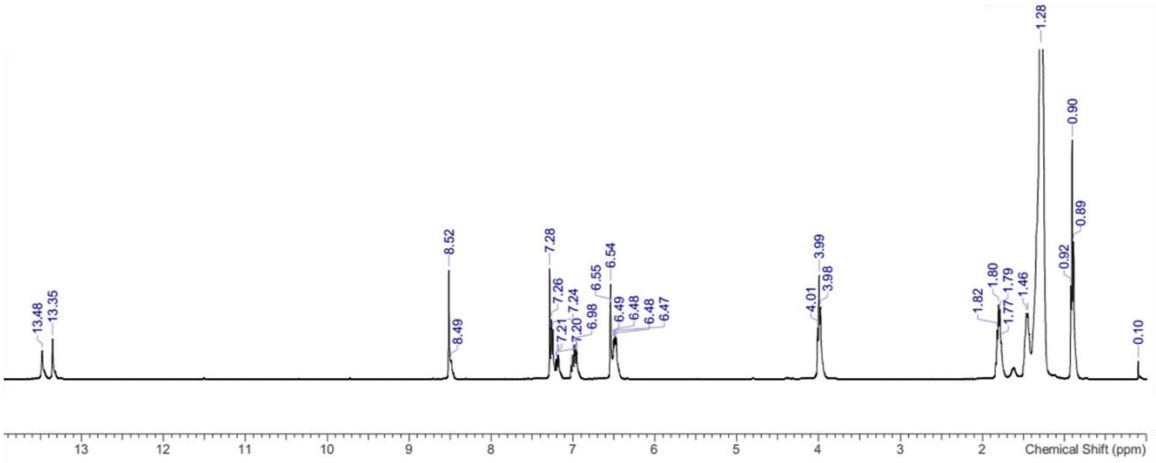

Fig. 5.1: ^{1}H NMR spectrum of a representative ligand (**16fpd**).

5.3.1.2. Liquid crystalline properties

Polarizing optical microscopy and differential scanning calorimetry:

Thermal behaviour of the mono-substituted salphen ligands was studied by polarizing optical microscopy (POM) and differential scanning calorimetry (DSC) studies. Phase transition temperatures and the associated enthalpies of the ligands are summarized in **Table 5.1**.

The salphen ligands (**nfpd**, **ncpd** and **nbpd**) are all mesomorphic. The ligands exhibited broken fan-like optical textures (**Fig. 5.2a-c**) characteristic of columnar phases upon cooling from the isotropic melt. Further, optical textures of **nfpd** and **ncpd** ligands (n = 12, 14, 16) remained unchanged till room temperature attesting room temperature mesmorphism. However, in the case of **nbpd** ligands solidification occurred on further cooling. The liquid crystalline behaviour of these ligands (**nfpd, ncpd** and **nbpd**) contrasts with that of un-substituted, methyl-substituted, nitro-substituted or dichloro-substituted ligands which were all non-mesomorphic.[16,20,21] The subtle interplay between the electronic and steric properties of the halogen substituent at the spacer might be the probable reason. The nature of the phase transitions was monotropic for the ligands as evident from DSC scans (**Table 5.1**) and POM observations. The ligands displayed a single endothermic peak in the heating cycle corresponding to direct melting to an isotropic liquid (**Fig. 5.3**). In the cooling cycle, a single peak pertaining to isotropic liquid-mesophase

transition was observed for **nfpd** and **ncpd** ligands (**Fig. 5.4a and b**). The cooling scan of **nbpd** ligands, however, displayed two peaks corresponding to isotropic liquid-mesophase and mesophase-crystal transitions (**Fig. 5.4c**). An increase in clearing temperature was also noted on changing the substituent at the phenylene spacer from F through Cl to Br in the ligands. Quite a similar trend was noted in the isotropic melt-mesophase transition temperature in the cooling cycle (**Table 5.1**).

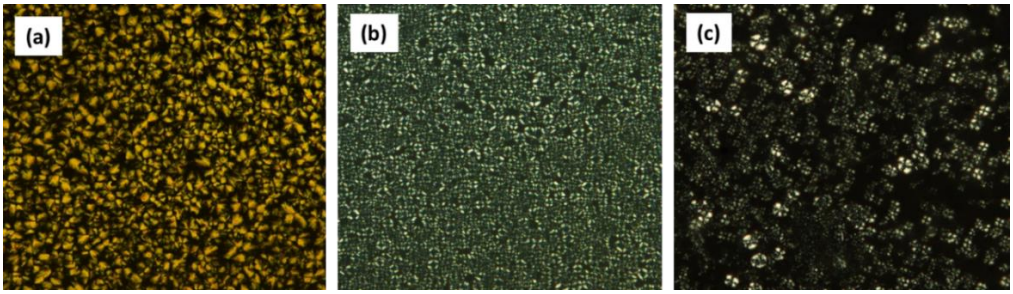

Fig. 5.2: Polarizing optical micrographs of (a) **16fpd** at 29°C, (b) **16cpd** at 30°C and (c) **16bpd** at 50°C.

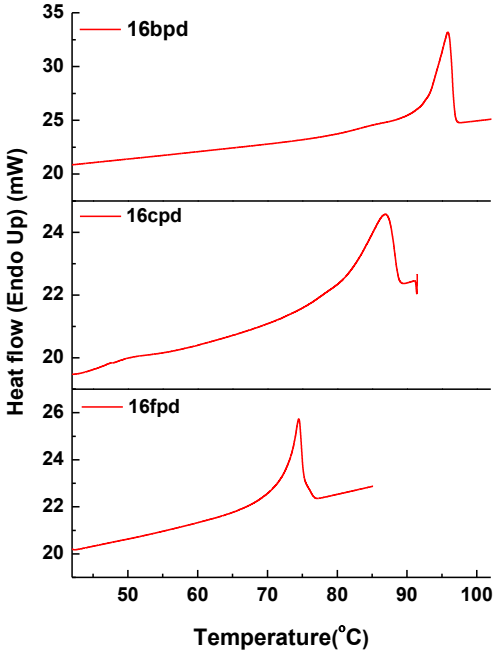

Fig. 5.3: DSC traces (1st heating) of **16fpd**, **16cpd**, and **16bpd**.

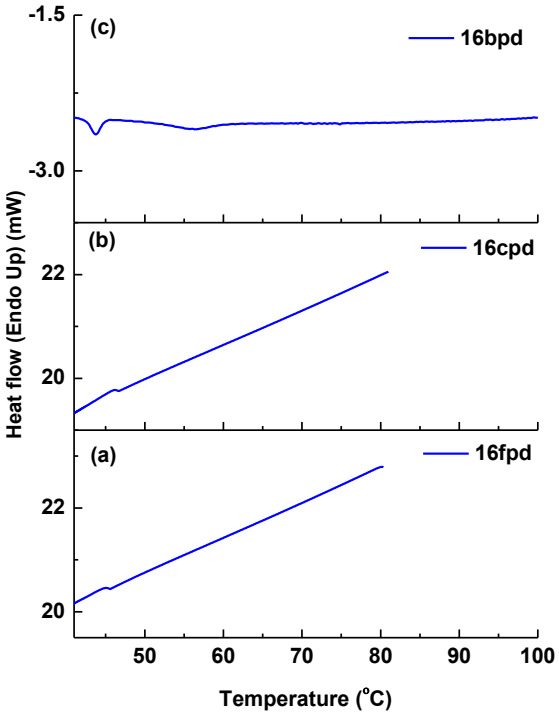

Fig. 5.4: DSC profiles (1st cooling scan) of (a) **16fpd** (b) **16cpd** and (c) **16bpd**.

Table 5.1: Thermodynamic data for the ligands. Transition temperatures are given in °C, and the corresponding enthalpy changes are in parentheses (ΔH; kJ mol^{-1}).

Compounds	Heating cycle[a]	Cooling cycle[a]
12fpd	Cr 84 (20.7) I	I 52 (0.7) Col_o
14fpd	Cr 79 (23.8) I	I 49 (1.2) Col_o
16fpd	Cr 75 (25.6) I	I 45 (0.9) Col_o
12cpd	Cr 96 (37.6) I	I 56 (1.2) Col_r
14cpd	Cr 91 (33.4) I	I 51 (0.9) Col_r
16cpd	Cr 87 (46.9) I	I 48 (0.7) Col_r
18cpd	Cr 84 (41.7) I	I 45 (0.5) Col_r
12bpd	Cr 107 (62.2) I	I 68 (1.1) Col_h 52 (1.2) Cr
14bpd	Cr 101 (62.2) I	I 62 (1.4) Col_h 49 (1.5) Cr
16bpd	Cr 96 (92.9) I	I 57 (1.3) Col_h 43 (1.4) Cr

[a]DSC peak temperature. Cr: crystalline; Col_o: columnar oblique phase; Col_r: rectangular columnar phase; Col_h: hexagonal columnar phase.

Variable temperature PXRD study:

Phase assignments were confirmed by variable temperature powder X-ray diffraction measurements. The C-16 ligands (**16fpd**, **16cpd**, and **16bpd**) were selected as representative.

The XRD pattern of **16fpd**, measured at 28°C (**Fig. 5.5a**) displayed a series of Bragg diffraction peaks in the low-angle region in accordance with an oblique columnar phase with a *p1* space group symmetry (**Table 5.2**). [29,30] Along with these reflections, an intense halo corresponding to the molten state of the alkyl chains was observed at 3.9 Å. The lattice parameters *a*, *b* and γ were estimated to be 39.4 Å, 56.6 Å, and 67.2°, respectively. However, no separate core-core peak was detected at wider angles, suggesting a weaker correlation between the cores within the column.

Diffractogram of **16cpd**, at 25°C, also displayed a number of reflections in the small angle region (**Fig. 5.5b**). Profile fitting of the data, in this case, fitted well to an rectangular columnar phase (Col_r) (**Table 5.2**).[31] Based on X-ray indexation and extinction rules, the symmetry of the mesophase was assigned to be *p2mm* (for *p2mm*: hk: no conditions, h0: no conditions, 0k: no conditions).[31] Additionally, a broad scattering halo was seen at 4.2 Å which could be ascribed to the liquid-like order of molten alkyl chains. The lattice parameters a_r and b_r calculated from the observed *d* spacings are correspondingly, 36.2 Å and 35.7 Å. In this case too, no feature corresponding to the stacking of the aromatic cores was observed at wider angles.

The XRD pattern of **16bpd**, recorded at 40°C (**Fig. 5.5c**), consisted of a single intense reflection in the small-angle region with a Bragg's spacing of 53.4 Å (**Table 5.2**) and was indexed to the fundamental (100) reflection of a two-dimensional hexagonal lattice (a = 61.7 Å).[29] The absence of additional reflections in the small angle region is indicative of a high disorder along each column. The bulky bromine substituent at the ligand spacer, in this case, is believed to sterically restrict closer association of molecules compared to the rest. At wide angles, a diffuse halo was observed at 4.3 Å corresponding to the liquid-like correlation of molten alkyl chains.

The absence of additional features in the wide-angle region for the ligands precluded an unambiguous interpretation of the stacking of molecular cores within the columns in the

mesophase. The lack of stronger inter-mesogen correlations in the ligands is attributed to the greater flexibility of the mesogenic cores.

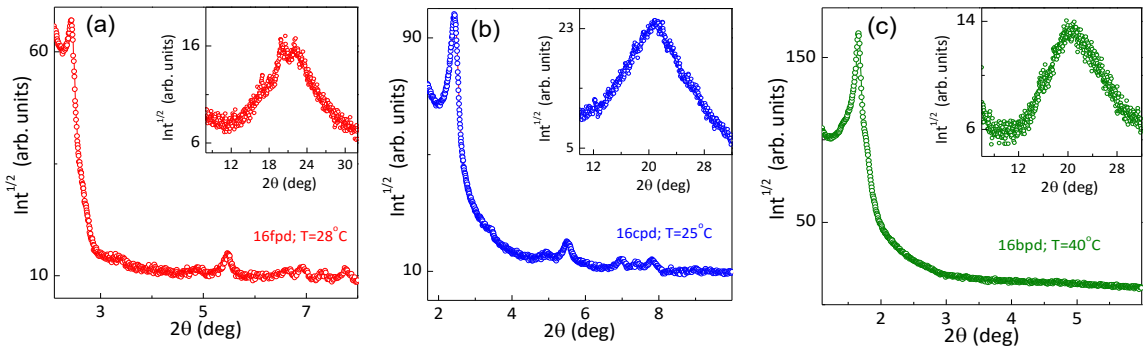

Fig. 5.5: One-dimensional intensity vs. 2θ profile of (a) **16fpd**, (b) **16cpd** and (c) **16bpd**.

Table 5.2: X-ray diffraction data of the ligands.

Compounds	Temperature (°C)	$d_{meas.}$/Å[a]	$d_{calc.}$/Å[a]	Miller indices(hkl)[b]	Mesophase parameters[c]
16fpd	28	36.3	36.3	100	Col_o, *p1*
		26.1	26.1	020	a_o = 39.4 Å
		18.1	18.1	120	b_o = 56.6 Å
		16.2	16.0	-230	γ = 67.2°
		13.4	13.3	-240	S_o = 2052.3 Å^2
		12.8	12.8	220	V_{cell} = 8085.9 Å^3
		12.0	12.1	300	
		11.8	11.3	-340	
		5.3	5.2	010	
		4.9	4.9	110	
		4.5	4.5	-711	
		4.3	4.3	-930	
		3.9(diffuse)	–	–	
16cpd	25	36.2	36.2	100	Col_r, *p2mm*
		17.8	17.8	020	a_r = 36.2 Å
		16.0	16.0	120	b_r = 35.7 Å
		12.7	12.7	220	S_r = 1292.3 Å^2
		11.9	11.9	030	V_{cell} = 5492.4 Å^3
		11.3	11.3	130	
		4.9	5.1	550	
		4.2(diffuse)	–	–	
16bpd	40	53.4	53.4	100	Col_h, *p6mm*
		4.3(diffuse)	–	–	a_h = 61.7 Å
					S_r = 3292.6 Å^2
					V_{cell} = 14158.1 Å^3

[a] $d_{meas.}$ and $d_{calc.}$ are the experimentally measured and calculated diffraction spacings. [b] [*hkl*] are the Miller indices of the reflections. [c] Phase parameters, Col_o phase: $1/d_{hk} = 1/\sin\gamma \sqrt{\{(h/a_o)^2 + (k/b_o)^2 - (2hk\cos\gamma/a_o b_o)\}}$, γ is columnar tilt angle;

lattice area, $S_o = a_o b_o sin\gamma$; columnar cross-section, $S_{col} = a_o b_o/2$. Col_r phase: $a_r = d_{10}$; $1/d_{hk} = \sqrt{\{(h/a_r)^2 + (k/b_r)^2\}}$; columnar cross-section in the rectangular cell, $S_r = a_r b_r$. Col_h phase: $<d_{10}> = 1/N_{hk}\sqrt{[\sum_{hk} d_{hk}(h^2 + k^2 + hk)]}$, where N_{hk} is the number of hk reflections and $a = 2<d_{10}>/\sqrt{3}$; lattice area (columnar cross-section), $S_h = a^2(\sqrt{3})/2$. V_{cell}, volume of an elementary cell: Col_o phase, $V_{cell} = a_o b_o sin\gamma \times h$; Col_r phase, $V_{cell} = a_r b_r \times h$, where h is intra-columnar repeating distance.

A very significant role is thus, played by spacer group modification in tuning the mesomorphism of these salphen ligands. Varying the nature and (or) size of the substituent at the spacer brings about interesting changes in the mesophase behaviour of these compounds influencing strongly the thermal stability and/or nature of the two-dimensional packing of the columns in the lattice. The currently studied salphen ligands with electron withdrawing halogen substituent (F, Cl, Br) at the phenylene spacer exhibit mesophase at or above room temperature, whereas, the hitherto reported ligands without any or, with an electron donating methyl substituent or an electron withdrawing nitro substituent were all non-mesomorphic.[16,20,21] An increase in the melting and clearing temperature is also observed in the present salphen systems upon changing the substituent at the spacer from F to Br through Cl (Table 1). The effect on the molecular organization within the lattice is even more dramatic. The F atom is too small to produce a significant steric effect. Thus, the electronic effect of the fluorine atom in **nfpd**, and electronic coupled with the steric effect of heavier Cl and Br atoms in **ncpd** and **nbpd** ligands might be responsible for the change in intermolecular forces that lead to the variation in the mesophase behaviour of the ligands (**Table 5.2**).

5.3.1.3. Photophysical properties

The absorption and emission spectra of the ligands were recorded at room temperature in dichloromethane solution (10^{-5} M) and in the solid state.

Absorption spectra of the salphen ligands (**nfpd**, **ncpd**, and **nbpd**) consisted of a broad absorption band with maxima at ~ 290nm and between 329-336nm accompanied by a shoulder at longer wavelengths, respectively, corresponding to the π–π* transitions of the aromatic rings and the imine units (**Fig. 5.6 and Table 5.3**). Alkyl chain length variation had no effect on these features.

Photoluminescence studies of the salphen ligands were carried out at room temperature both in dichloromethane solution (10^{-5}M) and in the solid state. In solution, the emission

maxima of the salphen ligands were located at 442nm for **16fpd**, 451nm for **16cpd** and 455nm for **16bpd**, respectively (**Fig. 5.6**). Emission intensity of the ligands were found to decrease in the order **16bpd** > **16cpd** > **16fpd**. This might be attributed to higher electronegativity of the halogens in going from Br to F. This increases the energy gap between HOMO and LUMO of the fluorinated ligand more than the rest. Thus, the number of molecules undergoing transition decreases, which explains the reduced luminescence intensity and the blue shift for **16fpd** compared to the rest. Emission quantum yields (EQY) in solution were in the range 4-10% for the ligands (**Table 5.3**). Previously reported unsubstituted or monosubstituted ligands were, however, non-luminescent.[16,20,21]

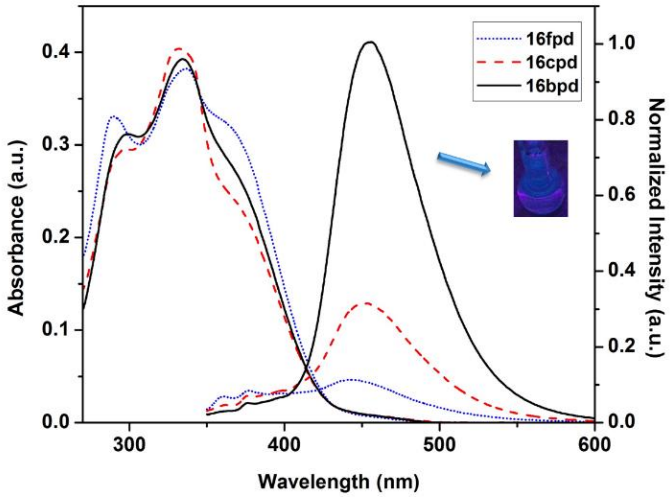

Fig. 5.6: Absorption(left) and photoluminescence(right) spectra ($\lambda_{exc.}$ = 336nm) of the ligands in dichloromethane solution (1×10^{-5} M, r.t.)

The solid state emission spectra of the ligands were recorded on thin films (**Fig. 5.7**). All the ligands showed green luminescence and the emission maxima was positioned at ~530nm, which is considerably red-shifted to that in solution. Moreover, the emission intensity got reduced in the solid state following closer association of molecular cores as compared to the solution. EQY values in the solid state were in the range 2-6%.

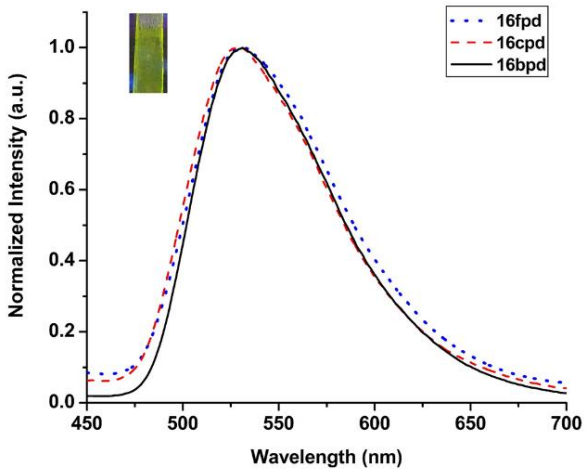

Fig. 5.7: Photoluminescence spectra of the ligands ($\lambda_{exc.}$ = 386nm) in the solid state.

Emission spectra of the room temperature liquid crystalline salphen ligands (**16fpd** and **16cpd**) were also recorded in the mesophase, at room temperature, after prior heating to the isotropic point followed by rapid cooling to ambient temperature. A red-shifted emission ($\lambda_{em.}$= 532nm) was observed in the mesophase compared to those in the solution and the solid state (**Fig. 5.8**).

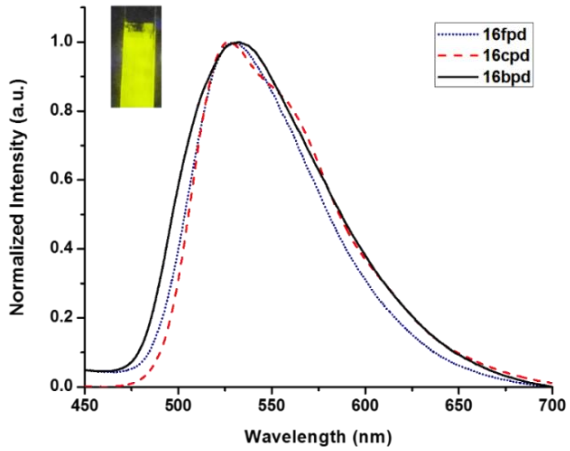

Fig. 5.8: Photoluminescence spectra of the ligands ($\lambda_{exc.}$ = 386nm) in the mesophase. Inset shows the PL image of **16cpd** obtained on irradiation with a light of wavelength 366nm.

Table 5.3: The optical absorption and photoluminescence data of the ligands in dichloromethane solution and in the solid state at 298 K.

Compounds	λ_{abs}^{max} [nm] ($\varepsilon/10^4$) [$M^{-1}cm^{-1}$]	λ_{em}^{max} [nm] (solution)	λ_{em}^{max} [nm] (solid)
12fpd	289(3.3), 336(3.9), 351(3.3)	442	
14fpd	289(3.5), 335(4.0), 350(3.5)	-do-	
16fpd	289(3.3), 336(3.8), 350(3.4)	-do-	530
12cpd	292(2.9), 328(4.1), 356(2.7)	451	
14cpd	292(2.8), 329(3.9), 355(2.6)	-do-	
16cpd	292(2.9), 329(4.0), 356(2.6)	-do-	530
18cpd	292(3.0), 329(4.2), 356(2.7)	-do-	
12bpd	292(3.1), 336(4.0), 354(3.1)	455	
14bpd	291(3.1), 336(3.9), 354(3.0)	-do-	
16bpd	292(3.1), 336(3.9), 354(3.0)	-do-	530

5.3.1.4. DFT study

As diffraction quality single crystals could not be isolated, density functional theory (DFT) was used as a tool to determine the energy optimized structure of two representative ligands; **16fpd** and **16bpd** (**Fig. 5.9a** and **b**). DFT calculations were carried out using GAUSSIAN 09 program package.[33] The ground state geometry optimization in the gas phase of the ligands has been performed using the three-parameter fit of Becke's hybrid functional combined with the Lee-Yang-Parr correlation functional termed as B3LYP,[34,35] within generalized gradient approximation (GGA) and 6-31+G(d,p), 6-31G(d) and 6-31G basis sets[36] were used for N, O, C and H, respectively, without imposing any symmetry constraint. The appropriate structure of the ligands was confirmed as energy minima by calculating the vibrational frequency and confirming the absence of any imaginary frequencies. The C–X (X = F, Br) bond length are 1.35Å and 1.92Å, respectively, for the ligands **16fpd** and **16bpd** (**Table 5.4**). Dipole moments are found to be 6.20D and 7.14D, respectively.

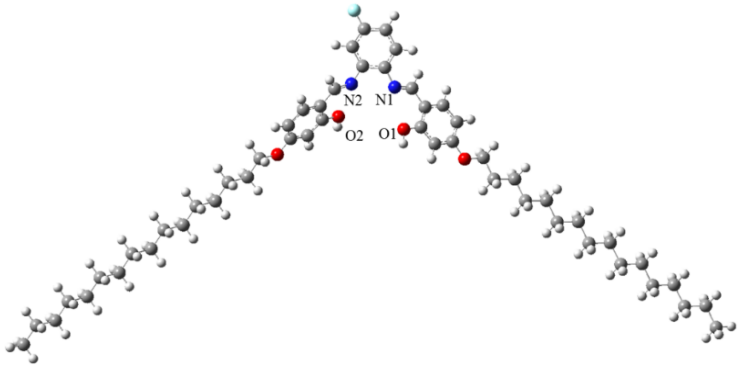

Fig. 5.9a: Optimized electronic structure of **16fpd**.

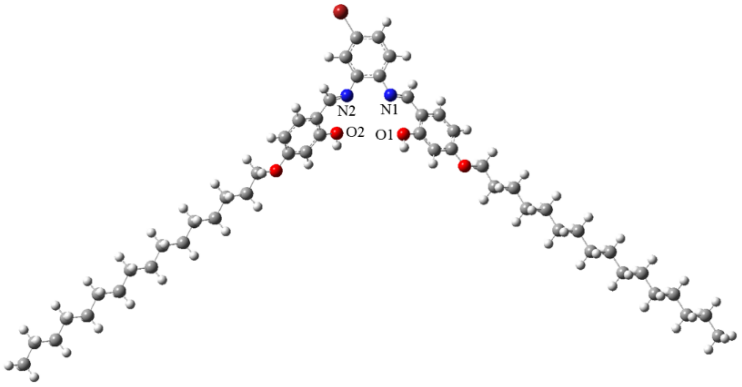

Fig. 5.9b: Optimized electronic structure of **16bpd**.

Table 5.4: Selected bond lengths (Å) and angles (°) and other related parameters of the salphen ligands evaluated at B3LYP level.

Structural parameters	16fpd	16bpd
$C_{ar.}$— O1	1.354	1.354
$C_{ar.}$— O2	1.354	1.354
$C_{ar.}$— N1	1.401	1.401
$C_{ar.}$— N2	1.400	1.400
N1—N2 — O2—O1	25.4	25.0
N1—O1 — O2—N2	-26.6	-26.7
C—X	1.354	1.918
Molecular length (Å)	45.13	45.11
Dipole moment (D)	6.20	7.14

5.3.2. VO(IV) complexes of mono-substituted salphen ligands; VO-nXpd (X = f, c, b)

5.3.2.1. Synthesis and structural assessment

Synthesis of the mononuclear oxovanadium(IV) complexes (**VO-nfpd**, **VO-ncpd**, and **VO-nbpd**) (n = 12, 14, 16) was achieved through a facile and straightforward procedure involving the reaction of the appropriate ligand with vanadyl sulfate in 1:1 molar ratio as depicted in **Scheme 5.2**. The complexes were isolated as light green solids in good yields. The complexes were characterized by elemental analyses, FT-IR, and UV-visible spectroscopy. Analytical data of the compounds were in good agreement with the proposed formulae. FT-IR spectra of the oxovanadium(IV) complexes lacked the weak, broad band due to a hydrogen bonded -OH group, which was observed for the free ligands in the region 3400-3437cm^{-1}, indicating deprotonation of the phenolic oxygen prior to coordination in the complexes. Also, the C=N stretching vibration was shifted to lower wave numbers in the complexes as compared to the free ligands ($\Delta \approx$ 4-15cm^{-1}), indicating azomethine nitrogen coordination to the metal. In addition to the above, the $\nu_{(V=O)}$ stretching mode was observed at relatively higher wave numbers (~966-968cm^{-1}), indicating the absence of any intermolecular ·····V=O·····V=O····· interaction and consistent with monomeric nature of the complexes.[15,37] In polymeric complexes, this band is usually shifted to somewhat lower wave numbers (<900 cm^{-1}) due to linear chain interactions.[37] Absorption spectra of the VO(IV) complexes consisted of two bands at ~ 334nm and ~ 410nm and a shoulder at 427nm (**Fig. 5.10** and **Table 5.5**). These are all ligand centered transitions, bathochromically shifted compared to the ligands, with the longer wavelength features acquiring substantial charge transfer character. Alkyl chain length variation had no effect on the band structures in these complexes.

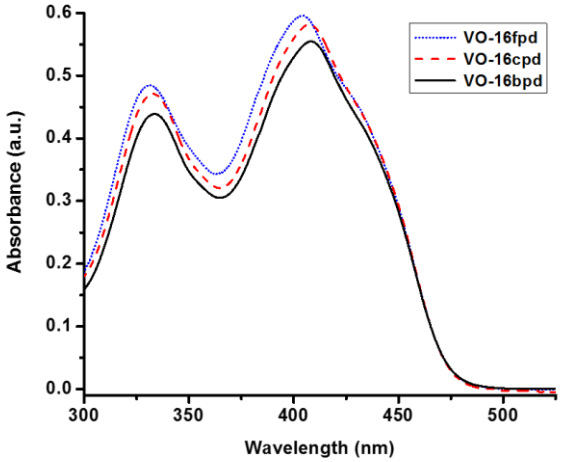

Fig. 5.10: Absorption spectra of oxovanadium(IV) complexes in dichloromethane solution(1×10^{-5} M, r.t.).

Table 5.5: The UV-visible spectral data of VO(IV) complexes in dichloromethane solution at 298K.

Compounds	λ_{abs}^{max} [nm] ($\varepsilon/10^4$; $M^{-1}cm^{-1}$)
VO-12fpd	331(4.5), 404(5.7), 420^{sh}(4.7)
VO-14fpd	331(4.6), 403(5.9), 420^{sh}(4.9)
VO-16fpd	331(4.8), 404(6.0), 420^{sh}(5.1)
VO-12cpd	332(4.6), 407(5.5), 422^{sh}(4.6)
VO-14cpd	332(4.6), 407(5.6), 422^{sh}(4.7)
VO-16cpd	332(4.7), 407(5.8), 422^{sh}(5.0)
VO-12bpd	334(4.4), 406(5.1), 424^{sh}(4.3)
VO-14bpd	333(4.3), 407(5.3), 424^{sh}(4.2)
VO-16bpd	333(4.4), 407(5.5), 424^{sh}(4.6)

sh: shoulder

5.3.2.2. Liquid crystalline properties

Polarizing optical microscopy and differential scanning calorimetry:

Thermal properties of the oxovanadium(IV) complexes were studied using polarizing optical microscopy (POM), differential scanning calorimetry (DSC) and X-ray diffraction

study at variable temperatures (XRD). **Table 5.6** lists the phase transition temperatures and the associated enthalpy data established by DSC.

Complexes of both **VO-nfpd** and **VO-ncpd** series displayed enantiotropic liquid crystalline behaviour. On the contrary, the entire series of **VO-nbpd** complexes were all non-mesomorphic and decomposed at a temperature greater than 280°C. Steric effect of heavier Br atom might be responsible for the observed thermal phenomena, which obscures the extruding oxo group. This prevented any axial weak V=O···V=O interactions which is believed to be crucial to the formation of mesophases.[14,37] Between crossed polarizers, **VO-nfpd** and **VO-ncpd** series of complexes showed birefringence displaying mosaic textures, quite characteristic of columnar phases upon cooling the samples from the isotropic melt (**Fig. 5.11**).[32]. DSC thermogram of **VO-16fpd** displayed four peaks in the heating cycle corresponding to two crystal-crystal and one each of crystal-mesophase and mesophase-isotropic liquid transitions (**Fig. 5.12a**). In the cooling scan, only two peaks were observed corresponding to isotropic liquid-mesophase and mesophase-crystal transitions. **VO-16cpd** displayed three peaks in the heating cycle, one each for crystal-crystal, crystal-mesophase and mesophase-isotropic liquid transitions (**Fig. 5.12b**). In the cooling cycle, only two peaks were observed corresponding to isotropic liquid-mesophase and mesophase-crystal transitions. Clearing temperatures for chloro-substituted complexes were somewhat higher than that for the fluoro-substituted analogs. Quite a similar trend was noted in the isotropic liquid-mesophase transition temperatures. Further, a decrease in both the temperatures was noted on adding carbon atoms in the pendant alkoxy arms.

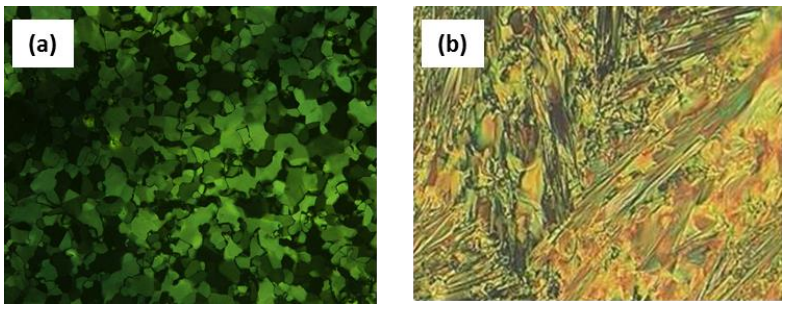

Fig. 5.11: Polarizing optical micrographs of (a) **VO-16fpd at** 188°C and (b) **VO-16cpd** at 221 °C.

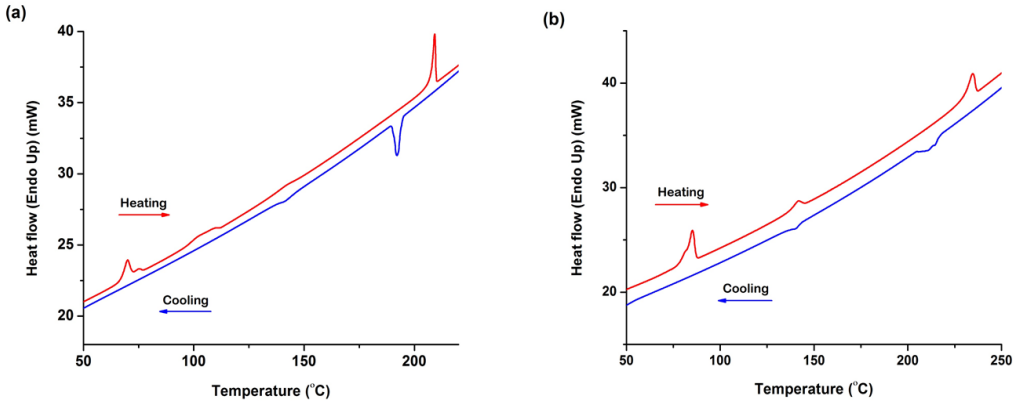

Fig. 5.12: DSC profile of (a) **VO-16fpd** and (b) **VO-16cpd**.

Table 5.6: Thermal data for the **VO-nfpd** and **VO-ncpd** complexes (n =12, 14, 16). Transition temperatures are given in °C, and the corresponding enthalpy changes are in parentheses (ΔH; J/g).

Compounds	Heating cycle[a]	Cooling cycle[a]
VO-12fpd	Cr 77 (27.7) Cr_1 110 (5.7) Cr_2 149 (5.1) Col_r 217 (38.7) I	I 202 (34.8) Col_r 148 (4.6) Cr_2
VO-14fpd	Cr 73 (27.5) Cr_1 108 (5.3) Cr_2 145 (4.7) Col_r 213 (42.4) I	I 197 (33.6) Col_r 145 (5.1) Cr_2
VO-16fpd	Cr 69 (29.1) Cr_1 104 (5.5) Cr_2 142 (4.9) Col_r 209 (40.6) I	I 192 (35.2) Col_r 141 (4.3) Cr_2
VO-12cpd	Cr 70 (27.1) Cr_1 170 (6.8) Col_r 250 (18.6) I	I 225 (25.5) Col_r 169 (5.3) Cr_1
VO-14cpd	Cr 72 (33.6) Cr_1 163 (6.4) Col_r 243 (22.3) I	I 223 (24.2) Col_r 162 (5.8) Cr_1
VO-16cpd	Cr 85 (31.6) Cr_1 142 (7.4) Col_r 235 (20.9) I	I 221 (27.9) Col_r 141 (6.3) Cr_1

[a]DSC peak temperature. Cr, Cr_1, Cr_2 refer to the phases which are crystalline solids, Col_r: rectangular columnar phase.

Variable temperature PXRD study:

In order to confirm the columnar nature of the liquid crystal phases, complexes **VO-16fpd** and **VO-16cpd**, selected as representative examples, were subjected to temperature-dependent powder X-ray diffraction (XRD) measurements.

XRD pattern of **VO-16fpd** at 200 °C, consisted of several reflections in the low angle region (**Fig. 5.13a**). At wide angles, a diffuse and broad-scattering halo was observed at 4.25 Å for the lateral short range order of molten alkyl chains. In addition to that, two sharp wide-angle peaks were seen at 4.1Å and 3.7Å, which are ascribed to 2D-ordering of the

columns. Based on the profile fitting, it may be inferred that the observed spacings correspond to a two-dimensional rectangular columnar phase (Col_r) with a *p2mm* symmetry.[31] The systematic presence of several reflections indicated the long-range order of the 2D arrangements of the columns. The lattice parameters a_r and b_r are found to be 33.82Å and 39.21Å, respectively (**Table 5.7**). The diffractogram at 100°C (**Fig. 5.13b**), however, displayed several sharp reflections both in the small and the wide-angle region which points toward the near crystalline nature of the sample at this temperature. Moreover, the diffuse halo at wide angles corresponding to the short-range order of molten alkyl chains was also poorly resolved. The lattice constant, a_r = 33.82 Å in the mesophase is intermediate between the calculated radius (21Å; *vide infra*) and twice the calculated radius of a fully extended molecule as optimized using DFT. Nevertheless, an exact determination of the molecular packing inside the columns is not possible in the absence of additional features at wide angles, suggesting a weaker correlation between the cores. However, it is assumed that the molecules self-assemble in an somewhat interdigitated and antiparallel disposition (**Fig. 5.13c**) along the column to cover the surface area of the lattice.[38]

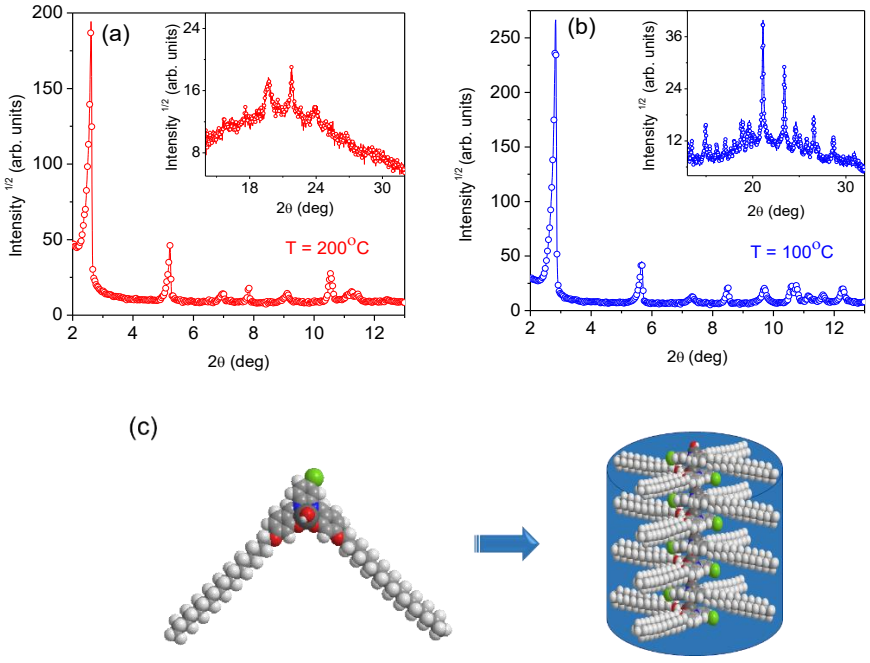

Fig. 5.13: (a) PXRD pattern of **VO-16fpd** at 200°C, (b) PXRD pattern of **VO-16fpd** at 100°C and (c) model for the molecular organization in the mesophase.

The diffraction profile of **VO-16cpd** at 220°C, also consisted of a number of reflections in the low angle region (**Fig. 5.14a**). In the wide angle region, a diffuse halo was observed at 4.47Å, corresponding to the liquid-like correlation between molten alkyl chains. At slightly wider angles, a sharp, less diffuse halo corresponding to a distance of 3.75 Å is attributed to the 2-D ordering of the mesophase. The small-angle reflections agree well with the assignment of a rectangular columnar phase and the extinction rules permit the identification of the *p2mm* rectangular symmetry(for *p2mm*: hk: no conditions, h0: no conditions, 0k: no conditions).[31] The lattice parameters a_r and b_r calculated from the observed *d* spacings are respectively, 18.66 Å and 34.92 Å (**Table 5.7**). The diffraction profile at 100°C (**Fig. 5.14b**) on the other hand, consisted of multiple peaks both at small and wide angles. The features were indicative of a crystalline phase. Moreover, the diffractogram was devoid of any diffuse band at wide angles, in agreement with the crystalline nature of the material. The intercolumnar repeating distance in the mesophase (18.66Å) is comparable to the radius of a fully extended molecule (21Å, DFT computed). Though, additional information regarding the stacking of the molecular cores in the mesophase is not available, it is presumed that the molecules arrange in an antiparallel highly interdigitated fashion within the column, as depicted in **Fig. 5.14c** for an efficient space filling.[38]

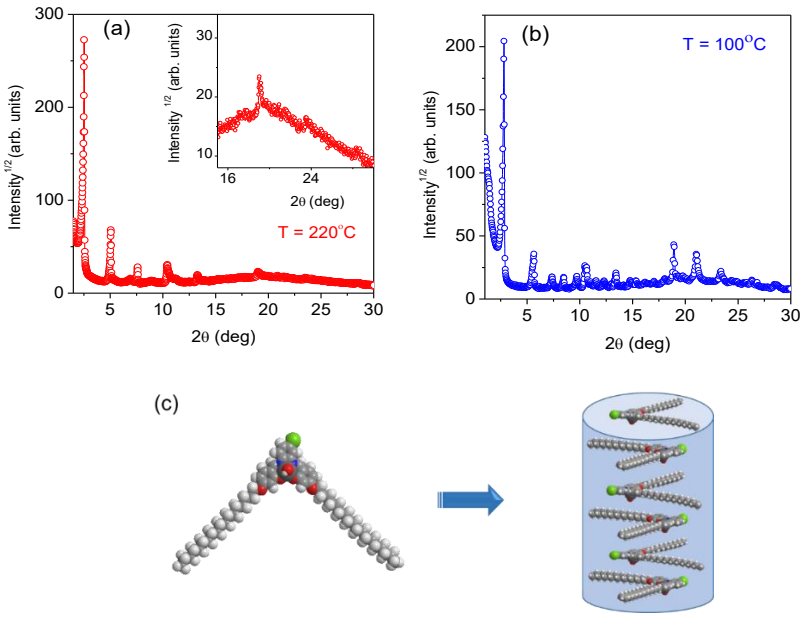

Fig. 5.14: PXRD profile of **VO-16cpd** at (a) 240°C, (b) 100°C and (c) molecular organization in the mesophase.

Previous report on structurally related oxovanadium(IV) complexes, however, showed phase transformation between two rectangular columnar phases (*c2mm*).[15] A textural change was noted for these complexes at lower temperatures. The important point to note is that the ligand framework in those complexes contained an electron-donating methyl substituent at the aromatic spacer. VO(IV) complexes of unsubstituted salphen ligands, on the contrary, did not display such phenomenon and exhibited lamellar columnar mesomorphism.[18] The complexes under current study, however, displayed rectangular columnar mesophase with a *p2mm* symmetry. A marked increase in the clearing temperature is also observed on changing the electron-withdrawing halogen substituent from F to Cl at the aromatic spacer in these systems. Another important aspect is that there is a considerable difference in the lattice constant values of the two series of oxovanadium(IV) complexes, which is contemplated to be associated with the electronic effects of the substituent at the phenylene spacer.

Table 5.7: X-ray diffraction data of the VO(IV) complexes.

	Temperature (°C)	$d_{meas.}$/Å[a]	$d_{calc.}$/Å[b]	**Miller indices(hkl)**[c]	**Mesophase parameters**[d]
VO-16fpd	200	33.82	33.82	100	Col_r, *p2mm*
		16.96	16.96	120	a_r = 33.82 Å
		12.69	12.80	220	b_r = 39.21 Å
		11.29	11.27	300	S_r = 1326.08 Å^2
		9.72	9.77	320	
		8.39	8.46	400	
		7.88	7.84	050	
		7.73	7.76	420	
		6.67	6.67	510	
		6.39	6.39	520	
		4.51	4.49	380	
		4.25(diffuse)	–	–	
		4.08	–	–	
		3.72	–	–	
VO-16cpd	220	34.92	34.92	010	Col_r, *p2mm*
		12.75	12.75	120	a_r = 18.66 Å
		11.64	11.64	030	b_r = 34.92 Å
		9.89	9.88	130	S_r = 651.61 Å^2
		8.50	8.73	040	
		6.65	6.54	150	
		4.65	4.64	350	
		4.47(diffuse)	–	–	
		3.75	–	–	

[a]$d_{meas.}$ and [b]$d_{calc.}$ are the experimentally measured and calculated diffraction spacings. [c][*hkl*] are the Miller indices of the reflections. [d] Phase parameters, Col_r phase: $a_r = d_{10}$; $1/d_{hk} = \sqrt{\{(h/a_r)^2 + (k/b_r)^2\}}$; columnar cross-section in the rectangular cell, $S_r = a_r b_r$. Volume of an elementary cell, $V_{cell} = a_r b_r \times h$, where h is intra-columnar repeating distance.

5.3.2.3. DFT study

As diffraction quality single crystals could not be grown, density functional theory (DFT) study was carried out on a representative VO(IV) complex, **VO-16cpd**, to arrive at the energy optimized structure. DFT calculations were carried out using DMol3 program package.[39] The ground state geometry optimization in the gas phase has been performed using the restricted BLYP(Becke-Lee-Yang-Parr)/ DNP(double-numerical atomic orbitals augmented by polarization functions) methods without imposing any symmetry constraint.[35] Spin restricted calculation has been performed in the framework of the generalized gradient approximation(GGA). The BLYP functional, at the GGA level, used throughout this study, comprises of a hybrid exchange functional as defined by Becke and the non-local Lee-Yang-Parr correlation functional.[35] The basis set chosen is DNP, the double- numerical atomic orbitals augmented by polarization functions. Relativistic effects were taken into account with an all-electron scalar relativistic method based on the Douglas–Kroll–Hess(DKH) transformation. The appropriate structure of the complex (**Fig. 5.15**) was confirmed as energy minima by calculating the vibrational frequency and confirming the absence of any imaginary frequencies. The average V–O and V–N bond lengths were respectively, 1.9Å and 2.1Å (**Table 5.8**). The O–V–O and N–V–N bond angles were about 87.2° and 76.9°; suggestive of a distorted square pyramidal geometry around the vanadium center.

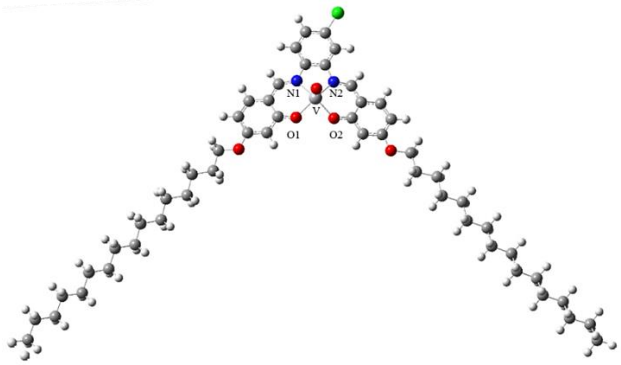

Fig. 5.15: Optimized electronic structure of a representative complex (**VO-16cpd**).

Table 5.8: Selected bond lengths (Å) and angles (°) and other related parameters of **VO-16cpd** evaluated at BLYP level.

Structural parameters	VO-16cpd
V—O1	1.971
V—O2	1.969
V—N1	2.122
V—N2	2.116
V=O	1.615
O1— V— O2	87.2
N1 — V—N2	76.9
N1 — V—O1	86.7
N2 — V—O2	48.9
N1—N2 — O2—O1	1.1
N1—O1 — O2—N2	-1.0
Molecular length (Å)	42.1

5.3.3. Ni(II) complexes of mono-substituted salphen ligands; Ni-nXpd (X = f, c, b)

5.3.3.1. Synthesis and structural assessment

The strategy implemented for the synthesis of the mononuclear Ni(II) complexes (**Ni-nfpd**, **Ni-ncpd** or **Ni-nbpd**; n = 12, 14 and 16) derived from respective salphen ligands has been summarized in **Scheme 5.2**. The structure of the complexes was ascertained by elemental analyses, UV-visible, FT-IR and ^{1}H NMR spectroscopy. FT-IR spectra of the ligands had bands corresponding to the $\nu_{C=N}$ and ν_{O-H} vibrations in the region 1619–1629cm^{-1} and at ~3436cm^{-1}, respectively. The IR spectra of the corresponding Ni(II) complexes showed shifts of $\nu_{C=N}$ vibrations to lower wave numbers with respect to the free ligands and absence of ν_{O-H} vibrations, suggesting the coordination of the imine nitrogen and phenolate oxygen to the Ni(II) center. The ^{1}H NMR spectra of the Ni(II) complexes lacked signal for the phenolic –OH protons, indicating coordination via phenolate oxygen. The signals for the imine protons were observed at ~ 7.98ppm and ~7.95ppm, respectively (**Fig. 5.16**). An upfield shift (~0.56ppm) in the peak position of the –N=CH protons with respect to the free ligands validated the azomethine nitrogen coordination in the complexes.

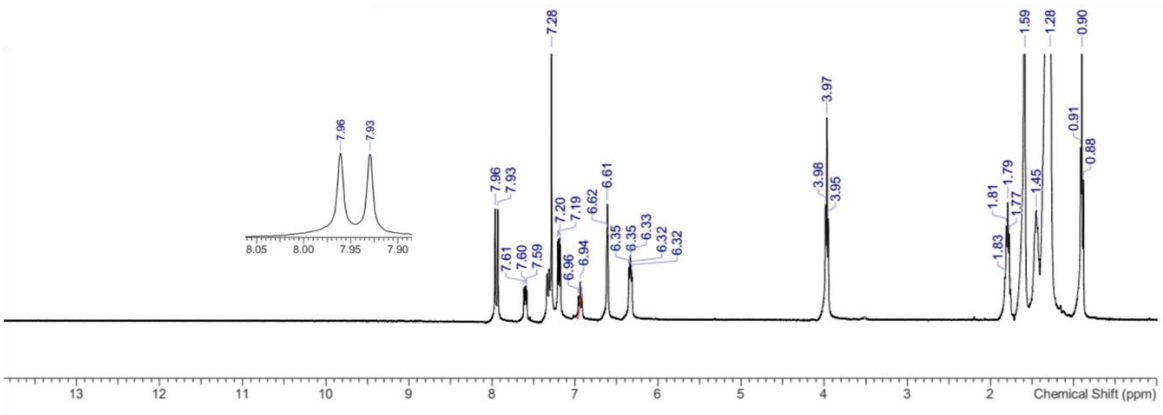

Fig. 5.16: ^{1}H NMR spectrum of a representative Ni(II) complex (**Ni-16fpd**).

5.3.3.2. Liquid crystalline properties

Polarizing optical microscopy and differential scanning calorimetry:

Phase transition temperatures of the complexes and the associated enthalpy data established by DSC are listed in **Table 5.9**.

The Ni(II) complexes displayed enantiotropic liquid crystalline behaviour. Upon cooling the samples from the isotropic melt, **Ni-nfpd**, **Ni-ncpd** and **Ni-nbpd** (n = 12, 14, 16) showed birefringence displaying textures consisting of fan-like defects or a grainy pattern, which are quite characteristic of columnar phases (**Fig. 5.17a-c**).[40] DSC profile of the Ni(II) complexes showed first-order transitions at the phase transition temperatures, typical of crystal and liquid crystalline phases as established by repetitive heating-cooling scans. A total of four crests were observed in each case, two each in the heating and cooling cycle (**Fig. 5.18a-c**). In particular, **Ni-16fpd** showed a transition from a columnar oblique (Col_o) to columnar rectangular (Col_r) phase above 80°C. The low-temperature Col_o phase is stable upto room temperature. Similar behaviour has been noted earlier for Co(II) complexes derived from 2,6-Bis[3,4,5-tri(alkoxy)phenyliminomethyl]pyridines, where a phase transformation from columnar oblique to columnar rectangular phase was observed.[29] In the case of **Ni-16cpd**, the Col_r mesophase at higher temperature was stable till ambient temperature slowly freezing into a glassy state on subsequent cooling. Quite apart, **Ni-16bpd** solidified on further cooling with no glassy behaviour detected. No trend was visible in the melting and clearing temperatures of the complexes as a function of the

substituent at the aromatic spacer. However, a gradual decrease in the clearing temperature was observed with increasing number of carbon atoms in the pendant alkoxy arm in the respective series. The isotropic liquid-mesophase transition temperature also displayed similar trends with increasing chain length.

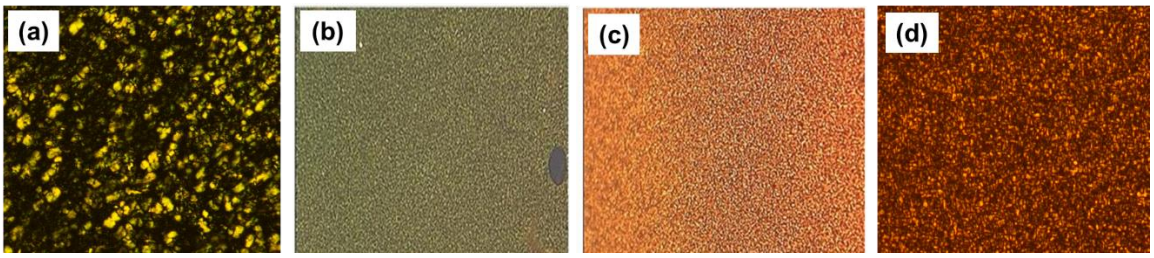

Fig. 5.17: Optical micrographs of (a) **Ni-16fpd** at 99°C, (b) **Ni-16fpd** at 25°C, (c) **Ni-16cpd** at 130°C, and (d) **Ni-16bpd** at 110°C.

Table 5.9: Thermodynamic data for the Ni(II) complexes. Transition temperatures are given in °C, and the corresponding enthalpy changes are in parentheses (ΔH; J/g).

Compounds	Heating cycle[a]	Cooling cycle[a]
Ni-12fpd	Col_o 88 (8.6) Col_r 147 (11.1) I	I 118 (16.1) Col_r 87 (3.5) Col_o
Ni-14fpd	Col_o 84 (6.4) Col_r 141(7.6) I	I 111 (9.7) Col_r 80 (5.2) Col_o
Ni-16fpd	Col_o 80 (7.0) Col_r 136(9.3) I	I 108 (12.8) Col_r 75 (4.6) Col_o
Ni-12cpd	Cr 105 (29.6) Col_r 172 (5.2) I	I 149 (13.8) Col_r 80 (4.3) G
Ni-14cpd	Cr 97 (23.5) Col_r 167 (6.3) I	I 143 (11.7) Col_r 76 (6.5) G
Ni-16cpd	Cr 93 (30.3) Col_r 161 (6.9) I	I 136 (10.6) Col_r 73 (6.1) G
Ni-12bpd	Cr 94 (34.6) Col_r 155 (11.1) I	I 129 (19.5) Col_r 69 (14.6) Cr
Ni-14bpd	Cr 91 (41.3) Col_r 151 (8.1) I	I 124 (12.9) Col_r 60 (11.2) Cr
Ni-16bpd	Cr 87 (16.2) Col_r 139 (4.4) I	I 115 (16.3) Col_r 52 (9.6) Cr

[a]: Peak temperature

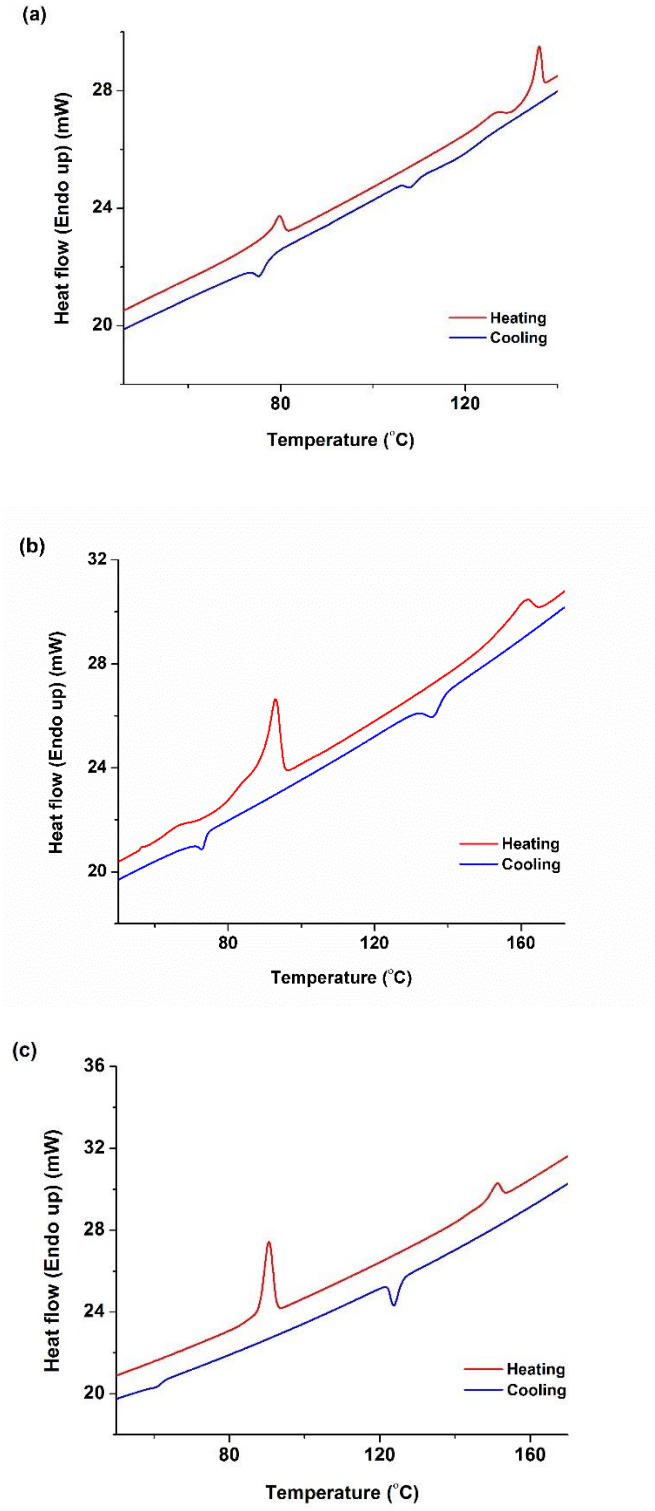

Fig. 5.18: DSC profile of (a) **Ni-16fpd**, (b) **Ni-16cpd** and (c) **Ni-14bpd**.

Variable temperature PXRD study:

In order to confirm the mesophase identification, **Ni-16fpd**, **Ni-16cpd** and **Ni-16bpd** were selected as a representative example to be subjected to temperature dependent powder X-ray diffraction measurements.

The powder XRD pattern of **Ni-16fpd** at 110°C consisted of five small angle peaks corresponding to both the fundamental and higher orders of reflections (**Fig. 5.19a**). In fact, the second small angle reflection was far from being a second harmonic of the first peak, indicating the existence of no simple layer structure. Moreover, the sharpness of the small angle reflections suggests an ordered mesophase structure. These peaks could be indexed to a primitive rectangular columnar lattice (*p2mm*) (**Table 5.10**).[31] The lattice parameters are evaluated as a_r = 19.55 Å and b_r = 33.89 Å. At wide angles, a diffuse halo was observed at 4.5Å due to the liquid-like correlation of molten alkyl chains. However, a second less intense halo corresponding to the stacking of molecular cores was not observed, suggesting a weaker correlation between the cores. The intercolumnar repeating distance in the mesophase is comparable to the radius of a fully extended molecule (21 Å) (*vide-infra*). Thus, it is assumed that two half-disc shaped molecules arrange in an anti-parallel interdigitated fashion to cover the surface area of the lattice (**Fig. 5.22a**).[38] The diffractogram at 80°C (**Fig. 5.19b**), however, fitted well to an oblique columnar phase with a *p1* symmetry.[29,30,32] The small-angle region consisted of a number of reflections. Along with these signatures, a diffuse and broad-scattering halo was observed at wide-angles and was centered at 4.5 Å, corresponding to the short-range correlations of the molten alkyl chains. The lattice parameters a_o, b_o and γ in the Col_o phase were deduced as 52.75 Å, 40 Å, and 83.3°, respectively (**Table 5.10**). Core-core interaction gets significantly enhanced at lower temperatures as stronger core-core interactions are required for the formation of an oblique columnar phase. The lattice constant a_o, in this case, is slightly greater than twice the radius of a fully extended molecule, thus, it is presumed that two molecules arrange in a back to back fashion to cover the surface area of a disc (**Fig. 5.22b**). However, in the absence of additional information, further insight could not be gained about the packing of molecules within the column and that of columns in the monoclinic lattice.

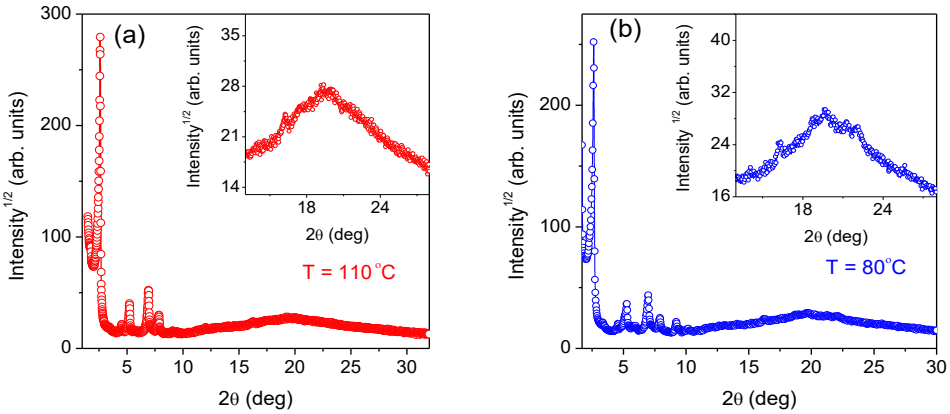

Fig. 5.19: PXRD profile of **Ni-16fpd** at (a) 110°C and (b) at 80°C.

The diffractogram of **Ni-16cpd** at 140°C, displayed a strong maximum accompanied by other relatively weak reflections in the low-angle region (**Fig. 5.20a**). At wide angles, a diffuse halo was observed with a d-spacing value of 4.6 Å corresponding to the liquid-like order of the molten alkyl chains. A second peak in the wide-angle region, corresponding to short-range π–π stacking interactions of the molecular cores was, however, not detected, suggesting weaker correlations amid the cores.[31] The proposed indexation coupled with the extinction rules matched well to a rectangular columnar phase with a *p2mm* symmetry (for *p2mm*: hk: no conditions, h0: no conditions, 0k: no conditions).[31] Lattice parameters a_r and b_r evaluated from the observed *d* spacings are respectively, 19.57Å and 33.95Å (**Table 5.10**). The DFT optimized radius of a fully extended molecule (21Å) is comparable to the intercolumnar repeating distance, thus, it can be deduced that the columnar cross-section is formed by approximately two semi-discoid molecules arranged in an anti-parallel fashion with partial interdigitation of molten alkyl chains (**Fig. 5.22a**).[38] The XRD spectrum recorded at 50°C (**Fig. 5.20b**) was quite similar to that recorded at higher temperatures. The proposed indexation was in good agreement with the assignment of a rectangular columnar phase (*p2mm*); the presence of a diffuse reflection at wide angles and the absence of any mixed-index reflections at low angles rules out the phase being crystalline in nature at this temperature. Lattice parameters a_r and b_r evaluated from the observed *d* spacings are respectively, 16.46Å and 33.57Å. The intercolumnar repeating

distance is slightly reduced in this case when compared to that at higher temperatures indicating tighter packing of columns.

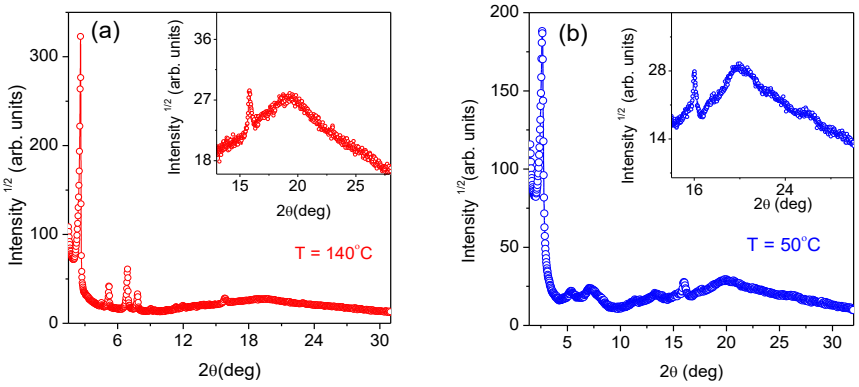

Fig. 5.20: PXRD profile of **Ni-16cpd** at (a) 140°C and at (b) 50°C.

PXRD pattern of **Ni-16bpd**, at 141°C, consisted of a number of Bragg diffractions in the low-angle region; an intense (010) reflection accompanied by relatively less intense ones, indexed to (100), (110), (120), (030), (130) and (210) reflections (**Fig. 5.21**). The anharmonicity of small angle reflections indicates the absence of any simple layer structure but a long-range two-dimensional ordered arrangement of the molecules within the mesophase. Profile fitting of the data, in this case too, matched well to a columnar rectangular organization (Col_r). Since the reflections do not abide by specific symmetry rules, it is presumed that the columns are packed in accord with a *p2mm* symmetry.[31] Lattice constants a_r and b_r are found out to be respectively, 20.28Å and 35.08Å (**Table 5.10**). In the wide-angle region, two diffuse halos were observed, first one at 4.6Å is diagnostic of the liquid-like order of the molten chains, while the relatively less diffuse one at 3.5 Å corresponds to the stacking of molecules in the columns, although this was correlated over a very short distance. If a density value of 1g/cm^3 is assumed, the number of molecules organized in each stratum of a column of height 3.5Å is found out to be 1.5. The semi-discoid molecules, thus, arrange in an antiparallel disposition with greater interdigitation of alkyl chains for efficient space filling (**Fig. 5.22a**).[38] The radius of the fully extended molecule is comparable to the intercolumnar repeating distance, thereby supporting the proposed arrangement.

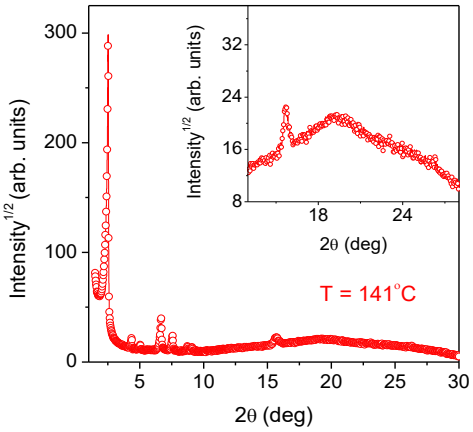

Fig. 5.21: PXRD pattern for **Ni-16bpd** at 141°C.

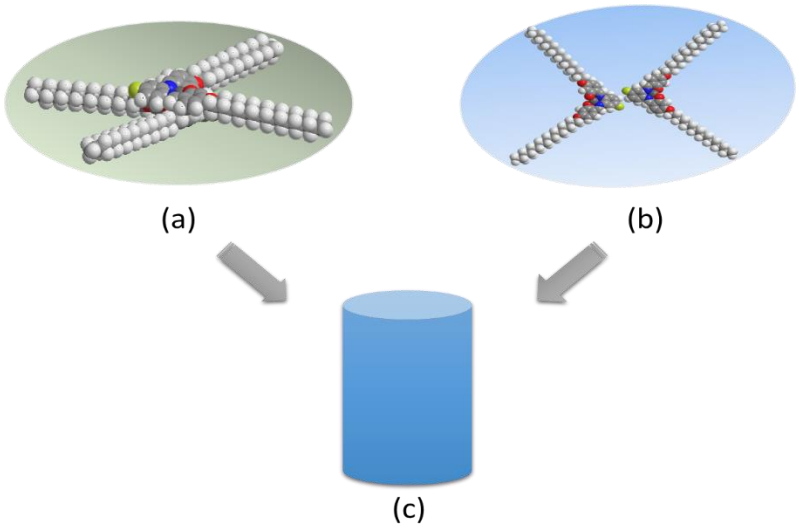

Fig. 5.22: Top-view of cross-section of a disc formed by (a) antiparallel interdigitated stacking of molecules, (b) face to face stacking of molecules and (c) packing of the semi-discoid molecules within the columns in the mesophase.

Previously reported Ni(II) complexes without any substituent, an electron donating methyl group (-CH_3) or an electron withdrawing nitro group (-NO_2) at the spacer exhibited monotropic/enantiotropic phase transition showing exclusively rectangular columnar mesophases (Col_r) with *c2mm* symmetry.[16] Monotropic mesomorphism was encountered for nitro and methyl substituted complexes whereas, the unsubstituted one showed enantiotropic mesomorphic behaviour.

Table 5.10: PXRD data of Ni (II) complexes.

Compounds	Temperature	$d_{meas.}$/Å[a]	$d_{calc.}$/Å[b]	Miller indices(hkl)[c]	Mesophase parameters[d]
Ni-16fpd	110 °C	33.89	33.89	010	Col_r, *p2mm*
		19.55	19.55	100	a_r = 19.55 Å
		16.94	16.94	110	b_r = 33.89 Å
		12.79	12.80	120	S_r = 662.55 Å^2
		11.28	11.30	030	
		4.49	–	–	
	80 °C	52.39	52.39	100	Col_o, *p1*
		33.60	33.60	110	a_o = 52.75 Å
		19.34	19.34	120	b_o = 40.00 Å
		16.89	16.80	220	γ = 83.28°
		15.04	15.00	-220	S_o = 2095.50 Å^2
		12.68	12.50	-130	S_{col} = 1047.75 Å^2
		11.18	11.20	330	
		9.59	9.55	-140	
		5.44	5.44	470	
		4.52	4.52	-670	
		4.40	–	–	
Ni-16cpd	140 °C	33.95	33.95	010	Col_r, *p2mm*
		19.57	19.57	100	a_r = 19.57 Å
		16.98	16.98	020	b_r = 33.95 Å
		12.82	12.82	120	S_r = 664.40 Å^2
		11.30	11.32	030	
		9.78	9.79	200	
		7.77	7.79	140	
		7.39	7.40	230	
		5.59	5.58	250	
		4.62	–	–	
	50°C	33.57	33.57	010	Col_r, *p2mm*
		16.46	16.46	100	a_r = 16.46 Å
		12.11	11.75	120	b_r = 33.57 Å
		7.67	7.48	140	S_r = 552.56 Å^2
		6.71	6.71	050	
		5.53	5.49	300	
		5.36	5.42	310	
		4.38	–	–	
Ni-16bpd	141 °C	35.08	35.08	010	Col_r, *p2mm*
		20.28	20.28	100	a_r = 20.28 Å
		17.56	17.56	110	b_r = 35.08 Å
		13.26	13.27	120	S_r = 711.42 Å^2
		11.69	11.69	030	V_{cell} = 2489.98 Å^3
		10.12	10.13	130	V_{mol} = 1665.68 Å^3
		9.73	9.74	210	h = 3.5 Å
		5.65	5.85	330	N_{cell} = 1.5
		4.62	–	–	
		3.53	–	–	

[a]$d_{meas.}$ and [b]$d_{calc.}$ are the experimentally measured and calculated diffraction spacings. [c] [*hkl*] are the Miller indices of the reflections. [d] Phase parameters, Col_o phase: $1/d_{hk} = 1/sin\gamma \sqrt{\{(h/a_o)^2 + (k/b_o)^2 - (2hk\ cos\gamma/a_o b_o)\}}$, γ is columnar tilt

angle; lattice area, $S_o = a_o b_o sin\gamma$; columnar cross-section, $S_{col} = a_o b_o/2$; Col_r phase: $a_r = d_{10}$; $1/d_{hk} = \sqrt{\{(h/a_r)^2 + (k/b_r)^2\}}$; columnar cross-section in the rectangular cell, $S_r = a_r b_r$. V_{cell}, volume of an elementary cell: Col_o phase, $V_{cell} = a_o b_o sin\gamma \times h$; Col_r phase, $V_{cell} = a_r b_r \times h$, where h is intra-columnar repeating distance. V_{mol}, molecular volume is determined considering a density of $1 gcm^{-3}$ according to the relationship $MW/\lambda\rho N_A$, where MW is the molecular weight, N_A is the Avogadro's number and $\lambda(T)$ is a temperature correction coefficient at the temperature of the experiment (T), $\lambda(T) = V_{CH2}(T^o) / V_{CH2}(T)$; where $V_{CH2}(T) = 26.5616 + 0.02023T$ is the volume of a methylene group (in $Å^3$) at a given temperature (in °C), and T° = 25°C. N_{cell}, number of molecules per unit cell.

5.3.3.3. Photophysical properties

The absorption and emission spectra of the Ni(II)-salphen complexes were recorded in dichloromethane solution (10^{-5} M). As a representative example, **Fig. 5.23** shows the photophysical characterization of the complexes **Ni-16fpd**, **Ni-16cpd**, and **Ni-16bpd**, respectively. All results are collected in **Table 5.11**.

Absorption spectra of the Ni(II) complexes consisted of three bands (**Fig. 5.23**). The first two at 313–316nm and at 386–391nm respectively, correspond to characteristic intraligand π–π* electronic transitions and were red-shifted with respect to the free ligands. The higher wavelength feature at 458–464nm is believed to be of charge-transfer character. This is ascribed to the excitation of filled d-orbital electrons into the empty antibonding π orbitals (d→π*) of the salphen ligand.[41,42] In the emission spectra, a single weak broad unstructured band was observed, which was located at ca. 458-460nm, in case of **Ni-16cpd** and **Ni-16bpd** while at 432nm in the case of **Ni-16fpd** due to metal-perturbed ligand centred transitions. The emission intensity is quenched in the complexes and decreases in the order: **Ni-16bpd** > **Ni-16cpd** > **Ni-16fpd**. The greater ligand-field strength of the fluoro-substituted ligands leads to maximum splitting of complex's HOMO and LUMO in fluorinated complexes compared to the rest. Thus, fractions of molecules getting excited to LUMO is reduced, explaining the reduced intensity in the case of **Ni-16fpd**. The emission quantum yields of all compounds were relatively low when compared to structurally related systems with unsubstituted, methyl or nitro-substituted aromatic spacers,[16] and was found in the range 2–5%. Taking cognizance of these facts, it is imperative to conclude that the increasing number of carbon atoms in the side alkyl chains do not affect the absorption or emission properties.

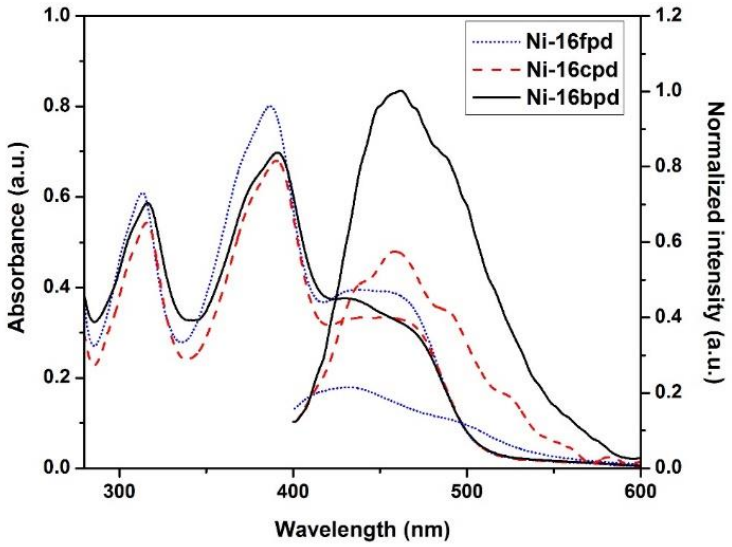

Fig. 5.23: Absorption (left) and photoluminescence (right) spectra ($\lambda_{exc.}$ = 390nm) of the Ni(II) complexes in dichloromethane solution (1×10^{-5} M, r.t.).

Table 5.11: The absorption and photoluminescence data of the Ni(II) complexes in dichloromethane solution(10^{-5}M) at 298 K.

Compounds	λ_{abs}^{max} **[nm]**$(\varepsilon/10^4)$ **[$M^{-1}cm^{-1}$]**	λ_{em}^{max} **[nm]**
Ni-12fpd	313(6.0), 386(7.9), 458(4.0)	432
Ni-14fpd	314(5.7), 386(7.3), 458(3.7)	432
Ni-16fpd	313(5.9), 386(7.7), 458(3.9)	432
Ni-12cpd	315(5.3), 390(6.3), 462(3.1)	458
Ni-14cpd	315(5.4), 390(6.9), 462(3.4)	458
Ni-16cpd	315(5.4), 390(6.8), 462(3.4)	458
Ni-12bpd	316(5.6), 391(6.7), 464(3.2)	460
Ni-14bpd	316(5.9), 391(7.0), 464(3.5)	460
Ni-16bpd	316(5.8), 391(7.0), 464(3.4)	460

5.3.4. Cu(II) complexes of mono-substituted salphen ligands; Cu-nXpd (X = f, c, b)

5.3.4.1. Synthesis and structural assessment

Mononuclear Cu(II) complexes (**Cu-nfpd**, **Cu-ncpd**, and **Cu-nbpd**) were accessed from the reaction of the appropriate ligand with copper acetate, $Cu(OAc)_2.2H_2O$ in 1:1 molar ratio as detailed in **Scheme 5.2**. The complexes were isolated as brown solids in good yields. The complexes were characterized by elemental analyses, FT-IR, and UV-visible spectroscopy. The weak broad band due to a hydrogen bonded -OH group, observed for the free ligands in the region 3400-3437cm^{-1}, was absent in all the complexes lending credence to the phenolate coordination. Further, the C=N stretching vibration was also shifted to lower wave numbers as compared to the free ligands ($\Delta \approx$ 9-18 cm^{-1}), indicating azomethine nitrogen coordination to the metal. Absorption spectra of Cu(II) complexes consisted of three distinct bands at ~326nm, ~352nm and ~403nm, respectively, accompanied by a weak shoulder at ~427nm (**Fig. 5.24** and **Table 5.12**). All of these are metal perturbed ligand centered π–π^* transitions, bathochromically shifted from those observed for the free ligands, with the longer wavelength features acquiring considerable charge transfer character. The absorption features were independent of the number of carbon atoms in the flexible alkyl chains.

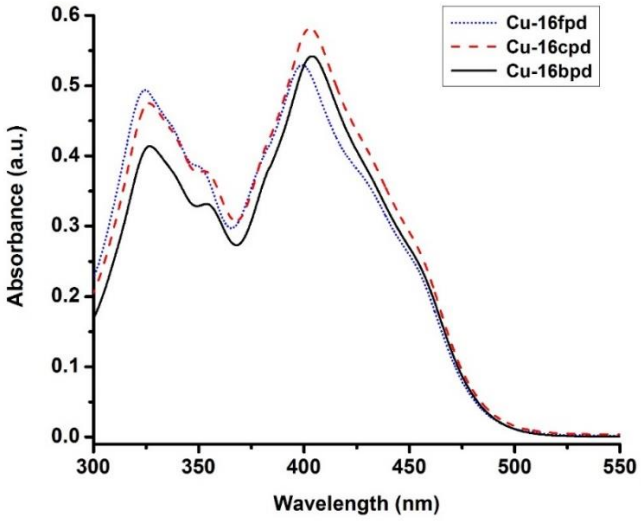

Fig. 5.24: Absorption spectra of Cu(II) complexes in dichloromethane solution (1×10^{-5}M, r.t.).

Table 5.12: Absorption data of Cu(II) complexes in dichloromethane solution (10^{-5}M) at 298K.

Compounds	λ_{abs}^{max} [nm] ($\varepsilon/10^4$) [$M^{-1}cm^{-1}$]
Cu-12fpd	325(4.8), 351(3.8) 400(5.1), 426^{sh}(3.6)
Cu-14fpd	325(4.7), 351(3.5) 400(4.9), 426^{sh}(3.6)
Cu-16fpd	325(4.9), 351(3.8) 400(5.2), 426^{sh}(3.7)
Cu-12cpd	326(4.8), 352(3.6) 403(4.9), 428^{sh}(3.5)
Cu-14cpd	326(5.0), 352(3.9) 402(5.9), 428^{sh}(3.9)
Cu-16cpd	326(4.9), 352(3.8) 403(5.8), 428^{sh}(4.3)
Cu-12bpd	327(4.2), 354(3.5) 404(5.5), 427^{sh}(4.0)
Cu-14bpd	327(4.3), 354(3.6) 404(5.6), 427^{sh}(4.1)
Cu-16bpd	327(4.1), 354(3.3) 404(5.4), 427^{sh}(3.9)

sh: shoulder

5.3.4.2. Liquid crystalline properties

Thermal property of the Cu(II) complexes was probed by polarizing optical microscopy (POM). The copper complexes all decomposed prior to melting. This unusual thermal behaviour is ascribed to a tetrahedral distortion away from the square planar geometry usually encountered in these complexes. Axial interaction is believed to be very crucial for the stability of mesophase in square planar Cu(II) complexes.[14] The metal center is coordinatively unsaturated in the square planar geometry and usually favours interaction with neighboring molecules along the axial direction. This additional interaction leads to the formation of a one-dimensional array of molecules.[14] Deviation from planarity, in some cases, prevent this axial interaction involving oxygen atoms of neighboring mesogens, thereby, frustrating mesomorphism.[14,43] In the case of presently studied mono-substituted Cu(II)-salphen complexes, the electron withdrawing halogen substituent at the phenylene spacer is believed to be disturbing the axial interaction and hence causing decomposition. Similar observation has been recorded earlier in Cu(II)-salphen complexes bearing nitro-substituted phenylene spacer.[13] In contrast to this, Cu(II) complexes of ligands with unsubstituted or methyl substituted aromatic spacer are all mesomorphic displaying rectangular plastic columnar(Col_{rp}) phase and rectangular columnar (Col_r) phase, respectively.[13]

Table 5.13: Thermal data of Cu(II) complexes.

Compounds	Decomposition temperature(°C)
Cu-12fpd	100
Cu-14fpd	95
Cu-16fpd	93
Cu-12cpd	107
Cu-14cpd	103
Cu-16cpd	98
Cu-12bpd	118
Cu-14bpd	114
Cu-16bpd	109

5.3.5. Zn(II) complexes of mono-substituted salphen ligands; Zn-nXpd (X = f, c, b)

5.3.5.1. Synthesis and structural assessment

Mononuclear Zn(II) complexes of respective salphen ligands **nfpd**, **ncpd** or **nbpd** (n = 12, 14, 16 and 18 is the number of carbon atoms in alkyl chains) were accessed using Zn(II) acetate; $Zn(OAc)_2.2H_2O$ in a single step procedure as detailed in **Scheme 5.2**. The structure of the compounds was ascertained by elemental analyses, UV-visible, FT-IR, ^1H NMR and ^{13}C NMR (for **Zn-16cpd** only) spectroscopy. FT-IR spectra of the Zn(II) complexes showed shifts of the $\nu_{C=N}$ vibrations to lower wave numbers with respect to the free ligands and absence of the ν_{O-H} vibrations, suggesting the coordination of the imine nitrogen and phenolate oxygen to the zinc(II) center. The ^1H NMR spectra of the Zn(II) complexes lacked signal for the phenolic –OH protons (**Fig. 5.25**). However, an upfield shift (~0.30ppm) in the peak position of the –N=CH protons with respect to the free ligands was observed further validating azomethine nitrogen coordination in the complexes.

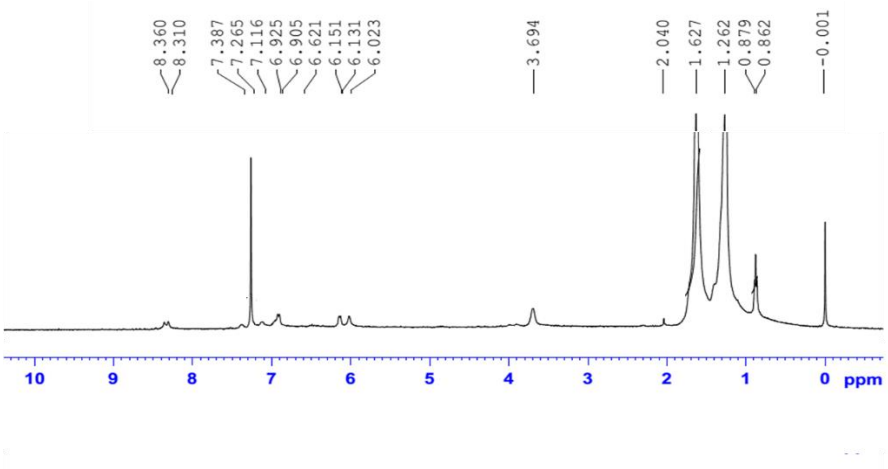

Fig. 5.25: ^{1}H NMR spectrum of a representative Zn(II) complex (**Zn-16fpd**).

5.3.5.2. Liquid crystalline properties

Polarizing optical microscopy and differential scanning calorimetry:

The Zn(II) complexes exhibited enantiotropic mesomorphism, displaying optical textures observed generally for columnar phases. Optical textures consisted of fan-like defects or broken pseudo focal-conics with linear birefringent defects, reminiscent of columnar phases (**Fig. 5.26a-c**).[32] DSC thermogram of **Zn-16fpd** consisted of two peaks in the heating cycle corresponding to solid-mesophase and mesophase-isotropic liquid transitions and only one peak in the cooling cycle corresponding to isotropic liquid-mesophase transition (**Fig. 5.27a** and **Table 5.14**). In the DSC study, **Zn-16cpd** exhibited three transitions (**Table 5.14**); two in the heating cycle corresponding to solid-mesophase and mesophase-isotropic liquid transitions and one in the cooling cycle due to isotropic liquid-mesophase transition (**Fig. 5.27b**). For both the complexes, the mesophase-solid transition was not detected in the cooling cycle of the DSC, probably due to the slower transition to more organized phases, and partial or complete vitrification of compounds upon cooling.[44] The DSC trace of **Zn-16bpd** (**Fig. 5.27c**) consisted of three peaks in the heating cycle corresponding to solid-solid, solid-mesophase and mesophase-isotropic melt transitions. The cooling cycle consisted of only two peaks due to isotropic melt-mesophase and mesophase-solid transitions. So far, clearing or isotropic melt-mesophase transition

temperatures are concerned; no trend could be noted as a function of spacer substituent in the complexes as opposed to those of the ligands, though the extreme of both the temperatures was noted for **Zn-nbpd** complexes. Further, a pronounced hysteresis in the phase transition temperature was observed in all the cases due to the viscous nature of the compounds which tend to affect the molecular mobility upon cooling. A gradual decrease in the clearing temperature was also noticed on extending the pendant alkoxy arms. The isotropic liquid to mesophase transition temperature also displayed similar trends with increasing length of the side arms.

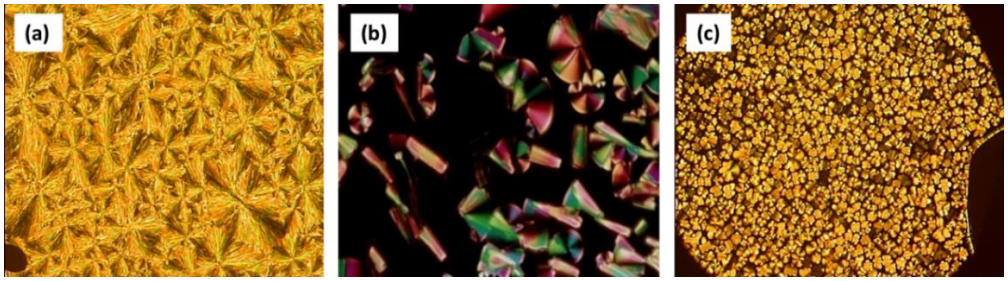

Fig. 5.26: Polarizing optical micrographs of (a) **Zn-16fpd** at 208°C, (b) **Zn-16cpd** at 189°C and (c) **Zn-16bpd** at 212°C.

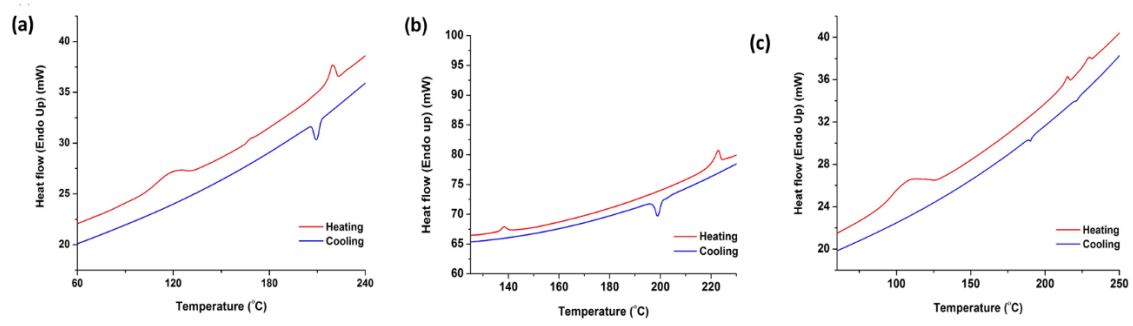

Fig. 5.27: DSC profiles of (a) **Zn-16fpd**, (b) **Zn-16cpd** and (c) **Zn-16bpd**.

Table 5.14: Thermodynamic data for the Zn(II) complexes. Transition temperatures are given in °C, and the corresponding enthalpy changes are in parentheses (ΔH; kJ mol^{-1}).

Compounds	Heating cycle[a]	Cooling cycle[a]
Zn-12fpd	Cr 126 (62.2) Col_r 234 (20.4) I	I 222 (19.2) Col_r
Zn-14fpd	Cr 123 (59.3) Col_r 228 (18.7) I	I 213 (16.5) Col_r
Zn-16fpd	Cr 121 (28.4) Col_r 222 (14.2) I	I 204 (12.8) Col_r
Zn-12cpd	Cr 138 (4.1) Col_r 222 (9.2) I	I 200 (9.1) Col_r
Zn-14cpd	Cr 131 (4.3) Col_r 218 (8.8) I	I 198 (8.9) Col_r
Zn-16cpd	Cr 129 (4.7) Col_r 214 (9.6) I	I 189 (9.9) Col_r
Zn-18cpd	Cr 126.1 (4.8) Col_r 210.2 (8.9) I	I 185.5 (8.8) Col_r
Zn-12bpd	Cr 128 (38.1) Cr_1–Col_r 242 (13.0) I	-
Zn-14bpd	Cr 110 (28.1) Cr_1–Col_r 238 (15.7) I	I 232 (3.8) Col_r 216 (2.1) Cr_1
Zn-16bpd	Cr 108 (50.1) Cr_1 215 (3.5) Col_r 232 (2.6) I	I 222 (2.2) Col_r 190 (2.6) Cr_1

[a]DSC peak temperature, Cr, Cr_1 refer to phases that are crystalline or solid; Col_r: rectangular columnar phase.

Variable temperature PXRD study:

Final phase assignments of all the Zn(II) complexes was made by variable temperature powder X-ray diffraction measurements. A representative from each series of complexes (**Zn-16fpd**, **Zn-16cpd**, and **Zn-16bpd**) was chosen for the study.

The diffractogram of **Zn-16fpd** at 220 °C (**Fig. 5.28a**) consisted of a series of several Bragg diffraction peaks in the low angle region resembling a 2-D primitive orthorhombic lattice.[29] These features could be indexed well to a rectangular columnar phase (Col_r) (**Table 5.15**). The presence of higher order reflections suggests that the mesophase is ordered. Additionally, two broad scattering halos (visualized by profile fitting of the data) were observed in the wide-angle region. The broad maxima centered at around 4.7 Å is due to the liquid-like correlation of molten aliphatic chains, and a characteristic less broad one at 3.6 Å corresponds to the lateral short-range order of the molecular cores within the same column (core–core separation). A third halo though relatively weak was also observed at still wider angles due to intracolumnar stacking. This suggests the correlation between the

cores is significantly enhanced in the complexes due to axial interactions. The presence of (110), (220), (130), (310), (320) and (040) reflections at small angles with hk: no conditions, h0: h = 2n, 0k: k = 2n, suggested orientation of elliptical columns along two different directions (herringbone packing of elliptical columns, *p2gg*).[29] The lattice parameters a_r and b_r calculated from the observed *d* spacings are found to be 43.0 Å and 45.5 Å. Considering a stacking distance of 3.6 Å (as obtained from X-ray) and assuming a density of 1g/cm^3 for the semi-discoid molecules, number of molecules per unit cell of the lattice, N_{cell} is calculated to be equal to four. In a *p2gg* plane group, there are two columns per unit lattice, so, the columnar cross-section, in this case, is composed of two molecules arranged in a back-to-back fashion to cover the surface area of the lattice. Also, the lattice constant is twice the radius of a single molecule in its extended conformation as inferred from DFT study (*vide-infra*), supporting the proposed molecular organization (**Fig. 5.28b**).[38]

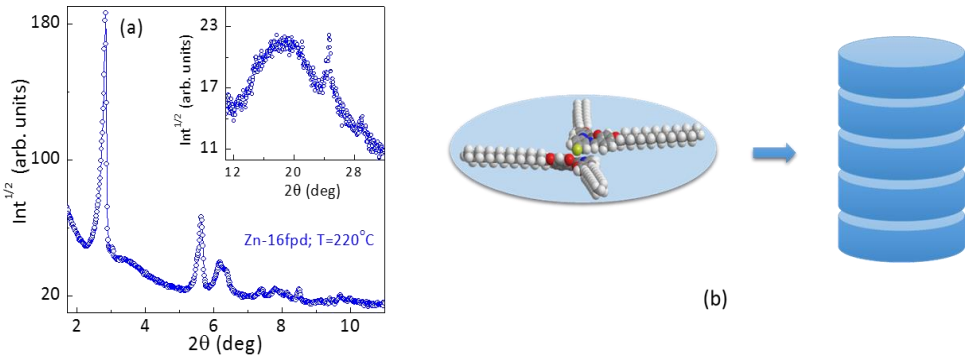

Fig. 5.28: (a) One-dimensional intensity vs. 2θ profile of **Zn-16fpd** at 220°C and (b) model for molecular organization in the mesophase.

In the diffraction pattern of **Zn-16cpd**, at 194°C, three sharp diffraction peaks at 15.1Å, 13.01Å, and 10.06Å were observed in the small angle region (**Fig. 5.29a** and **Table 5.15**). The first two fundamental reflections were indexed as the (110) and (200) reflections of a rectangular lattice.[29] Moreover, due to the presence of (210) peak, the symmetry of the lattice can be further assigned to a *p2gg* plane group.[29] In the wide angle region, a broad diffuse peak (4.9Å) was observed which confirms the liquid-like order of the molten chains. The relatively sharper peak at about 3.5 Å, well separated from the broad one can

be attributed to the stacking distance of the discs within the same column (core–core separation). A less intense peak at ca. 7.8 Å possibly indicate a perpendicular stacking of the hemi-disc-shaped molecules which is necessary to produce a disc-shaped dimer for the formation of the columnar phase. A molecular organization based on a dimeric interaction involving Zn and phenolate-O has been invoked to explain the 'disc' like formation (**Fig. 5.29b**).

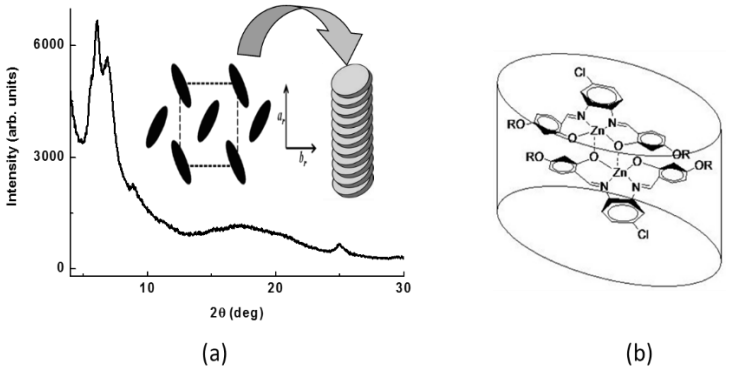

Fig. 5.29: (a) One-dimensional intensity vs. 2θ profile **Zn-16cpd** at 194°C and (b) dimeric association of the molecules in the mesophase.

For **Zn-16bpd**, the PXRD pattern at 230°C (**Fig. 5.30a**), consisted of a large number of peaks in the small angle region which fitted well to a 2-D rectangular columnar phase.[31,32] Application of the extinction rules, to the estimated indexation, agrees well with a *p2mg* plane group (for *p2mg;* hk: no condition, h0: no condition, 0k: k = 2n).[31,32] The lattice constants, a_r and b_r are calculated to be 30.6 Å and 37.7 Å (**Table 5.15**). The wide angle region consisted of two broad maxima, first one at 4.8 Å corresponds to the liquid-like correlations of molten alkyl arms and a second, relatively less broad one at slightly wider angles (3.6 Å), corresponds to the stacking periodicity of molecules within the column. In this case too, a third maximum due to intra-discoidal stacking is observed at slightly wider angles. Assuming a density of 1g/cm^3 typical for such half-discoid molecules,[19] it is found that the unit cell in the *p2mg* lattice is composed of two molecules. The intercolumnar repeating distance is slightly more than the computed radius of the molecule (~21 Å). Consequently, it is presumed that the half-disc molecules would stack in an anti-parallel interdigitated manner for more efficient space-filling (**Fig. 5.30b**).

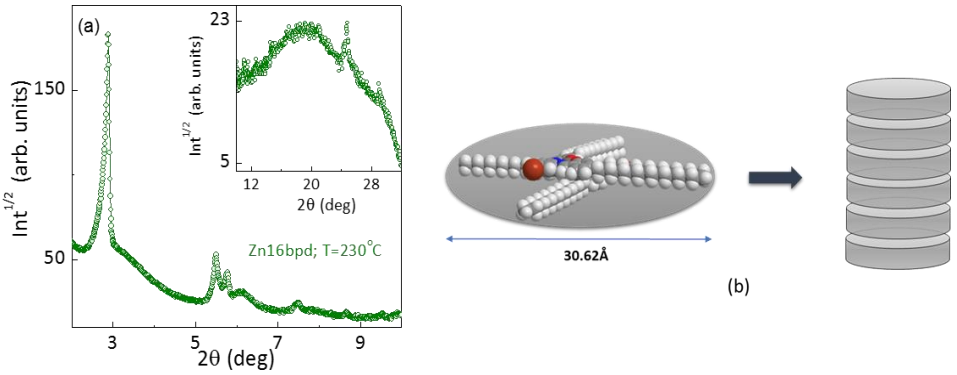

Fig. 5.30: (a) One-dimensional intensity vs. 2θ profile of **Zn-16bpd** at 230°C and (b) model for molecular organization in the mesophase.

A critical comparison among the different mono-halogenated Zn(II) complexes, suggests no trend in the melting and clearing temperatures as a function of a substituent when compared to that of the ligands. The overall lattice packing is, however, greatly influenced by the nature and size of the spacer substituent in the case of the Zn(II) complexes. While the fluoro- and chloro-substituted Zn(II) complexes being discussed herein exhibited columnar rectangular columnar phase with a *p2gg* symmetry, the bromo-substituted complexes displayed rectangular columnar phase with a *p2mg* symmetry. Further, all the halogenated Zn(II) complexes studied in the present work exhibited enantiotropic mesomorphism with a high thermal stability. But those previously reported without any substituent or with a methyl group at the aromatic spacer displayed monotropic columnar mesomorphism.[20,21] Mesophases exhibited by these complexes were either hexagonal or rectangular/oblique (P_{222}/P_{112}) columnar type.[20,21] Electron withdrawing nature of the halogen substituent (-F, -Cl, -Br) leads to enhanced dipolar interactions favouring better core-core correlations and improved thermal stability of the halogenated complexes over both unsubstituted as well as the methyl substituted ones. Apart from that, a significant increase in the magnitude of the lattice constant is noticed for the fluorinated complex compared to the Cl- or Br- substituted analogs. The size of the halogen moiety (covalent radius of F = 0.072nm; Cl = 0.099nm; Br = 0.114nm) and the associated electronic and steric properties may thus be responsible for the observed thermal properties of the Zn(II) complexes and their difference from the structurally related ones.

Table 5.15: X-ray diffraction data of the Zn(II) complexes.

Compounds	Temperature	$d_{meas.}$/Å[a]	$d_{calc.}$/Å[b]	Miller indices(hkl)[c]	Mesophase parameters[d]
Zn-16fpd	220 °C	31.2	31.2	110	Col_r, *p2gg*
		15.7	15.6	220	a_r = 43.0 Å
		14.3	14.3	130	b_r = 45.5 Å
		13.9	13.7	310	S_r = 1956.5 Å^2
		12.0	12.1	310	S_{col} = 978.2 Å^2
		11.2	11.4	320	h = 3.6 Å
		10.4	10.4	040	V_{cell} = 7043.4 Å^3
		4.7(diffuse)	–	–	V_{mol} = 1639.1 Å^3
		3.6(core-core)	–	–	
		3.1	–	–	
Zn-16cpd	194 °C	15.13	15.12	110	Col_r, *p2gg*
		13.01	13.03	200	a_r = 26.04 Å
		10.06	10.04	210	b_r = 18.63 Å
		7.8	–	–	S_r = 484.36 Å^2
		4.9(diffuse)	–	–	S_{col} = 242.18 Å^2
		3.5(core-core)	–	–	V_{mol} = 1774.13 Å^3
					h = 3.5 Å
Zn-16bpd	230 °C	30.6	30.6	100	Col_r, *p2mg*
		16.1	16.1	120	a_r = 30.6 Å
		15.3	15.3	200	b_r = 37.7 Å
		14.4	14.2	210	S_r = 1154.4 Å^2
		11.8	11.9	220	h = 3.6 Å
		11.2	11.6	130	V_{cell} = 4155.7 Å^3
		10.2	10.2	300	V_{mol} = 1752.7 Å^3
		9.3	9.4	040	
		8.9	8.9	320	
		7.9	8.0	240	
		7.6	7.6	400	
		6.9	6.9	340	
		6.1	6.1	350	
		6.0	6.0	510	
		4.7(diffuse)	–	–	
		3.6(core-core)	–	–	
		3.1	–	–	

[a]$d_{meas.}$ and [b]$d_{calc.}$ are the experimentally measured and calculated diffraction spacings. The distances are given in Å. [c] [*hkl*] are the Miller indices of the reflections. [d] Phase parameters, Col_r phase: $1/d_{hk} = \sqrt{[(h/a_r)^2 + (k/b_r)^2]}$; lattice area, $S_r = a_r b_r$; columnar cross-section, $S_{col} = S_r/2$ (for *p2mm* lattice, $S_{col} = S_r$). V_{cell}, volume of an elementary cell: Col_r phase, $V_{cell} = a_r b_r \times h$, where h is intra-columnar repeating distance. V_{mol}, molecular volume is determined considering a density of 1gcm^{-3} according to the relationship $MW/\lambda\rho N_A$, where MW is the molecular weight, N_A is the Avogadro's number and $\lambda(T)$ is a temperature correction coefficient at the temperature of the experiment (T), $\lambda(T) = V_{CH2}(T^o) / V_{CH2}(T)$; where $V_{CH2}(T) = 26.5616 + 0.02023T$ is the volume of a methylene group (in Å^3) at a given temperature (in °C), and T° = 25°C. N_{cell}, number of molecules per unit cell and N_{col}, number of molecules per columnar cross-section.

5.3.5.3. Photophysical properties

Absorption spectra of Zn(II) complexes consisted of two overlapped bands at ~320nm and between 373–385nm and a shoulder at longer wavelengths, corresponding to metal perturbed ligand centered π-π* transitions of the aromatic rings and the imine unit (**Fig. 5.31 and Table 5.16**).

The emission maxima of the Zn(II) complexes in dichloromethane solution was positioned at around 500nm for **Zn-16fpd** and 508nm for **Zn-16cpd** and **Zn-16bpd ,** respectively, in the blue-green region of the visible spectrum (**Fig. 5.31 and Table 5.16**). The observed fluorescence emission in the complexes originates from metal-perturbed π–π* ligand-centered transitions and the red shift of the emission feature is most likely due to the increased rigidity of the complex molecules when compared to the free ligands.[45] The ligand field strength of the halogenated ligands decreases in the order F > Cl > Br, causing maximum splitting of complex's HOMO and LUMO in the case of fluorinated complexes. This causes a decrease in the fraction of molecules getting excited to LUMO thereby explaining the reduced intensity in the case of **Zn-16fpd**. The emission quantum yield of the complexes (EQY= 7-18%) is higher than those of the free ligands (EQY= 4-10%), as the chelation of ligand to the metal center enhanced the rigidity of the ligand and reduced the loss of energy by thermal vibrational decay.

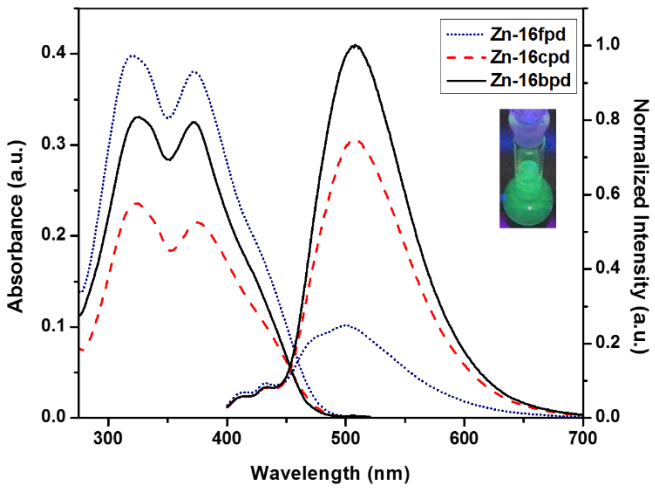

Fig. 5.31: Absorption(left) and normalized photoluminescence(right) spectra ($\lambda_{exc.}$ = 320nm) of the Zn(II) complexes in dichloromethane solution (1×10^{-5} M, r.t.).

The solid state emission spectra of the complexes were recorded on thin films. For the complexes emission maxima was located at ~ 515 nm in the solid state (**Fig. 5.32**). The emission intensity is, however, reduced in the solid state as a result of the closer association of molecular cores as compared to that in solution.[20,21]

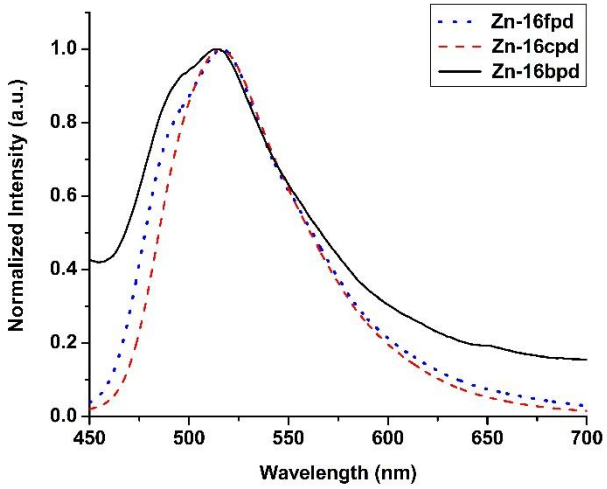

Fig. 5.32: Photoluminescence spectra of the Zn(II) complexes ($\lambda_{exc.}$ = 320nm) in the solid state.

The unusual square planar geometry around the Zn(II) center generated by the rigid ligand framework in Zn(II)-salphen complexes leaves a vacant axial coordination site resulting in high Lewis acidity of Zn^{2+} ion.[46] Bulky substituents at 3,3′- position of the salicylaldehyde fragments in these ligands are known to lead to the isolation of unique square planar complexes;[47] precluding chelation to suitable donors/Lewis bases or formation of aggregates/self-assembled structures.[1,46] In absence of any bulky substituents, pentacoordinate nature of the Zn^{II} center in these complexes facilitates aggregation through intermolecular Zn⋯O axial interaction in non-coordinating solvents and in the solid state or de-aggregation through axial coordination of coordinating solvents. Aggregation/de-aggregation phenomenon causes dramatic changes in the absorption and emission behaviour of these complexes.[1,48] Thus, solvatochromic studies were conducted on a representative complex of each halogenated series. The absorption spectra of **Zn-16fpd**, **Zn-16cpd**, and **Zn-16bpd** in dilute solution of non-coordinating solvents (DCM, toluene; 1×10^{-5}M) consisted of two overlapped bands at ~320nm and between 373–385nm and a

shoulder at longer wavelengths, in line with the existence of aggregate species in solution (**Fig. 5.33a-c**).[48] In coordinating solvent (DMSO), a red shift (~15nm) of the longer wavelength feature was noticed while the shoulder became much more prominent due to the axial coordination of the solvent molecules, suggesting the formation of 1:1 adduct (**Fig. 5.33a-c**).[48] These features are independent of any change in concentration and they remain substantially unaltered up to a concentration of 10^{-4} M (**Fig. 5.34a-c**). Photoluminescence spectra of the complexes (**Fig. 5.33a-c**) in non-coordinating solvents consisted of a broad band at ~500-508 nm (EQY = 7-19%). In coordinating solvents, the position of maxima is virtually unaltered, though an enhancement in fluorescence intensity is observed (EQY = 14-27%), suggesting de-aggregation with concomitant formation of monomeric species (Table 4).[48] Similar behaviour has been noted for analogous Zn(II)-salphen systems with varying aromatic spacers.[48] Fluorescence of face-to-face-stacked H-type dimer aggregates (sandwich-type dimers) is known to be quenched relative to that of the monomer due to a rapid energy relaxation of the lower excited states.[49]

Table 5.16: The optical absorption and photoluminescence data of the Zn(II) complexes in different solvents and in the solid state at 298 K.

Compounds	Solvents	λ_{abs}^{max} [nm] ($\varepsilon/10^4$; $M^{-1}cm^{-1}$)	λ_{em}^{max} [nm] (solution)	λ_{em}^{max} [nm] (solid)
Zn-12fpd	DCM	320(3.9), 376(3.8), 407^{sh} (2.3)	500	
Zn-14fpd	-do-	320(3.8), 376(3.7), 407^{sh} (2.4)	500	
Zn-16fpd	-do-	320(3.9), 373(3.8), 407^{sh} (2.4)	500	515
	Toluene	315(4.0), 381(4.2), 409^{sh} (2.7)	502	
	DMSO	312(4.4), 391(5.2), 418^{sh} (3.4)	499	
Zn-12cpd	DCM	324(2.9), 376(2.9), 407^{sh} (2.0)	508	
Zn-14cpd	-do-	324(2.7), 376(2.7), 407^{sh} (1.8)	508	
Zn-16cpd	-do-	323(2.8), 376(2.8), 407^{sh} (1.9)	508	515
	Toluene	321(2.8), 385(2.9), 410^{sh} (2.0)	503	
	DMSO	313(2.9), 395(3.4), 422^{sh} (2.2)	500	
Zn-18cpd	DCM	324(2.6), 376(2.7), 407^{sh} (2.0)	508	
Zn-12bpd	DCM	325(3.5), 373(3.4), 406^{sh} (2.5)	508	
Zn-14bpd	-do-	325(3.3), 374(3.3), 406^{sh} (2.3)	508	
Zn-16bpd	-do-	325(3.3), 373(3.2), 406^{sh} (2.1)	508	515
	Toluene	321(3.6), 385(3.8), 411^{sh} (2.6)	501	
	DMSO	315(3.6), 393(3.5), 421^{sh} (2.2)	500	

sh: shoulder

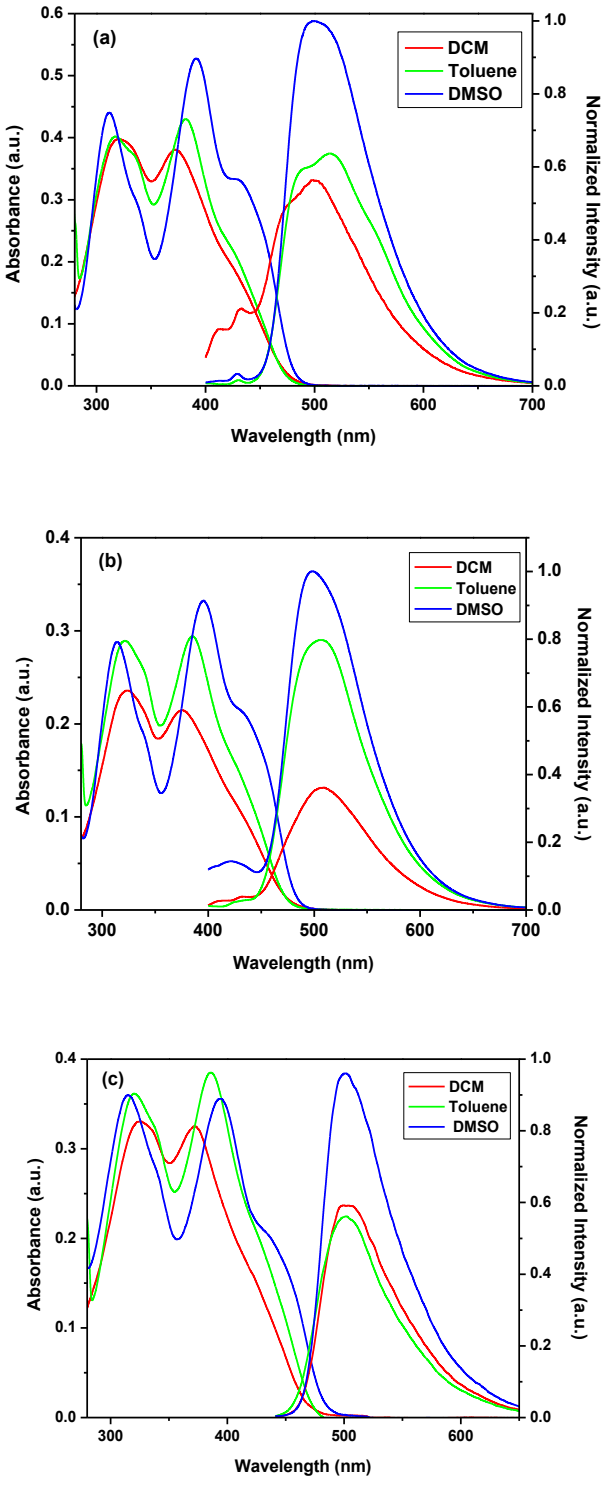

Fig. 5.33: Absorption(left) and emission(right) spectra of (a) **Zn-16fpd**, (b) **Zn-16cpd** and (c) **Zn-16bpd** in non-coordinating and coordinating solvents (1×10^{-5} M, r.t).

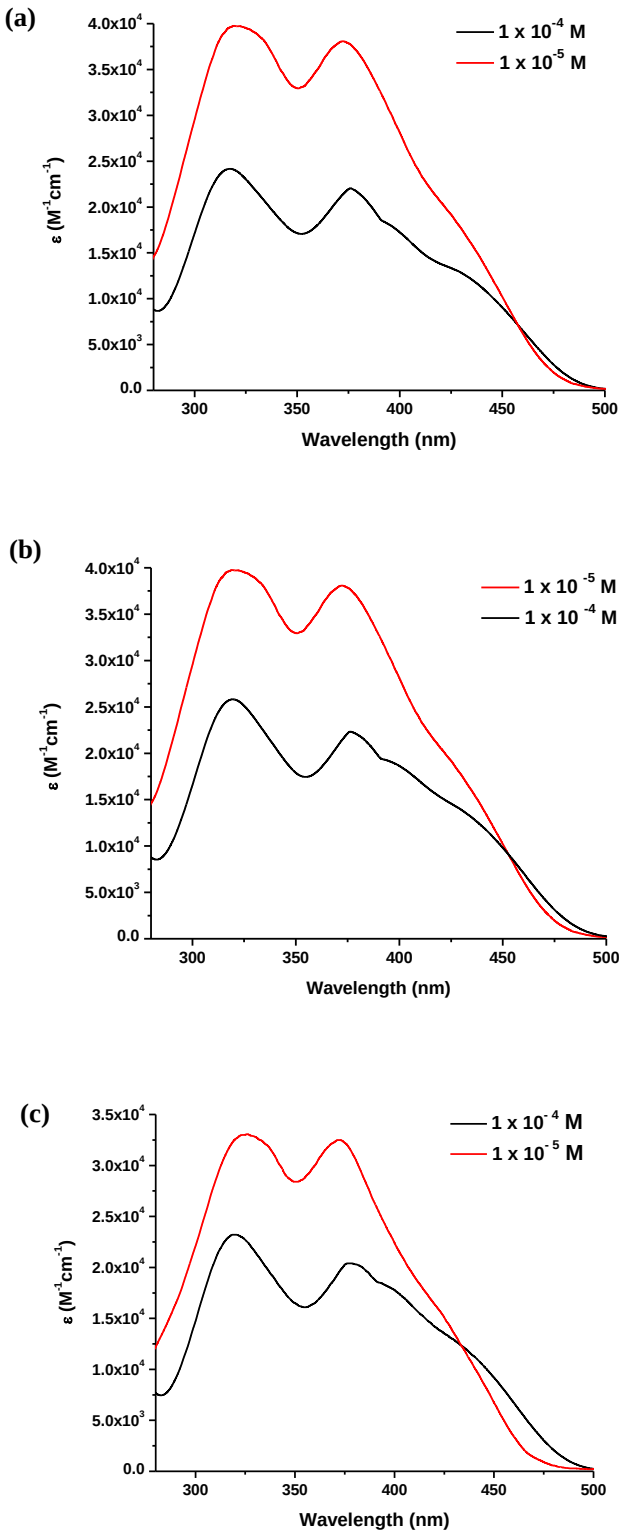

Fig. 5.34: Concentration dependence of UV-visible absorption spectra of (a) **Zn-16fpd**, (b) **Zn-16cpd** and (c) **Zn-16bpd** in dichloromethane solution.

5.3.5.4. DFT Study

In absence of diffraction quality single crystals, density functional theory (DFT) was used as a tool to arrive at the energy optimized structure of representative Zn(II)complexes, **Zn-16fpd**, **Zn-16cpd**, and **Zn-16bpd**. DFT calculations of **Zn-16fpd** and **Zn-16bpd** were carried out using GAUSSIAN 09 program package,[33] The ground state geometry optimization in the gas phase of the zinc complexes has been performed using the three-parameter fit of Becke's hybrid functional combined with the Lee-Yang-Parr correlation functional termed as B3LYP hybrid,[34,35] generalized gradient approximation(GGA) exchange along with 6-311+G(d,p), 6-31+G(d,p), 6-31G(d) and 6-31G basis sets [36] for Zn, N, and O, C and H, respectively, without imposing any symmetry constraint. For **Zn-16cpd**, calculations were performed with the DMol3 program package.[39] The basis set chosen in this case was DNP, the double numerical atomic orbitals augmented by polarization functions. Spin restricted calculation has been performed in the framework of the generalized gradient approximation (GGA). At the GGA level, the BLYP functional has been used throughout this study, comprising a hybrid exchange functional as defined by Becke and the non-local Lee–Yang–Parr correlation functional.[35] Convergence in energy, force and displacement were set as 10^{-5} Ha, 0.001 Ha/Å and 0.005 Å, respectively (**Table 5.17**). The appropriate structure of the three representative complexes (**Fig. 5.35a-c**) was confirmed as energy minima by calculating the vibrational frequency and confirming the absence of any imaginary frequencies. Based on the results a square planar geometry is suggested around the metal center in all the zinc(II) complexes (**Fig. 5.35a-c**).

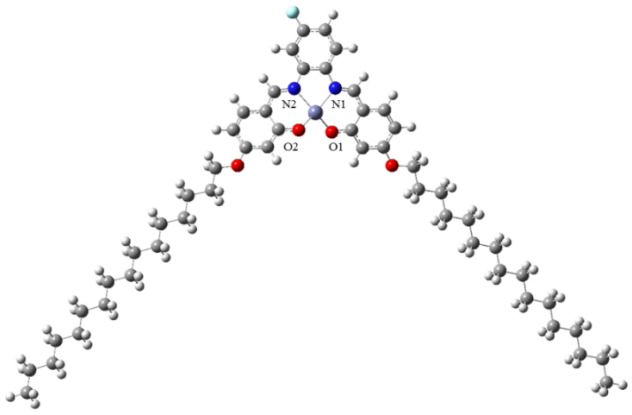

Fig. 5.35a: Optimized electronic structure of **Zn-16fpd**.

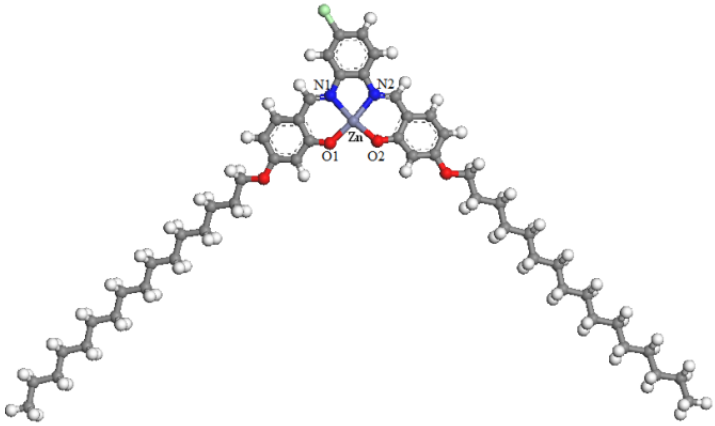

Fig. 5.35b: Optimized electronic structure of **Zn-16cpd**.

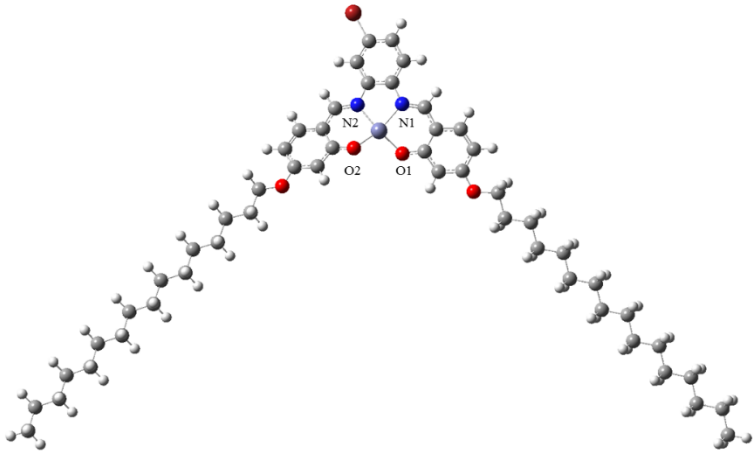

Fig. 5.35c: Optimized electronic structure of **Zn-16bpd**.

The three-dimensional (3D) iso-surface plots of the lowest unoccupied molecular orbital (LUMO) and the highest occupied molecular orbital (HOMO) of **Zn-16cpd** has also been studied and are presented in **Fig. 5.36a** and **b**. The electron density of the HOMO is localized on the aromatic rings, while the LUMO is mainly centered on N–C bonds. The HOMO and LUMO energies of the zinc complex are calculated to be −4.898 and −2.703 eV, respectively, ΔE = 2.195 eV. The HOMO–LUMO energy difference, in fact, is a measure of the kinetic stability of the molecule, indicating the reactivity pattern of the molecule.[50] The HOMO–LUMO gap (2.195 eV) in the present case implies high kinetic stability and low chemical reactivity because it is energetically unfavourable to add

electrons to a high-lying LUMO or to extract electrons from a low-lying HOMO.[51] The HOMO–LUMO energy difference evaluated from the lowest energy UV-Vis band (451 nm) is 2.75 eV, which is substantially higher than that obtained from DFT studies (ΔE = 2.195 eV). Extensive intermolecular interactions in the solution phase (UV-Vis study) *vis-á-vis* free gaseous molecule (DFT study) could be one plausible reason for such a deviation.

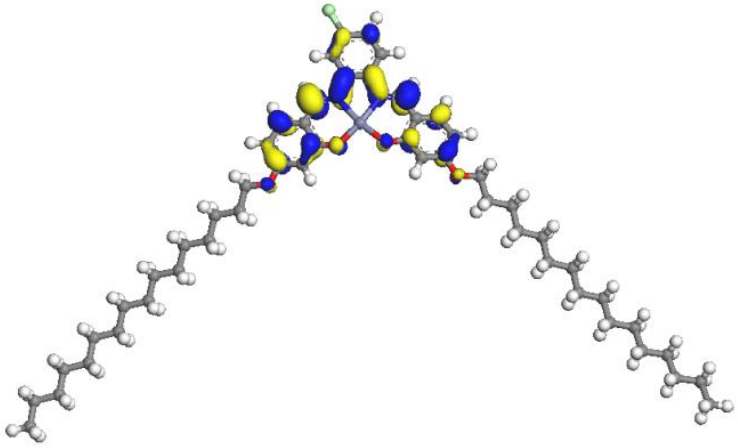

Fig. 5.36a: HOMO diagram of **Zn-16cpd**.

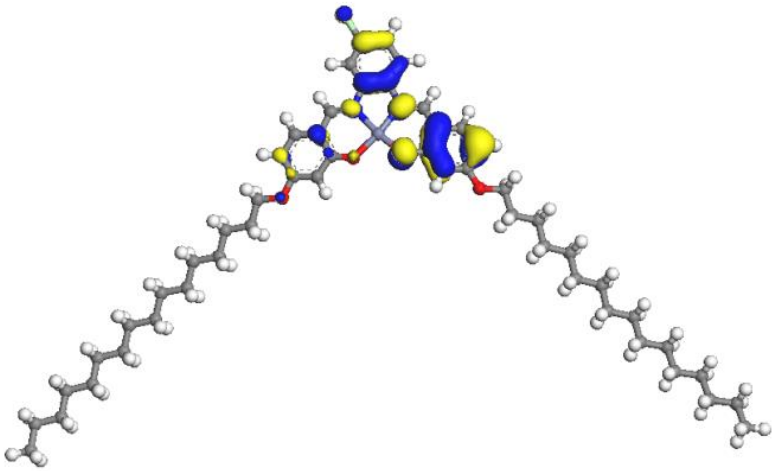

Fig. 5.36b: LUMO diagram of **Zn-16cpd**.

Table 5.17: Selected bond lengths (Å) and angles (°) and other related parameters of Zn(II) complexes evaluated at B3LYP(for **Zn-16fpd** and **Zn-16bpd**)/ BLYP (for Zn-16cpd) level.

Structural parameters	Zn-16fpd	Zn-16cpd	Zn-16bpd
Zn—O1	1.915	1.961	1.913
Zn—O2	1.906	1.966	1.908
Zn—N1	2.036	2.100	2.036
Zn—N2	2.033	2.095	2.034
O1— Zn— O2	104.6	97.2	104.5
N1 — Zn—N2	81.1	79.5	81.2
N1 — Zn—O1	91.8	91.6	92.1
N2 — Zn—O2	93.4	92.0	93.2
N1—N2 — O2—O1	-34.5	-33.9	-34.2
N1—O1 — O2—N2	31.9	31.3	31.8
Molecular Length (Å)	42.30	41.79	42.31
Dipole moment (D)	1.29	1.18	0.99

5.3.6. Comparative assessment of thermal and photophysical properties of the monosubstituted salphen ligands and corresponding metal complexes

Thus, spacer group substituent has a major influence on the thermal and photophysical properties of mono-halogen substituted salphen ligands and their corresponding metal complexes. The electronic effects coupled with the steric interactions of the substituent is key to such behaviour. Nevertheless, the role of the metal ion is also crucial, and any subtle changes in the metal's coordination geometry can cause dramatic changes in the thermal and photophysical properties as well. The salphen framework generates more or less a planar geometry and the metal ion is forced to attain either a square planar (as in the case of Ni^{2+}, Cu^{2+}, and Zn^{2+}) or a square-pyramidal conformation (in VO^{2+}), though some distortion occurs. Thus a subtle interplay of both steric and electronic factors originating from aromatic spacer and distortions in coordination geometry associated with the nature of metal ions might be responsible for the observed mesomorphic and photophysical diversity in the salphen complexes under current discussion and their deviation from those exhibited by structurally analogous metal-salphen systems.

5.3.7. Di-substituted salphen ligands and their metal complexes

5.3.7.1. Synthesis and structural assessment:

Condensation of 4-n-alkoxy substituted salicylaldehydes with 4,5-dichlorobenzene-1,2-diamine afforded the corresponding salphen ligands. Complexes were obtained by the reaction of the corresponding Schiff bases with vanadyl sulfate; $VOSO_4.H_2O$, nickel acetate; $Ni(OAc)_2.2H_2O$, copper acetate; $Cu(OAc)_2.2H_2O$ or zinc acetate; $Zn(OAc)_2.2H_2O$ in 1:1 molar ratio. The strategy implemented for the synthesis of ligands [N,N-bis-(4-n-alkoxysalicylidene)-4,5-dichloro-1,2-diaminobenzene], abbreviated as **nc2pd** (n = 12, 14 and 16 is the number of carbon atoms in alkyl chains) and the mononuclear complexes (**VO-nc2pd**, **Ni-nc2pd**, **Cu-nc2pd** or **Zn-nc2pd**) has been summarized in **Scheme 5.2**. The structure of the ligands and the corresponding complexes were ascertained by elemental analyses, UV-visible, FT-IR and ^{1}H NMR (for ligands, Ni(II) and Zn(II) complexes only) spectroscopy. IR spectra of the ligands showed bands corresponding to the $\nu_{C=N}$ and ν_{O-H} vibrations at ca. 1614cm^{-1} and 3436cm^{-1}, respectively. For corresponding metal complexes the $\nu_{C=N}$ vibrations were observed at lower wave numbers compared to the free ligands along with the absence of ν_{O-H} vibrations, suggesting coordination of the imine nitrogen and phenolate oxygen to the metal center. The VO(IV) complexes additionally showed $\nu_{V=O}$ stretching at ~ 971 cm^{-1} indicating the absence of any intermolecular (····V=O····V=O····) interaction, consistent with the monomeric nature of the complexes.[15,37] For polymeric complexes this band appears below 900cm^{-1} due to linear chain interactions, while that for monomeric ones it is located in the region 900-1000cm^{-1}.[37] The ^{1}H NMR spectra of the ligands (**nc2pd**) showed characteristic signals, at δ = 13.17ppm corresponding to the OH protons, and ~8.52ppm for the symmetric imine protons (**Fig. 5.37a**). The ^{1}H NMR spectra of the corresponding Ni(II) and Zn(II) complexes did not exhibit any signal for the phenolic –OH proton (**Fig. 5.37b** and **c**). However, an upfield shift in the peak position of –N=CH protons with respect to the free ligands was observed for complexes of both the series confirming azomethine nitrogen coordination.

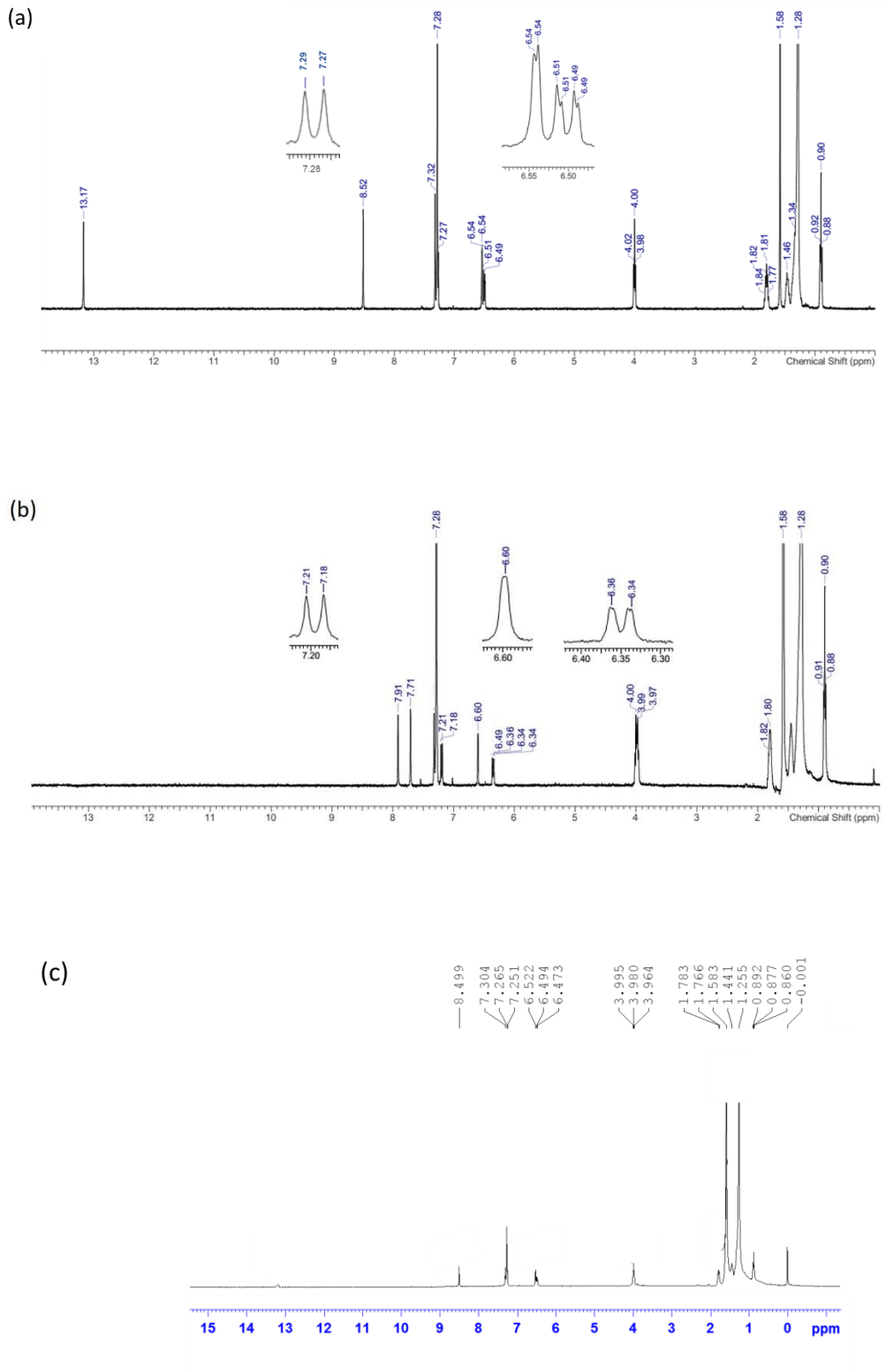

Fig. 5.37: ^{1}H NMR spectra of (a) **16c2pd**, (b) **Ni-16c2pd** and (c) **Zn-16c2pd**.

5.3.7.2. Liquid crystalline properties

Polarizing optical microscopy and differential scanning calorimetry:

The thermal behaviour of the ligands and the corresponding metal complexes were investigated by polarizing optical microscopy(POM), differential scanning calorimetry(DSC) and variable temperature powder X-ray diffraction(XRD) studies. Ligands are non-mesomorphic, melting directly to an isotropic liquid at 80-90°C. However, coordination of the salphen ligands particularly to Zn(II) and Ni(II) ions conferred liquid-crystalline properties on the resulting complexes. The Cu(II) complexes decomposed just at the onset of melting at 120°C. The VO(IV) analogs, on the contrary decomposed prior to melting at a temperature higher than 280°C preventing any mesomorphic study. This unusual thermal behaviour of the VO(IV) and Cu(II) complexes can be explained by invoking axial interaction for the stability of mesophase. Square planar copper(II)-salen or salphen complexes are coordinatively unsaturated and the metal center usually satisfies the necessity through interaction with neighboring molecules along the axial direction. This additional interaction favours the formation of an one-dimensional array of the molecules.[14] Tetrahedral distortions away from the square planar coordination, in some cases, prevent this axial interaction involving oxygen atoms of neighboring mesogens, preventing mesophase formation.[14,43] In the present salphen-Cu(II) complexes, the electron withdrawing dichloride substitution at the phenylene spacer is considered to be disturbing the axial interaction and hence resulting in decomposition of the same. Similar observation has been noted earlier in analogous Cu(II)-salphen complexes bearing nitro-substituted phenylene spacer.[13] VO(IV)-salphen complexes on the other hand adopt a square pyramidal geometry, which is non-planar and less anisotropic. The axial vanadyl oxygen is contemplated to form a weak dative bond with the vanadium of a neighboring mesogen, thus assembling the cores into an one-dimensional array, favouring mesophase formation.[14] Again, too rigid linear V=O·····V=O interactions may lead to polymeric complexes causing loss of mesomorphism.[37] Therefore, the length of the V=O bond i.e., the extent of axial interaction is very crucial to the formation of mesophases. A relatively high temperature of decomposition of the VO(IV) complexes in the present study, thus, can be accounted for by invoking (i) the presence of dichloride substituent at the phenyl

spacer might somewhat obscure the extruding oxo group, or (ii) there might be a trigonal-bipyramidal distortion in the metal coordination geometry.[14]

Ni-nc2pd and **Zn-nc2pd** complexes exhibited enantiotropic mesomorphism (**Table 5.18**). The Ni(II) complexes displayed a somewhat atypical texture (**Fig. 5.38a**) at 150 °C upon slow cooling from the isotropic melt. The Zn(II) complexes on the other hand showed a broken fan-like texture (**Fig. 5.38b**) at 160°C characteristic of columnar phases.[32] The optical texture remained unaltered till room temperature for the **Zn-nc2pd** complexes.

DSC thermogram of **Ni-16c2pd** displayed four endothermic peaks in the first heating cycle due to two crystal-crystal and one each of crystal-mesophase and mesophase-isotropic liquid transitions (**Fig. 5.39c**). In the cooling cycle, four exothermic peaks were observed corresponding to isotropic liquid-mesophase, mesophase-crystal and two crystal-crystal transitions. The endothermic peak observed at 101°C in the first heating run appeared as an exothermic peak at 98°C in the second heating run (**Fig. 5.39c**). This is believed to be initiating from a low energy crystal packing at higher temperatures.[52] The DSC trace for **Ni-12c2pd** and **Ni-14c2pd**, however, consisted of only two peaks both in the heating and the cooling cycle (**Fig. 5.39a** and **b**). DSC thermogram of **Zn-nc2pd**; n = 12, 14, 16 (**Fig. 5.40a-c**) displayed two endothermic peaks in the heating cycle corresponding to crystal-mesophase and mesophase-isotropic liquid transitions. In the cooling cycle, the isotropic liquid-mesophase transition as observed in the POM was not detected in DSC. Absence of this peak in the cooling cycle of DSC thermogram accompanied by low enthalpy value for the mesophase-isotropic liquid transition in the heating scan suggests the mesophase to be highly disordered.[53] A gradual decrease in the clearing temperature was noted on increasing the number of carbon atoms in the alkoxy arms. The isotropic liquid to mesophase transition temperature also displayed similar trends with increasing chain length. The reversibility of the thermal behaviour was verified with DSC on subsequent heating-cooling cycles.

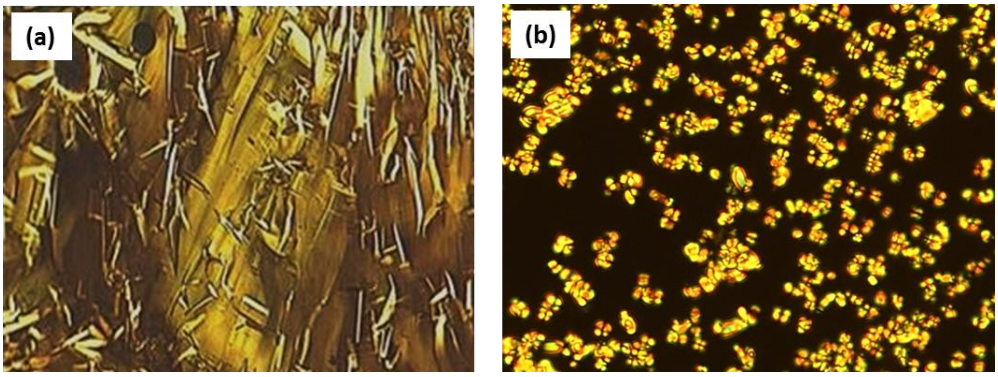

Fig. 5.38: POM photographs of (a) **Ni-16c2pd** at 150 °C and (b) **Zn-16c2pd** at 160°C, on cooling.

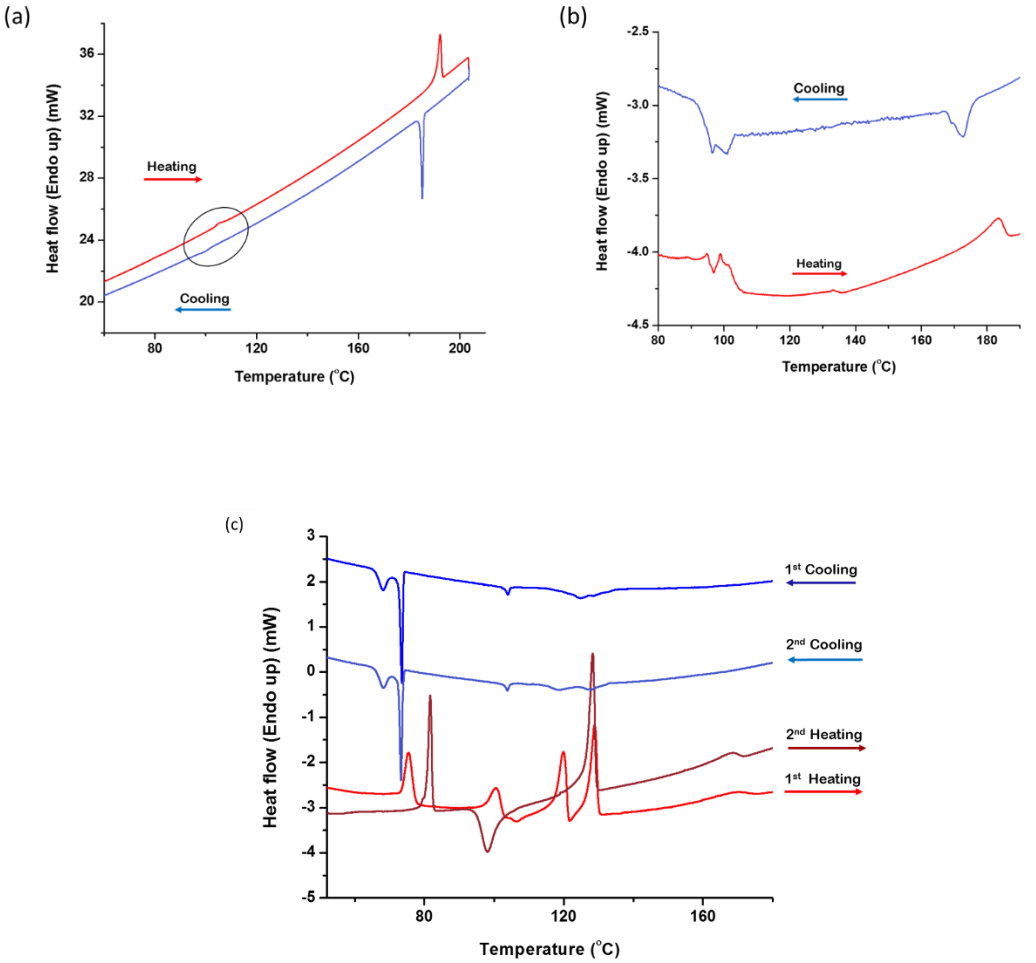

Fig. 5.39: DSC profiles for (a) **Ni-12c2pd** (second scan), (b) **Ni-14c2pd** (second scan) and (c) **Ni-16c2pd** (first and second scan).

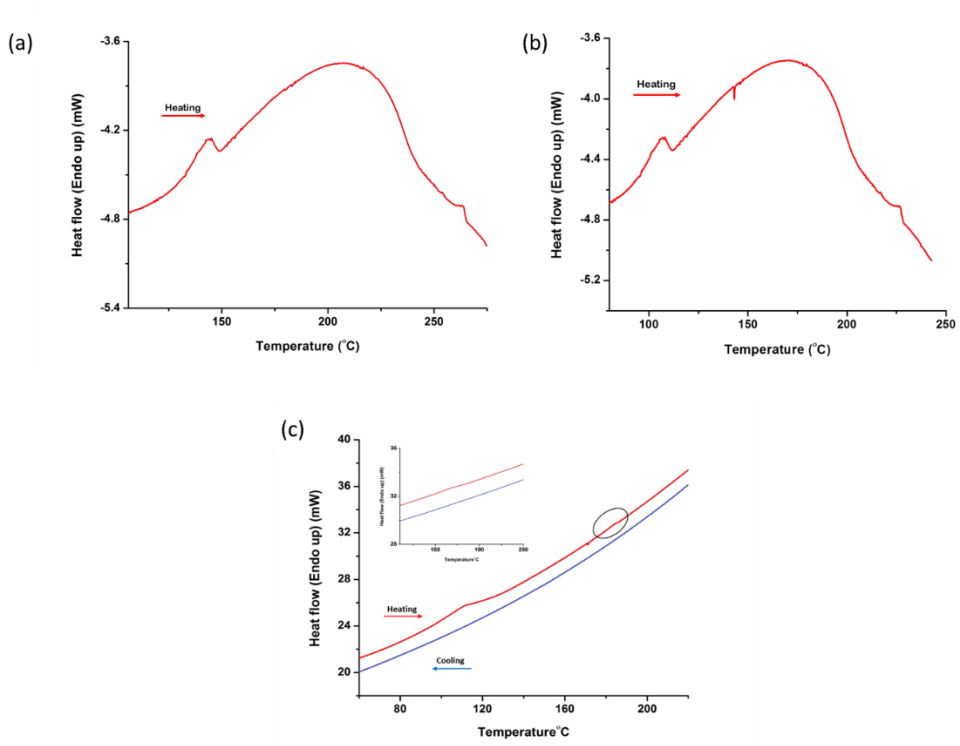

Fig. 5.40: DSC profiles for (a) **Zn-12c2pd** (first scan), (b) **Zn-14c2pd** (first scan) and (c) **Zn-16c2pd** (first scan).

Table 5.18: Thermodynamic data for the Ni(II) and Zn(II) complexes. Transition temperatures are given in °C, and the corresponding enthalpy changes are in parentheses (ΔH; J/g).

Compounds	Heating cycle[a]	Cooling cycle[a]
Ni-12c2pd	Cr 105(1.3) Col_o 192(21.3) I	I 185(22.9) Col_r 99(1.3) Cr
Ni-14c2pd	Cr 98(59.3) Col_o 184.5(9.9) I	I 172(25.1) Col_o 79(3.5) Cr
Ni-16c2pd[b]	Cr 75.7(20.5) Cr_1 100.6(6.9) Cr_2 128(45.7) Col_o 167(6.8)I	I 127(12.3) Col_o 104(1.3) Cr_2 73(13.3) Cr_1 68(5.5) Cr
Ni-16c2pd[c]	Cr 81.6(20.4) Cr_1 98.3(-3.7) Cr_2 128(29.8) Col_o 169(7.4)I	I 127(11.5) Col_o 103(1.6) Cr_2 73.2(13.1) Cr_1 68(5.3) Cr
Zn-12c2pd	Cr 144(15.4) Col_r 253(1.4) I	I 247.3[d] (-) Col_r
Zn-14c2pd	Cr 122(20.6) Col_r 235(1.7) I	I 225.4[d] (-) Col_r
Zn-16c2pd	Cr 111(23.2) Col_r 183(1.2) I	I 177.2[d] (-) Col_r

[a]DSC peak temperature, [b]first heating, [c]second heating, [d]optical microscopy data. Cr, Cr_1, Cr_2 refer to phases that are crystalline or solid; Col_o: oblique columnar phase, Col_r: rectangular columnar phase.

Variable temperature PXRD study:

XRD pattern of **Ni-16c2pd** at 126°C (**Fig. 5.41a**) consisted of a number of Bragg diffraction peaks in the small angle region. Besides, two diffuse halos were observed in the wide angle region, a broad one at 4.7 Å for the lateral short range order of molten alkyl chains and another, less broad halo at 3.7 Å, probably due to the liquid-like correlation between adjacent cores. X-ray diffraction profiles obtained over a wide temperature range (126°C - 80°C) were very similar (**Fig. 5.41a-c**). The profile fitting of the data matched well with that of a two-dimensional oblique columnar phase (Col_o) with a space group of *p*1.[29,30,32] The lattice parameters *a*, *b* and γ were found to be 57.39 Å, 99.38 Å and 69.8° respectively (**Table 5.19**). In a columnar oblique phase, the elementary cell is made up of two columns (**Fig.5.43a**).[29] If a density of 1 gcm^{-3} is assumed for these half-discoid molecules[29] and a periodic stacking value of 3.7 Å of the molecular cores within the column is estimated, we can infer that the columnar cross-section is made up of six molecules (N_{col} = 6). To account for the supramolecular organization in the mesophase, it is assumed that the molecules of the nickel complexes self-assemble into dimers in an anti-parallel fashion (**Fig. 5.43c**).[8,13] Three such dimers stack side by side to cover the surface area of a thin slice of a disk.[8] The lattice constant, *a* in the present case is considerably greater than the DFT optimized radius of a fully extended molecule (*vide infra*), thus supporting the proposed arrangement.

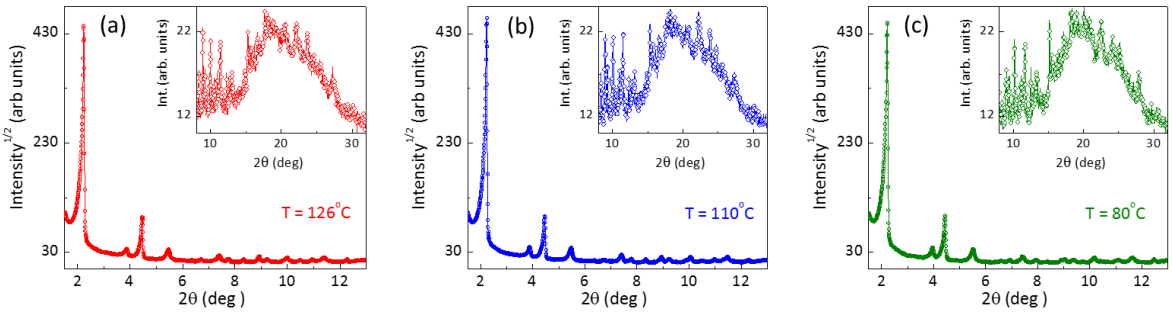

Fig. 5.41: X-ray diffraction pattern of **Ni-16c2pd** at (a)126 °C, (b)110 °C and (c) 80°C.

The X-ray diffractogram of ***Zn-16c2pd*** at 140°C (**Fig. 5.42a**) consisted of a single diffraction maximum at low angles that corresponds to Miller index (100). At wide angles,

a broad halo was observed at 4.6 Å corresponding to liquid like correlation of the molten alkyl chains. The absence of additional characteristic features in the diffraction pattern precluded unambiguous assignment of the mesophase at higher temperatures. The diffraction pattern at 25°C, however, (**Fig. 5.42b**) consisted of five reflections in the small angle region at 52.12 Å, 30.97 Å, 24.56 Å, 16.47 Å and 15.56 Å, respectively (**Table 5.19**). In fact, spacing for the second reflection, from the lowest angle side, is far from being a second harmonic of the first peak. Thus a lamellar structure is ruled out. Accordingly, these were assigned as (100), (010), (200), (300) and (020) reflections of a two dimensional rectangular lattice. Application of extinction rules to the estimated indexations ruled out the possibility of the *c2mm* and *p2gg* plane groups (for *c2mm*, hk: h + k = 2n, h0: h = 2n, 0k: k = 2n; for *p2gg*, hk: no conditions, h0: h = 2n, 0k: k = 2n) which are commonly observed.[31,32] Also absences of reflections with a set of restrictions; hk: no conditions, h0: no conditions, 0k: k = 2n, ruled out the possibility of *p2mg* symmetry.[31,32] In this scenario, since no specific symmetry rules are followed it is presumed that the columns are packed in accordance with an overall *p2mm* symmetry (**Fig. 5.43b**).[32] In addition to the small angle reflections, a broad halo was observed in the wide angle region at 4.2 Å, corresponding to the liquid like nature of molten alkyl chains. However, no second diffuse peak such as would be expected for intra-columnar stacking was not observed suggesting high disorder along each column which would also justify small enthalpy values associated with the clearing process.[53] Assuming a stacking periodicity of 4.2 Å for the molecular cores, it could be deduced that the columnar cross-section is formed by four molecules. In this case, the columnar cross-section is formed by lateral arrangement of two dimers (**Fig. 5.43c**). The lattice parameter, a_r (51.35 Å) in the present case is smaller than that of the Ni(II) complex, consistently with the proposed organization. Also the columnar mesophase of Zn(II) complex is rather disordered at high temperatures, relative to the Ni(II) complexes, so indexation of the PXRD pattern was only possible at room temperature, in a frozen state. Size of the metal ion, in addition to the geometry of the core, is, therefore, an important factor and any significant variation in the ionic radii also affects the thermal stability of the resulting complexes.[54]

Asymmetric chloro-substituted Ni(II) and Zn(II) complexes exhibited rectangular columnar phase(*p2mm/p2gg*) and/or oblique columnar phase(*p1*). The corresponding

VO(IV) complexes were also mesomrphic and displayed rectangular columnar phase with a *p2mm* symmetry (*see previous section*).

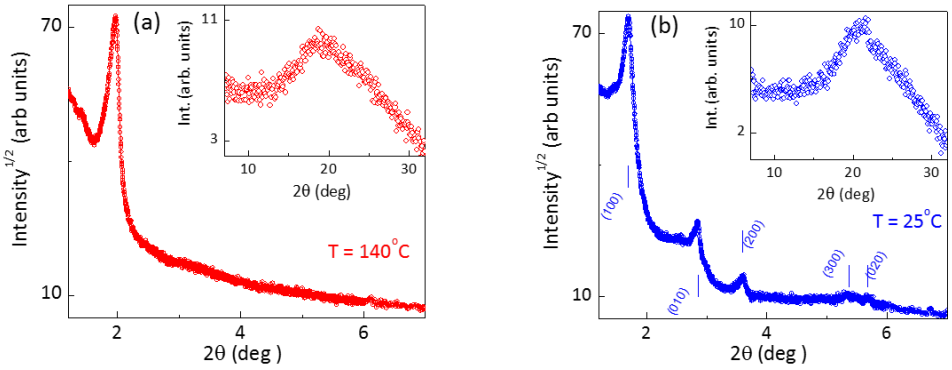

Fig. 5.42: X-ray diffraction pattern of **Zn-16c2pd** (a) at 140 °C and (b) at room temperature (25°C).

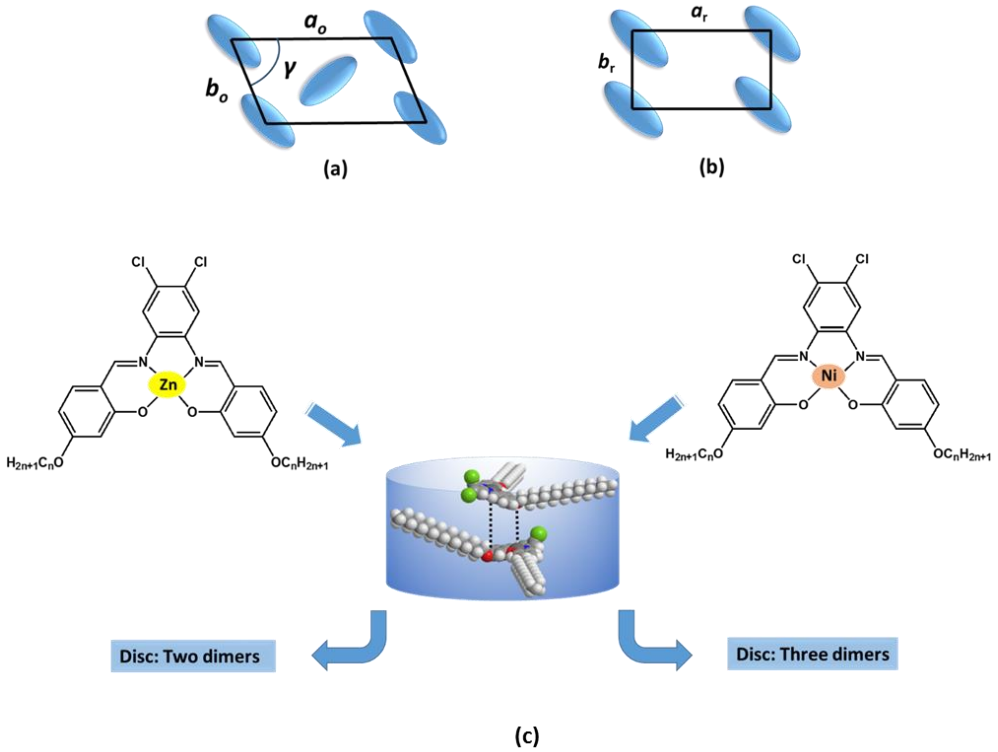

Figure 5.43: Schematic illustration of (a) unit cell of a two dimensional columnar oblique lattice (*p1*), (b) unit cell of a two dimensional rectangular columnar *p2mm* lattice and (c) model for dimeric association of the molecules and molecular organization in the mesophase.

Table 5.19: X-ray diffraction data of **Ni-16c2pd** and **Zn-16c2pd**.

Compounds	Temperature	$d_{meas.}$/Å[a, b]	$d_{calc.}$/Å[a]	Miller indices(hkl)[c]	Mesophase parameters[d]
Ni-16c2pd	126 °C	39.59^{s}	39.59	110	Col_o , *p1*
		22.92^{s}	22.92	130	a_o = 57.32 Å
		19.80^{s}	19.80	100	b_o = 99.38 Å
		16.21^{s}	16.21	250	γ = 69.8°
		13.17^{s}	13.20	330	S_o = 5346.05 Å^2
		11.96^{s}	12.13	450	V_{cell} = 20052.23 Å^3
		11.41^{s}	11.44	030	S_{col} = 2673.03 Å^2
		10.63^{s}	10.72	570	V_{mol} = 1629.86 Å^3
		9.92^{s}	9.90	200	N_{cell} = 12.3, N_{col} = 6.15
		9.58^{s}	9.54	380	
		8.87^{m}	8.73	270	
		8.44^{m}	8.58	680	
		8.08^{m}	8.08	430	
		7.77^{m}	7.77	$\bar{2}10$	
		6.90^{m}	6.86	050	
		5.80^{m}	5.77	530	
		4.74^{d}	4.67	-	
		4.01	4.01	620	
		3.75	-	-	
Zn-16c2pd	140°C	44.78^{s}	45.83	100	Highly disordered LC
		4.5^{d}	-	-	
	25°C	52.12^{s}	51.35	100	Col_r, *p2mm*
		30.97^{s}	31.00	010	a_r = 51.35 Å
		24.56^{s}	25.67	200	b_r = 31.0 Å
		16.47^{m}	17.12	300	S_r = 1591.85 Å^2
		15.56^{m}	15.50	020	V_{cell} = 6717.6 Å^3
		4.22^{d}	-	-	V_{mol} =1543.20 Å^3
					N_{cell} / N_{col} = 4.35

[a] $d_{meas.}$ and $d_{calc.}$ are the experimentally measured and calculated diffraction spacings. [b] Intensity of the reflections- s: sharp, m: medium, d: diffuse. The distances are given in Å. [c] [*hkl*] are the Miller indices of the reflections. [d] Phase parameters, Col_o phase: $1/d_{hk} = 1/sin\gamma\ \sqrt{\{(h/a_o)^2 + (k/b_o)^2 - (2hk\ cos\gamma/a_ob_o)\}}$, γ is columnar tilt angle; lattice area, $S_o = a_ob_osin\gamma$; columnar cross-section, $S_{col} = a_ob_o/2$; Col_r phase: $a_r = d_{10}$; $1/d_{hk} = \sqrt{\{(h/a_r)^2 + (k/b_r)^2\}}$; columnar cross-section in the rectangular cell, $S_r = a_rb_r$. V_{cell}, volume of an elementary cell: Col_o phase, $V_{cell} = a_ob_osin\gamma \times h$; Col_r phase, $V_{cell} = a_rb_r \times h$, where h is intra-columnar repeating distance. V_{mol}, molecular volume is determined considering a density of 1gcm^{-3} according to the relationship $MW/\lambda\rho N_A$, where MW is the molecular weight, N_A is the Avogadro's number and $\lambda(T)$ is a temperature correction coefficient at the temperature of the experiment (T), $\lambda(T) = V_{CH2}(T^o) / V_{CH2}(T)$; where $V_{CH2}(T) = 26.5616 + 0.02023T$ is the volume of a methylene group (in Å^3) at a given temperature (in °C), and T° = 25°C. N_{cell}, number of molecules per unit cell and N_{col}, number of molecules per columnar cross-section.

5.3.7.3. Photophysical properties

The photophysical properties of the salphen ligands **nc2pd** and their corresponding metal complexes (**VO-nc2pd**, **Ni-nc2pd**, **Cu-nc2pd** or **Zn-nc2pd**) were recorded in

dichloromethane solution (conc. 10^{-5} M) and in the solid state at 298 K. The spectral data of the compounds are listed in **Table 5.20**.

The salphen ligands each exhibited two broad absorption bands with maxima at 300nm and 336nm and a shoulder at 355nm corresponding to π-π* transitions of the aromatic rings and the imine unit (**Fig. 5.44**). Following coordination, all the absorption bands shifted remarkably to longer wavelengths with the longer wavelength feature acquiring substantial charge transfer character. For Cu(II) complexes, an additional peak was observed at 350nm. For Ni(II) complexes, the higher wavelength feature at 475nm **(Fig. 5.44)** is believed to be of charge-transfer character. This is ascribed to the excitation of filled d-orbital electrons into the empty antibonding π orbitals (d→π*) of the salphen ligand.[41,42] Moreover, the alkyl chain length variation had virtually no effect on the spectral behaviour in all the cases.

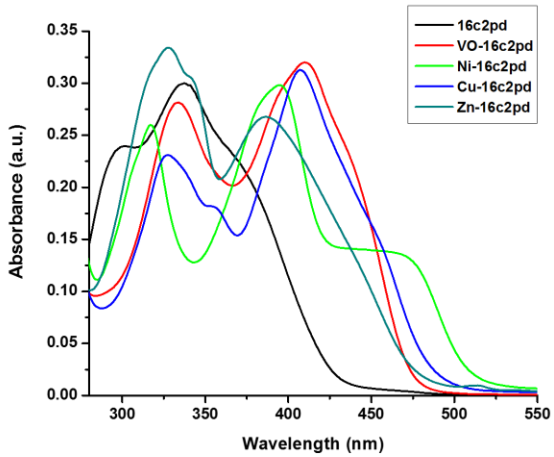

Fig. 5.44: UV-visible spectra of **16c2pd** and corresponding metal complexes in dichloromethane solution (1×10^{-5} M, r.t.).

Photoluminescence study of the compounds was carried out in dichloromethane solution (conc. 10^{-5} M) and in the solid state at room temperature. Emission spectra in the solid state were recorded by placing a uniform powder sheet of the sample between two quartz plates. The ligands and the Zn(II) complexes are luminescent. As a representative example, **Fig. 5.45** and **5.46** shows the photoluminescence spectra of **16c2pd** and **Zn-16c2pd**, respectively. Emission spectra of the ligands in dichloromethane solution consisted of a broad band with maxima at ~ 460nm associated with intraligand π-π* electronic transitions.

Previously reported un-substituted or mono methyl- or nitro- substituted ligands were however, non-luminescent.[16,20,21] Further, while the corresponding Ni(II) complexes were both photoluminescent, the presently studied Ni(II) complexes with dichloro-substituted phenylenediamine spacer are not. The emission maxima for the currently studied Zn(II) complexes was bathochromically shifted (~8nm) compared to the free ligands. The observed fluorescence emission in the Zn(II) complexes originates from metal-perturbed π–π* ligand-centered transitions. The emission intensity is increased on complexation as chelation provided additional rigidity to the salphen framework.[45]

The solid state emission spectra of the ligands and the Zn(II) complexes exhibited a structure, similar to that in solution (**Fig. 5.45** and **5.46**). However, emission maxima for both the ligands and the corresponding Zn(II) complexes got substantially red shifted compared to solution, related shift for the ligands and that of the Zn(II) complexes being 78nm and 36nm, respectively. The red shift of the emission maxima in the solid state can be attributed to the closer association of aromatic cores with a reduction in the local mobility, which reduces deactivation through non-radiative channels.[20] As of for the Zn(II) complexes, since the mesophase is stable down to room temperature, photoluminescence study was conducted in this state as well (**Fig. 5.46**). The mesophase emission maximum is located at 518nm ($\lambda_{exc.}$= 320nm), bathochromically shifted from that observed in solution (468nm) and in the solid state (504nm).

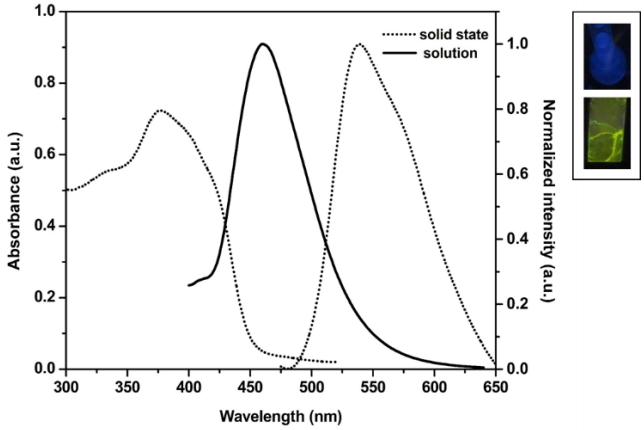

Fig. 5.45: Absorption (left) and normalized fluorescence emission (right) spectra of **16c2pd** in dichloromethane (1×10^{-5}M, r.t.) solution (—) and solid state (----). Side panels show the photoluminescence pictures of solution(top) and solid state (bottom) respectively, as seen after irradiation with a light of 366nm.

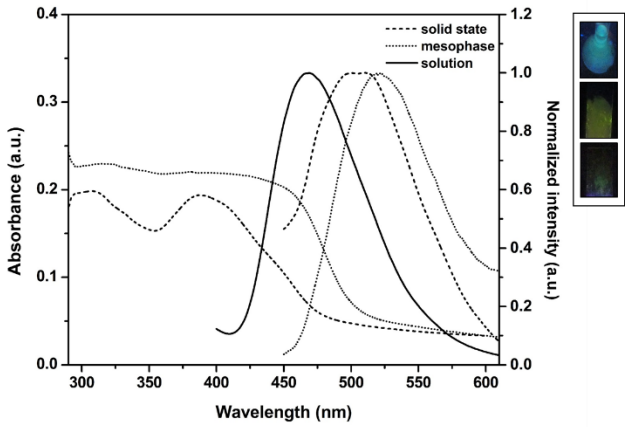

Fig. 5.46: Absorption (left) and normalized fluorescence emission (right) spectra of **Zn-16c2pd** in dichloromethane (1×10^{-5} M, r.t.) solution (—), solid state (----) and mesophase (⋯⋯). Side panels show the photoluminescence pictures of solution(top), solid state(middle) and mesophase (bottom), respectively, as seen after irradiation with a light of 366nm.

Solvatochromic study:

Solvatochromic study of a representative complex from each series, **VO-16c2pd**, **Ni-16c2pd**, **Cu-16c2pd** and **Zn-16c2pd** in dilute solution of solvents (10^{-5} M) of different polarities has been carried out. Absorption spectra of **VO-16c2pd** in non-coordinating solvents consisted of two well-defined bands at 334nm and 410nm with a shoulder at 427nm. However, in coordinating solvent(THF) only two bands were observed with substantial broadening and red-shift of the second absorption feature and the shoulder at longer wavelength being overlapped by the second band (**Fig. 5.47** and **Table 5.21**). This observation can be related to the weak interaction of the solvent molecule trans- to the vanadyl oxo-ligand.[55] The d-level ordering in five coordinate square pyramidal complexes of vanadyl ion (VO^{2+}) is[56] : $d_{xy} < d_{\pi}(d_{xz}, d_{yz}) < d_{x^2-y^2} < d_{z^2}$. The lower wavelength band is ascribed to $d_{xy} \rightarrow d_{x^2-y^2}$ transition while the higher wavelength band appears due to $d_{xy} \rightarrow d_{\pi}$ transition of vanadium. The antibonding d_{π} orbital participates in the $p_{\pi} \rightarrow d_{\pi}$ donation from the vanadyl oxygen atom, while the antibonding $d_{x^2-y^2}$ orbital depends on the strength of the in-plane ligand field. In order to minimize the accumulation of charge on V(IV), the π donation from the axial oxygen decreases, as the in-plane donor strength of the ligand increases.[57] It is speculated that the square pyramidal structure of the complex

is subtly perturbed upon solvent coordination with the V=O group moving toward the equatorial plane of the ligand, resulting in an enhancement of the ligand-vanadium interaction. Coordination of a solvent molecule in the sixth position, trans- to the axial oxygen, thus, decreases the π-donation of the axial oxygen to the metal. As a result the antibonding d_{π} orbital is stabilized while the $d_{x^2-y^2}$ orbital gets destabilized. This accounts for the decrease in the molar absorptivity values and the observed shift in THF.

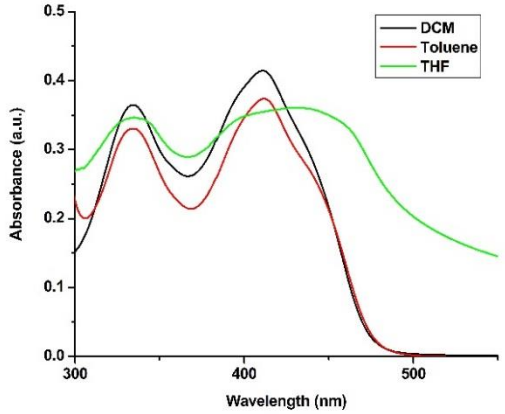

Fig. 5.47: Solvent dependent UV-visible spectra of **VO-16c2pd** (conc. 1×10^{-5} M).

For the Cu(II) and the Ni(II) complexes, absorption features in coordinating solvent(THF) were similar to that observed in the case of non-coordinating solvents (**Fig. 5.48** and **5.49,** and **Table 5.21**).

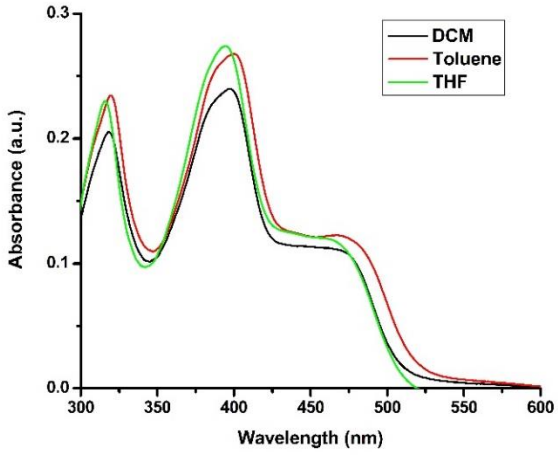

Fig. 5.48: Solvent dependent UV-visible spectra of **Ni-16c2pd** (conc. 1×10^{-5} M).

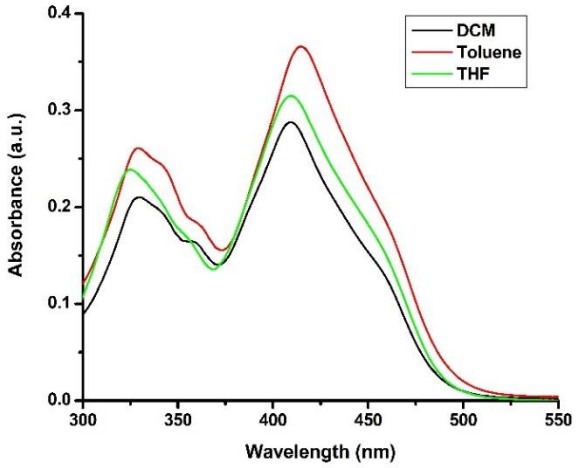

Fig. 5.49: Solvent dependent UV-visible spectra of **Cu-16c2pd** (conc. 1×10^{-5} M).

The Zn(II) complexes, however, exhibited an interesting solvent induced aggregation phenomena. The absorption spectra of **Zn-16c2pd** in non-coordinating solvents (e.g. CH_2Cl_2, $CHCl_3$ and toluene) showed two well-defined bands located at ~328nm, 386-391nm and a shoulder at 413nm (**Fig. 5.50a**) corroborating the presence of aggregates. On switching to coordinating solvent (e.g. THF), solvent induced de-aggregation caused substantial changes in the optical absorption spectrum. Hyperchromism accompanied by a red-shift of the longer wavelength feature was observed. The results are consistent with the formation of H-type aggregates similar to those observed for related salphen systems.[48] Concentration variations had no effect on these spectral features up to a concentration of 1×10^{-4} M (**Fig. 5.50b**). Photoluminescence spectra of **Zn-16c2pd** (**Fig. 5.50a**) in non-coordinating solvents consisted of a broad band with maxima at ~468nm which remained virtually unaltered in THF, though an enhancement in fluorescence intensity could be observed indicating the formation of 1:1 adduct (**Table 5.20**). The emission quantum yield values in non-coordinating solvents (e.g. CH_2Cl_2, $CHCl_3$ and toluene) are close to 20%; this is enhanced (EQY = 30%) upon de-aggregation in THF. Quenching of fluorescence of face-to-face-stacked H-type dimer aggregates(sandwich-type dimers) relative to monomer in the present case as well observed earlier for analogous Zn(II)-salphen complexes,[48] may be argued as a consequence of rapid energy relaxation of the lower excited states.[49]

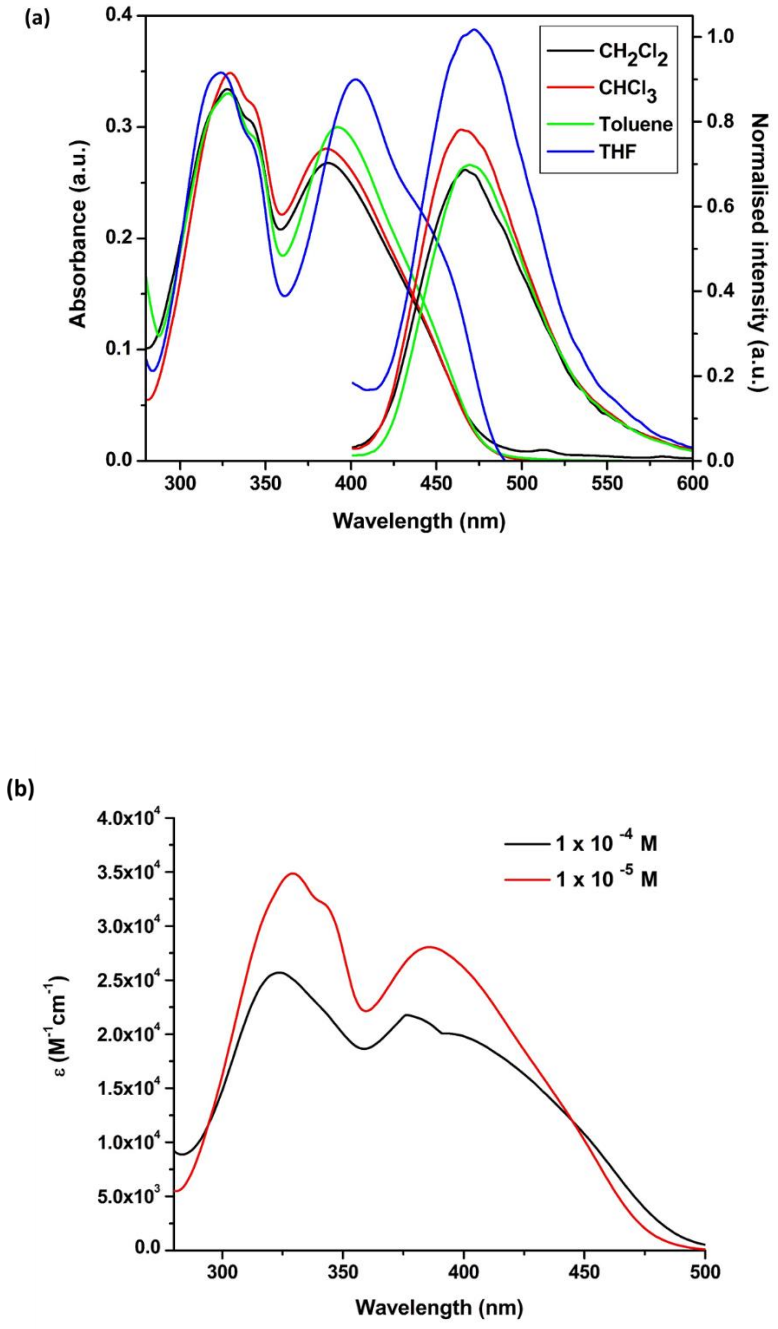

Fig. 5.50: (a) UV-visible (left) and fluorescence (right) spectra of **Zn-16c2pd** in non-coordinating and coordinating solvents (1×10^{-5} M), (b) concentration dependent absorption spectra of **Zn-16c2pd** (CH_2Cl_2, r.t.).

Table 5.20: Absorption data of the ligands (n = 12, 14, 16) and the corresponding metal complexes in various solvents, molar absorption coefficient(ε) in $M^{-1}cm^{-1}$ and photoluminescence data of ligands and Zn(II) complexes in solution and the solid state at 298K.

Compound	Solvent	$\lambda_{abs}(\varepsilon/10^4)$ nm	[a]λ_{em}^{max}(nm) (solution)	[b]λ_{em}^{max}(nm) (solid)	[c]$\Phi_{F(solution)}$	[d]$\Phi_{F(solid)}$
12c2pd	CH_2Cl_2	300(2.2), 336(2.9), 358(2.5)	460	538	0.09	0.04
14c2pd	-do-	300(2.2), 336(3.1), 358(2.4)	-do-	-do-	0.10	0.03
16c2pd	-do-	300(2.3), 336(3.0), 358(2.5)	-do-	-do-	0.10	0.04
VO-12c2pd	-do-	334(2.8), 410(3.1), 427^{sh} (2.6)	-	-	-	-
VO-14c2pd	-do-	334(2.7), 410(3.1), 427^{sh} (2.5)				
VO-16c2pd	-do-	334(2.8), 410(3.2), 427^{sh} (2.6)				
Ni-12c2pd	-do-	317(2.5), 396(2.9), 475 (1.4)	-	-	-	-
Ni-14c2pd	-do-	317(2.7), 396(3.0), 475 (1.7)				
Ni-16c2pd	-do-	317(2.6), 396(2.9), 475 (1.5)				
Cu-12c2pd	-do-	328(2.2), 350(1.9), 407 (3.2) 433^{sh} (2.4)	-	-	-	-
Cu-14c2pd	-do-	328(2.3), 350(1.8), 407 (3.2) 433^{sh} (2.3)				
Cu-16c2pd	-do-	328(2.3), 350(1.8), 407 (3.1) 433^{sh} (2.3)				
Zn-12c2pd	-do-	327(3.2), 386(2.5), 411^{sh} (2.1)	468	504	0.19	0.07
Zn-14c2pd	-do-	327(3.4), 386(2.6), 411^{sh} (2.3)	-do-	-do-	0.19	0.07
Zn-16c2pd	CH_2Cl_2	327(3.3), 386(2.6), 411^{sh} (2.2)	468	-do-	0.20	0.08
	$CHCl_3$	327(3.5), 386(2.8), 413^{sh} (2.3)	468		0.20	
	Toluene	327(3.3), 391(2.9), 415^{sh} (2.4)	468		0.21	
	THF	323(3.5), 403(3.4), 426^{sh} (2.6)	469		0.30	

[a] λ_{ex} = 336nm (ligand); 320nm (Zn-complex). [b] λ_{ex} = 386nm (ligand); 320nm (Zn-complex).

[c] Estimated error: ± 5 %. [d] Estimated error: ± 10 %. sh: shoulder

Table 5.21: The UV-visible spectral data of **VO-16c2pd**, **Ni-16c2pd** and **Cu-16c2pd** in different solvents at 298K.

Compounds	Solvents	λ_{abs} nm ($\varepsilon/10^4$)
VO-16c2pd	CH_2Cl_2	334(3.6), 410(4.1), 427^{sh}(3.4)
	Toluene	334(3.3), 411(3.7), 427^{sh}(3.2)
	THF	334(3.5), 428^{br}(3.6)
Ni-16c2pd	CH_2Cl_2	317(2.0), 396(2.4), 475(1.1)
	Toluene	317(2.3), 398(2.6), 477(1.2)
	THF	315(2.3), 394(2.7), 469(1.2)
Cu-16c2pd	CH_2Cl_2	328(2.1), 350(1.6), 407(2.9), 433^{sh}(2.0)
	Toluene	328(2.6), 350(1.9), 410(3.6), 433^{sh}(2.6)
	THF	324(2.4), 350(1.8), 407(3.2), 433^{sh}(2.4)

br: broad peak; sh: shoulder

5.3.7.4. DFT study

As diffraction quality single crystals could not be isolated, density functional theory (DFT) study was used to arrive at the energy optimized electronic structure of the complexes. A representative Zn(II) complex, **Zn-16c2pd** has been chosen for the purpose. All the quantum chemical calculations have been performed employing GAUSSIAN 09 program package.[33] The ground state geometry optimization in the gas phase of the complex has been performed using the three-parameter fit of Becke's hybrid functional combined with the Lee-Yang-Parr correlation functional termed as B3LYP hybrid,[34,35] generalized gradient approximation (GGA) exchange along with 6-311+G(d,p), 6-31+G(d,p), 6-31G(d) and 6-31G basis sets[36] for Zn, N and O, C and H, respectively, without imposing any symmetry constrain. The appropriate structure of the complex has been confirmed as energy minima by calculating the vibrational frequency and confirming the absence of any imaginary frequencies. Key geometric parameters of the optimized **Zn-16c2pd** complex, estimated by DFT at the B3LYP level are gathered in **Table 5.22**. Average bond angles about the metal center suggest a distorted square planar geometry for the Zn(II) complex (**Fig. 5.51**).

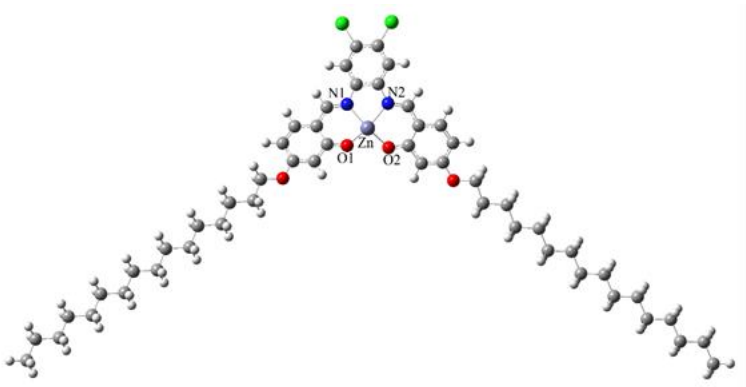

Fig. 5.51. Optimized electronic structure of **Zn-16c2pd**.

Table 5.22: Selected bond lengths (Å) and bond angles (°) of **Zn-16c2pd** optimized at the B3LYP level.

Structural parameters	Bond lengths (Å) and bond angles (°)
Zn—O1	1.912
Zn—O2	1.912
Zn—N1	2.039
Zn—N2	2.039
O1— Zn— O2	104.2
N1 — Zn—N2	81.0
N1 — Zn—O1	92.6
N2 — Zn—O2	92.6
N1—N2 — O2—O2	-33.3
N1—O1 — O2—N2	30.9
Molecular length	42.6
Dipole moment	1.28D

5.3.8. Comparative assessment of thermal and photophysical properties of the mono-and di-substituted salphen ligands and their metal complexes

A rich mesomorphic and photophysical diversity is thus, observed in the presently studied mono- and di-substituted salphen ligands and their metal complexes as well as previously reported structurally related salphen systems containing un-substituted or mono-substituted phenylenediamine spacers, this containing either electron donating methyl(-CH_3) or

electron withdrawing nitro(-NO_2) substituents. A critical comparison of the mesomorphic and photophysical properties of all such ligand systems and their corresponding metal complexes is presented in **Table 5.23**.

Between the differently substituted salphen ligands, while the dichloro-substituted systems are non-liquid-crystalline, those with mono-halogen substitution are all mesomorphic and display columnar phases at or near room temperature. Mesophases exhibited by these ligands are columnar oblique (*p1*), rectangular columnar (*p2mm*) and hexagonal columnar (*p6mm*). Besides, all the mono- and dihalogen substituted salphen ligands emit blue light at room temperature. Quite apart, the hitherto reported un-substituted or mono-methyl or nitro-substituted derivatives are both non-mesomorphic and non-luminescent.[13,20,21]

A comparison amongst VO(IV) complexes of differently substituted salphen ligands indicated that, while the VO(IV) complexes of salphen ligands bearing mono-fluoro or chloro-substituted aromatic spacer are mesomorphic, those derived from ligands with mono-bromo- or dichloro-substituted aromatic spacers are not, decomposing at higher temperatures. The previously reported complexes with unsubstituted or methyl substituted aromatic spacers were also mesomorphic.[15,18] However, the clearing or the decomposition temperatures of the halogenated complexes are higher than that of the un-substituted or methyl-substituted ones. The phases exhibited by the mesomorphic VO(IV) complexes is also quite diverse. The un-substituted ones exhibited lamellar columnar mesomorphism,[18] while the methyl-substituted VO(IV) complexes displayed a phase transition between two rectangular columnar phases(*c2mm*).[15] The presently studied fluoro and chloro-substituted complexes displayed columnar rectangular phase (*p2mm*).

The Cu(II) complexes of the presently studied mono- or di-halogenated salphen ligands are all non-mesomorphic. Analogous nitro-substituted complexes were also non-mesomorphic.[13] In contrast to that, the previously reported Cu(II) complexes of unsubstituted or methyl-substituted ligands were mesomorphic and displayed rectangular columnar (Col_r) and rectangular plastic columnar (Col_{rp}) phase, respectively.[13]

The Ni(II) complexes of the presently studied halogenated systems are all mesomorphic and displayed enantiotropic columnar rectangular or columnar oblique phases respectively. Those previously reported without or with methyl or nitro substituted spacer were also mesomorphic.[16] Such ligands upon coordination with Ni^{2+} ion have been found to exhibit

monotropic/enantiotropic phase behaviour showing rectangular columnar mesophases with *c2mm* symmetry. Besides, all previously reported mono-substituted Ni(II) complexes along with the mono-halogenated ones under present discussion exhibit photoluminescence but, the dichloro-substituted complexes being discussed herein are non-luminescent.

The hitherto reported Zn(II) complexes without any substituent or with an electron donating methyl group (-CH_3) at the spacer displayed monotropic columnar mesomorphism.[20,21] Mesophases exhibited by these complexes were either rectangular/oblique columnar (P_{222}/P_{112}) or hexagonal columnar.[20,21] On the contrary, with electron withdrawing fluoro-, chloro-, bromo- or vicinal dichloro- substituent at the spacer, enantiotropic phase behaviour with enhanced thermal stability is observed in the Zn(II) complexes under current investigation. While the fluoro-and the chloro-substituted Zn(II) complexes exhibited rectangular columnar phase with a *p2gg* symmetry, the bromo-substituted analogs displayed rectangular columnar phase with a *p2mg* symmetry. The Zn(II) complexes of di-substituted salphen ligands also displayed enantiotropic rectangular columnar phase with a *p2mm* symmetry which is stable at room temperature. In addition, the Zn(II) complexes are all luminescent at room temperature.

Thus, a subtle interplay of both steric and electronic factors originating from aromatic spacer and distortions in coordination geometry associated with the nature of metal ions might be responsible for the observed mesomorphic and photophysical diversity in the salphen complexes under current investigation and their deviation from those exhibited by structurally analogous metal-salphen systems.

Table 5.23: Mesomorphism and photoluminescence of salphen ligands and corresponding metal complexes with different 'salphen' spacer substituents.

Spacer	Compounds	Mesophase(Symmetry)	[a]PL	References
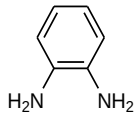	16opd	Non-LC	-	[13, 16, 18, 20]
	Zn-16opd	Col_r/Col_o (P_{222}/P_{112})	+	
	Ni-16opd	Col_r (*c2mm*)	+	
	VO-16opd	Col_L	-	
	Cu-16opd	Col_{rp}	-	
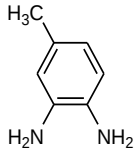	16mpd	Non-LC	-	[13, 15, 16, 21]
	Zn-16mpd	Col_h	+	
	Ni-16mpd	Col_r (*c2mm*)	+	
	VO-16mpd	$Col_{r1} \rightarrow Col_{r2}$ (*c2mm*)	-	
	Cu-16mpd	Col_r (*c2mm*)	-	
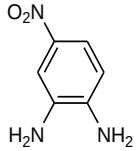	16npd	Non-LC	-	[13, 16]
	Ni-16npd	Col_r (*c2mm*)	+	
	Cu-16npd	Non-LC	-	
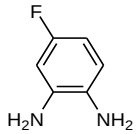	16fpd	Col_o(*p1*)	+	Present work
	Zn-16fpd	Col_r (*p2gg*)	+	
	Ni-16fpd	Col_r /Col_o (*p2mm/ p1*)	+	
	VO-16fpd	Col_r (*p2mm*)	-	
	Cu-16fpd	Non-LC	-	
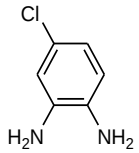	16cpd	Col_r (*p2mm*)	+	Present work
	Zn-16cpd	Col_r (*p2gg*)	+	
	Ni-16cpd	Col_r (*p2mm*)	+	
	VO-16cpd	Col_r (*p2mm*)	-	
	Cu-16cpd	Non-LC	-	
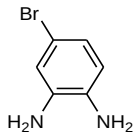	16bpd	Col_h (*p6mm*)	+	Present work
	Zn-16bpd	Col_r(*p2mg*)	+	
	Ni-16bpd	Col_r (*p2mm*)	+	
	VO-16bpd	Non-LC	-	
	Cu-16bpd	Non-LC	-	
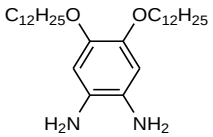	$MnXL^4$ (X = Cl, Br)	Col_h	-	[8]
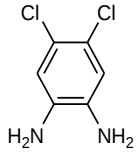	16c2pd	Non-LC	+	Present work
	Zn-16c2pd	Col_r (*p2mm*)	+	
	Ni-16c2pd	Col_o (*p1*)	-	
	VO-16c2pd	Non-LC	-	
	Cu-16c2pd	Non-LC	-	

[a] PL: photoluminescence; +: PL active.

5.4. Conclusion

In summary, synthesis of three new series of mono-halogen-substituted (X= F, Cl, Br) and a series of di-halogen-substituted (X= Cl/Cl) 'salphen' type ligands and their 1:1 metal complexes with VO^{2+}, Ni^{2+}, Cu^{2+} and Zn^{2+} metal ions has been successfully achieved through the choice of differently halogenated aromatic diamines. Influence of size, position and associated electronic properties of the halogen substituent at the aromatic spacer upon the mesomorphic and photophysical properties of the ligands and their corresponding metal complexes has been studied. Besides, the square-planar Zn(II) complexes having a vacant axial coordination site facilitate solvatochromism, exhibiting aggregate or monomer formation in solvents of different coordinating ability. Furthermore, solvatochromic studies involving selected VO(IV), Cu(II) and Ni(II) complexes of the dichloro-substituted ligands has also been carried out. The axial vacant coordination site at the square-pyramidal VO(IV) center facilitates solvatochromism in solvents of different coordinating ability. The Cu(II) and Ni(II) complexes lack such 'solvatochromism'. The metal coordination induced mesomorphism coupled with solvatochromic effects in these salphen-ligated systems are of particular relevance to the design of functional entities with both thermo and chemo-sensing properties.

REFERENCES

[1] C. J. Whiteoak, G. Salassa, A. W. Kleij, *Chem. Soc. Rev*., 2012, **41**, 622.

[2] S. J. Wezenberg, A. W. Kleij, *Angew. Chem. Int. Ed*., 2008, **47**, 2354.

[3] J. Cheng, X. Ma, Y. Zhang, J. Liu, X. Zhou, H. Xiang, *Inorg. Chem.*, 2014, **53**, 3210.

[4] S. J. Wezenberg, E. C. Escudero-Adán, J. Benet-Buchholz, A. W. Kleij, *Org. Lett.*, 2008, **10**, 3311.

[5] A. W. Kleij, *Dalton Trans*., 2009, 4635.

[6] P. G. Lacroix, *Eur. J. Inorg. Chem.*, 2001, 339.

[7] S. Di Bella, *Chem. Soc. Rev.*, 2001, **30**, 355.

[8] R. Chico, C. Dominguez, B. Donnio, S. Coco, P. Espinet, *Dalton Trans.*, 2011, **40**, 5977.

[9] K. Binnemans, K. Lodewyckx, B. Donnio, D. Guillon, *Eur. J. Inorg. Chem*., 2005, 1506.

[10] J. Cheng, K. Wei, X. Ma, X. Zhou, H. Xiang, *J. Phys. Chem. C*, 2013, **117**, 16552.

[11] A. M. Castilla, S. Curreli, M. M. Belmonte, E. C. Escudero-Adán, J. Benet-Buchholz, A. W. Kleij, *Org. Lett.*, 2009, **11**, 5218.

[12] M. Palucki, N. S. Finney, P. J. Pospisil, M. L. Güler, T. Ishida, E. N. Jacobsen, *J. Am. Chem. Soc.*, 1998, **120**, 948.

[13] C. Datta, R. Chakrabarty, G. Das, C. R. Bhattacharjee, P. Mondal, *Liq. Cryst*., 2014, **41**, 541.

[14] N. Hoshino, *Coord. Chem. Rev.*, 1998, **174**, 77.

[15] C. R. Bhattacharjee, C. Datta, G. Das, P. Mondal, *Liq. Cryst.*, 2012, **39**, 819.

[16] C. R. Bhattacharjee, C. Datta, G. Das, R. Chakrabarty, P. Mondal, *Polyhedron*, 2012, **33**, 417.

[17] C. R. Bhattacharjee, C. Datta, G. Das, P. Mondal, *Materials Science and Engineering C*, 2012, **32**, 735.

[18] C. R. Bhattacharjee, G. Das, P. Mondal, S. K. Prasad, D. S. S. Rao, *Inorg. Chem. Commun.*, 2011, **14**, 606.

[19] C. R. Bhattacharjee, G. Das, P. Mondal, *Eur. J. Inorg. Chem.*, 2011, 5390.

[20] C. R. Bhattacharjee, G. Das, P. Mondal, S. K. Prasad, D. S. S. Rao, *Eur. J. Inorg. Chem.*, 2011, 1418.

[21] C. R. Bhattacharjee, G. Das, P. Mondal, N. V. S. Rao, *Polyhedron*, 2010, **29**, 3089.

[22] M. Bertolotti, G. Sansoni and F. Scudieri, *Appl. Opt.*, 1979, **18**, 528.

[23] Y. Sagara, S. Yamane, T. Mutai, K. Araki, T. Kato, *Adv. Funct. Mater.*, 2009, **19**, 1869.

[24] M. P. Aldred, A. J. Eastwood, S. M. Kelly, P. Vlachos, A. E. A. Contoret, S. R. Farrar, B. Mansoor, M. O'Neill, W. C. Tsoi, *Chem. Mater.*, 2004, **16**, 4928.

[25] M. Grell, D. D. C. Bradley, *Adv. Mater.*, 1999, **11**, 895.

[26] S. Sergeyev, W. Pisula, Y. H. Geerts, *Chem. Soc. Rev.*, 2007, **36**, 1902.

[27] V. Liuzzo, W. Oberhauser, A. Pucci, *Inorg. Chem. Commun.*, 2010, **13**, 686.

[28] G. Consiglio, S. Failla, I. P. Oliveri, R. Purrello, S. Di Bella, *Dalton Trans.*, 2009, 10426.

[29] F. Morale, R. W. Date, D. Guillon, D. W. Bruce, R. L. Finn, C. Wilson, A. J. Blake, M. Schröder, B. Donnio, *Chem. Eur. J.*, 2003, **9**, 2484.

[30] J.-W. Choi, J.-H. Han, M.-H. Ryu, B.-K. Cho, *Bull. Korean Chem. Soc.*, 2011, **32**, 781.

[31] N. Godbert, A. Crispini, M. Ghedini, M. Carin, F. Chiaravallotic, A. Ferrise, *J. Appl. Cryst.*, 2014, **47**, 668.

[32] S. Laschat, A. Baro, N. Steinke, F. Giesselmann, C. Hägele, G. Scalia, R. Judele, E. Kapatsina, S. Sauer, A. Schreivogel, M. Tosoni, *Angew. Chem. Int. Ed.*, 2007, **46**, 4832.

[33] M. J. Frisch, G. W. Trucks, H. B. Schlegel, G. E. Scuseria, M. A. Robb, J. R. Cheeseman, G. Scalmani, V. Barone, B. Mennucci, G. A. Petersson, H. Nakatsuji, M. Caricato, X. Li, H. P. Hratchian, A. F. Izmaylov, J. Bloino, G. Zheng, J. L. Sonnenberg, M. Hada, M. Ehara, K. Toyota, R. Fukuda, J. Hasegawa, M. Ishida, T. Nakajima, Y.Honda, O. Kitao, H. Nakai, T. Vreven, J. A. Montgomery Jr., J. E. Peralta, F. Ogliaro, M. Bearpark, J. J. Heyd, E. Brothers, K. N. Kudin, V. N. Staroverov, R. Kobayashi, J. Normand, K. Raghavachari, A. Rendell, J. C. Burant, S. S. Iyengar, J. Tomasi, M. Cossi, N. Rega, J. M. Millam, M. Klene, J. E. Knox, J. B. Cross, V. Bakken, C. Adamo, J. Jaramillo, R. Gomperts, R. E. Stratmann, O. Yazyev, A. J. Austin, R. Cammi, C. Pomelli, J. W. Ochterski, R. L. Martin, K. Morokuma, V. G. Zakrzewski, G. A. Voth, P. Salvador,

J. J. Dannenberg, S. Dapprich, A. D. Daniels, Ö. Farkas, J. B. Foresman, J.V. Ortiz, J. Cioslowski, D. J. Fox, GAUSSIAN 09, Gaussian Inc., Wallingford CT, 2009.

[34] A. D. Becke, *J. Chem. Phys.*, 1993, **98**, 5648.

[35] C. Lee, W. Yang, R. G. Parr, *Phys. Rev. B*, 1988, **37**, 785.

[36] P. C. Hariharan, J. A. Pople, *Theor. Chim. Acta*, 1973, **28**, 213.

[37] A. Serrette, P. J. Carroll, T. M. Swager, *J. Am. Chem. Soc.*, 1992, **114**, 1887.

[38] S. T. Trzaska, T. M. Swager, *Chem. Mater.*, 1998, **10**, 438.

[39] B. J. Delley, *Chem. Phys.*, 1990, **92**, 508.

[40] C. V. Yelamaggad, A. S. Achalkumar, D. S. S. Rao, S. K. Prasad, *J. Mater. Chem.*, 2007, **17**, 4521.

[41] B. Bosnich, *J. Am. Chem. Soc.*, 1968, **90**, 627.

[42] A. Akbari, Z. Alinia, *Comput. Res.*, 2013, **1**, 19.

[43] R. Paschke, D. Balkow, U. Baumeister, H. Hartung, J. R. Chipperfield, A. B. Blake, P. G. Nelson, G. W. Gray, *Mol. Cryst. Liq. Cryst.*, 1990, **188**, 105.

[44] C. Cuerva, J. A. Campo, P. Ovejero, M. R. Torres, M. Cano, *Dalton Trans.*, 2014, **43**, 8849.

[45] T. Yu, K. Zhang, Y. Zhao, C. Yang, H. Zhang, L. Qian, D. Fan, W. Dong, L. Chen, Y. Qiu, Inorg. Chim. Acta, 2008, **361**, 233.

[46] M. M. Belmonte, S. J. Wezenberg, R. M. Haak, A. Daniele, E. C. EscuderoAdán, J. Benet-Buchholz, A. W. Kleij, *Dalton Trans.*, 2010, **39**, 4541.

[47] E. C. Escudero-Adán, J. Benet-Buchholz, A. W. Kleij, *Chem. Eur. J.*, 2009, **15**, 4233.

[48] G. Consiglio, S. Failla, P. Finocchiaro, I. P. Oliveri, S. Di Bella, *Dalton Trans.*, 2012, **41**, 387.

[49] M. Kasha, H. R. Rawls, M. A. El-Bayoumi, *Pure Appl. Chem*., 1965, **11**, 371.

[50] K. H. Kim, Y. K. Han, J. Jung, *Theor. Chem. Acc.*, 2005, **113**, 233.

[51] J. Aihara, *J. Phys. Chem. A*, 1999, **103**, 7487.

[52] O. N. Kadkin, E. H. Kim, S. Y. Kim, M.-G. Choi, *Polyhedron*, 2009, **28**, 1301.

[53] C. Cuerva, J. A. Campo, P. Ovejero, M. R. Torres, E. Oliveira, S. M. Santos, C. Lodeiro, M. Cano, *J. Mater. Chem. C*, 2014, **2**, 9167.

[54] F. Morale, R. L. Finn, S. R. Collinson, A. J. Blake, C. Wilson, D. W. Bruce, D. Guillon, B. Donnio, M. Schröder, *New J. Chem.*, 2008, **32**, 297.

[55] S. S. Amin, K. Cryer, B. Zhang, S. K. Dutta, S. S. Eaton, O. P. Anderson, S. M. Miller, B. A. Reul, S. M. Brichard, D. C. Crans, *Inorg. Chem.*, 2000, **39**, 406.

[56] L. G. Vanquickenborne, S. P. McGlynn, *Theor. Chim. Acta*, 1968, **9**, 390.

[57] L. J. Boucher, T. F. Yen, *Inorg. Chem.*, 1968, **7**, 2665.